COMPARATIVE ANALYSIS OF RECONSTRUCTED IMAGE QUALITY IN A SIMULATED CHROMOTOMOGRAPHIC IMAGER

THESIS

Ryan L. Tervo, Captain, USAF

AFIT-ENP-14-M-35

DEPARTMENT OF THE AIR FORCE
AIR UNIVERSITY

AIR FORCE INSTITUTE OF TECHNOLOGY

Wright-Patterson Air Force Base, Ohio

DISTRIBUTION STATEMENT A
APPROVED FOR PUBLIC RELEASE; DISTRIBUTION UNLIMITED

The views expressed in this thesis are those of the author and do not reflect the official policy or position of the United States Air Force, Department of Defense, or the United States Government. This material is declared work of the United States Government and is not subject to copyright protection in the United States.

AFIT-ENP-14-M-35

COMPARATIVE ANALYSIS OF RECONSTRUCTED IMAGE QUALITY IN A SIMULATED CHROMOTOMOGRAPHIC IMAGER

THESIS

Presented to the Faculty

Department of Engineering Physics

Graduate School of Engineering and Management

Air Force Institute of Technology

Air University

Air Education and Training Command

In Partial Fulfillment of the Requirements for the

Degree of Master of Science in Applied Physics

Ryan L. Tervo, BA

Captain, USAF

March 2014

DISTRIBUTION STATEMENT A
APPROVED FOR PUBLIC RELEASE; DISTRIBUTION UNLIMITED

AFIT-ENP-14-M-35

COMPARATIVE ANALYSIS OF RECONSTRUCTED IMAGE QUALITY IN A SIMULATED CHROMOTOMOGRAPHIC IMAGER

Ryan L. Tervo, BA
Captain, USAF

Approved:

//signed//	17 March 2014
Michael Hawks, PhD (Chairman)	Date
//signed//	17 March 2014
Glen P. Perram, PhD (Member)	Date
//signed//	17 March 2014
Matthew C. Fickus, PhD (Member)	Date

Abstract

A hyperspectral chromotomographic instrument has been developed to determine the spatial and spectral distribution of a target. It does this by recording the dispersed images produced by a rotating direct vision prism with a high speed camera. The recorded images are processed through a tomographic reconstruction algorithm to produce a reconstructed hypercube.

A physics-based system model was developed to investigate three areas. The first was how the prism angle selection and range of angles used impacted the reconstructed image quality. The second was an assessment of a new iterative reconstruction algorithm developed to remove artifacts produced in the Back Projection algorithm. The third area was how optical aberrations in the recorded images impacted the reconstructed image. The simulation modeled a new prism design because a distortion-like effect was found in the current prism design.

It was determined the range of prism angles recorded impacts the reconstructed image quality. The greater the range of angles used in the reconstruction the better the reconstructed image quality was. The majority of the image quality gains were accomplished in the first 20 projections used in the reconstruction. Provided at least 30 projections were used in the reconstruction the new algorithm, developed for this investigation, outperformed Back Projection in 15 of the 18 targets evaluated. Minor amounts of optical aberration negatively impact the reconstructed image quality. The image quality lost due to the reconstruction process and the optical aberrations appears to be accumulative.

Acknowledgments

I would like to thank my committee members for their excellent support. I am especially thankful for my advisor, Dr. Michael Hawks, whose keen insight in optical design and the theory of chromotomography was invaluable. When running into walls it is good to have an advisor like Dr. Hawks who can find a way to keep moving forward. His support in both tangible and intangible ways is appreciated. Without his help, I would not have been able to deliver this product.

I would also like to thank Captain Kyle Dufaud, one could not ask for a better lab partner. Also, Dr. Collins and Mr. Burchett for sharing their wealth of IT resources. This reduced the processing time down from several weeks or months to days and without which most of the simulations and reconstructions would not have been completed on time.

Lastly thanks to my family most of all who was with me on the ups and downs of this journey. To my wife, who is wonderful in all she does. To my children, who never cease to amaze.

Ryan L. Tervo

Table of Contents

Page

Abstract iv

Acknowledgments v

Table of Contents vi

List of Figures viii

List of Tables xviii

I. Introduction 1

1.1 Motivation 2
1.2 Research Goals 3
1.3 Organization 3

II. Background 5

2.1 Hyperspectral Remote Sensing 5
2.2 Computed Tomography Origins 6
2.3 Fundamental Principles of Chromotomography 8
2.4 Basic Reconstruction Algorithm 10
2.5 Mathematical Basis of Chromotomography 11
2.5.1 Cone of Missing Information 15
2.6 Optical Aberrations 17

III. Methodology 19

3.1 Simulation 20
3.1.1 Simulation Tool 21
3.1.2 Optical Model 21
3.1.3 Need for a New Prism Design 23
3.1.4 Current and Proposed CTEx Prism Design 27
3.1.5 Zemax Image Simulation 30
3.2 Reconstruction 31
3.2.1 Primary Reconstruction Algorithm 33
3.3 Analysis 34
3.3.1 Reconstructed Image Analysis Method 35
3.4 Video Conversion Tool 38
3.5 New Reconstruction Algorithm 39
3.5.1 Back Projection Reconstruction Examples and Fundamental Problem 40
3.5.2 Proposed Solution to Back Projection Problem 46

Page

IV. Analysis and Results....54

4.1 Initial Target Sets....54
4.2 Angle Selection....57
4.2.1 Step By Step Example *57*
4.2.2 Results of Summary.... *59*
4.2.3 Results of Summary.... *62*
4.2.4 General Results.... *67*
4.3 Comparison of Back Projection to Shift and Place Reconstructed Images 68
4.3.1 20 Nanometer Separation.... *68*
4.3.2 5 Nanometer Separation.... *73*
4.4 Impact of Optical Aberrations 78
4.4.1 Optical Aberration using Zernike Polynomial 4: "Defocus".... *80*
4.4.2 Optical Aberration using Zernike Polynomial 5: "Astigmatism".... *84*
4.4.3 Optical Aberration using Zernike Polynomial 7: "Coma" *88*
4.4.4 Optical Aberration using Zernike Polynomial 9: "Spherical" *92*
4.5 Summary of Results....96

V. Conclusions and Recommendations 97

5.1 Model, Simulation, Reconstruction, and Analysis Tools 97
5.2 Angle Selection and Range....97
5.3 Back Projection and Shift and Place Reconstruction 98
5.4 Optical Aberrations and Reconstructed Image Quality....98
5.5 Recommendations....98

Appendix A....100

References....127

List of Figures

Page

Figure 1. This is a classic spectral hypercube in which each layer contains the spatial distribution for a different wavelength bin or frequency band. 6

Figure 2. Graphical representation of different scanning techniques. 7

Figure 3. A typical chromotomographic instrument. 9

Figure 4. Each box contains a recorded image and contains a unique projection of a segment of an Air Force Bar Chart in which three wavelengths are present. .. 10

Figure 5. This depicts the Shift and Add reconstruction algorithm. 11

Figure 6. Represents information recorded in the frequency domain. 17

Figure 7. The simulation tool interface. 22

Figure 8. A standard chromotomographic optical model using paraxial lenses and direct vision prism. 22

Figure 9. Comparison of optical aberration using same image at different wavelengths.. 23

Figure 10. Each image has been simulated in the Zemax Image Simulation tool using the same target image of vertical bars with the current CTEx optical model. 25

Figure 11. Comparison of dispersion curves for an on axis source to an off axis source demonstrating the wavelength and location dependence. 25

Figure 12. Comparison of reconstructed images using the current prism design. 26

Figure 13. Comparison of reconstructed images using the current prism design. 27

Figure 14. Current CTEx prism design. 28

Figure 15. The proposed prism design. 28

Figure 16. (a) Is the dispersion curve for the current prism in the CTEx optical system. 29

Figure 17. Comparison of reconstructed images using the current and proposed prism design at 400 nm. 29

Page

Figure 18. The reconstruction tool. 33

Figure 19. The analysis tool. 34

Figure 20. A monochromatic hypercube using a point source and three reconstructed images at three wavelengths. 41

Figure 21. A monochromatic hypercube using a small letter reconstructed at three wavelengths. 42

Figure 22. The initial target hypercube that contains five images of the first five letters of the alphabet each at different wavelengths. 44

Figure 23. A hypercube that contains five images of the first five letters of the alphabet each at different wavelengths. 45

Figure 24. Five shifted projections of a hypercube containing five wavelength specific images. 47

Figure 25. Three 2x2 matrixes demonstrating the placement technique used in Shift and Place. 48

Figure 26. Comparison on the reconstruction results of Back Projection and Shift and Place. 51

Figure 27. Comparison on the reconstruction results of Back Projection and Shift and Place as in Figure 26, but displayed on a log scale. 52

Figure 28. A Side by side comparison of the reconstructed images 53

Figure 29. Basic images used in the target hypercube. 56

Figure 30. Example plot of how the range and number of prism angles impact reconstructed image quality. 58

Figure 31. Results summary of monochromatic targets with prism angle range of 360 degrees. 59

Figure 32. Results summary of 100 nm spaced images with prism angle range of 360 degrees. 60

Figure 33. Results summary of 20 nm spaced images with prism angle range of 360 degrees. 60

Page

Figure 34. Results summary of 10 nm spaced images with prism angle range of 360 degrees. 61

Figure 35. Results summary of 5 nm spaced images with prism angle range of 360 degrees. 61

Figure 36. Results summary of 1 nm spaced images with prism angle range of 360 degrees. 62

Figure 37. Results summary of point-like source with constant intensity. 63

Figure 38. Results summary of point-like source with random intensity with prism angle range of 360 degrees. 63

Figure 39. Results summary of capital letters with constant intensity with prism angle range of 360 degrees. 64

Figure 40. Results summary of capital letters with random intensity with prism angle range of 360 degrees. 64

Figure 41. Results summary of backlit AF bar chart with constant intensity with prism angle range of 360 degrees. 65

Figure 42. Results summary of backlit AF bar chart with random intensity with prism angle range of 360 degrees. 65

Figure 43. Results summary of front lit AF bar chart with constant intensity with prism angle range of 360 degrees. 66

Figure 44. Results summary of front lit AF bar chart with random intensity with prism angle range of 360 degrees. 66

Figure 45. Results summary of 400 by 400 random intensity with prism angle range of 360 degrees. 67

Figure 46. Comparison of Back Projection and Shift and Place using point like source with constant intensity target hypercube, 20 nm separation. 69

Figure 47. Comparison of Back Projection and Shift and Place using point like source with random intensity target hypercube, 20 nm separation. 69

Figure 48. Comparison of Back Projection and Shift and Place using letter with constant intensity target hypercube, 20 nm separation. 70

Page

Figure 49. Comparison of Back Projection and Shift and Place using letter with random intensity target hypercube, 20 nm separation. 70

Figure 50. Comparison of Back Projection and Shift and Place using backlit AF Bar chart with constant intensity target hypercube, 20 nm separation. 71

Figure 51. Comparison of Back Projection and Shift and Place using backlit AF Bar chart with random intensity target hypercube, 20 nm separation. 71

Figure 52. Comparison of Back Projection and Shift and Place using front lit AF Bar chart with constant intensity target hypercube, 20 nm separation. 72

Figure 53. Comparison of Back Projection and Shift and Place using front lit AF Bar chart with random intensity target hypercube with 20 nm separation. 72

Figure 54. Comparison of Back Projection and Shift and Place using 400x400 random intensity target hypercube, 20 nm separation. 73

Figure 55. Comparison of Back Projection and Shift and Place using point like source with constant intensity, 5 nm separation. 74

Figure 56. Comparison of Back Projection and Shift and Place using point like source with random intensity, 5 nm separation. 74

Figure 57. Comparison of Back Projection and Shift and Place using letter with constant intensity, 5 nm separation. 75

Figure 58. Comparison of Back Projection and Shift and Place using letter with random intensity, 5 nm separation. 75

Figure 59. Comparison of Back Projection and Shift and Place using backlit AF bar chart with constant intensity, 5 nm separation. 76

Figure 60. Comparison of Back Projection and Shift and Place using backlit AF bar chart with random intensity, 5 nm separation. 76

Figure 61. Comparison of Back Projection and Shift and Place using front lit AF bar chart with constant intensity, 5 nm separation. 77

Figure 62. Comparison of Back Projection and Shift and Place using front lit AF bar chart with random intensity, 5 nm separation. 77

Page

Figure 63. Comparison of Back Projection and Shift and Place using 400x400 pixel random intensity, 5 nm separation. 78

Figure 64. Comparison of an initial image to the Zernike image and reconstructed image. 80

Figure 65. Optical aberration evaluation using image type letter with constant intensity, Zernike polynomial number 4. 81

Figure 66. Optical aberration evaluation using image type letter with random intensity, Zernike polynomial number 4. 81

Figure 67. Optical aberration evaluation using image type backlit AF bar chart with constant intensity, Zernike polynomial number 4. 82

Figure 68. Optical aberration evaluation using image type backlit AF bar chart with random intensity, Zernike polynomial number 4. 82

Figure 69. Optical aberration evaluation using image type front lit AF bar chart with constant intensity, Zernike polynomial number 4. 83

Figure 70. Optical aberration evaluation using image type front lit AF bar chart with random intensity, Zernike polynomial number 4. 83

Figure 71. Optical aberration evaluation using image type letter with constant intensity, Zernike polynomial number 5. 85

Figure 72. Optical aberration evaluation using image type letter with random intensity, Zernike polynomial number 5. 85

Figure 73. Optical aberration evaluation using image type backlit AF bar chart with constant intensity, Zernike polynomial number 5. 86

Figure 74. Optical aberration evaluation using image type backlit AF bar chart with random intensity, Zernike polynomial number 5. 86

Figure 75. Optical aberration evaluation using image type front lit AF bar chart constant intensity, Zernike polynomial number 5. 87

Figure 76. Optical aberration evaluation using image type front lit AF bar chart with random intensity, Zernike polynomial number 5. 87

Page

Figure 77. Optical aberration evaluation using image type letter with constant intensity, Zernike polynomial number 7. 89

Figure 78. Optical aberration evaluation using image type letter with random intensity, Zernike polynomial number 7. 89

Figure 79. Optical aberration evaluation using image type backlit AF bar chart with constant intensity, Zernike polynomial number 7. 90

Figure 80. Optical aberration evaluation using image type backlit AF bar chart with random intensity, Zernike polynomial number 7. 90

Figure 81. Optical aberration evaluation using image type front lit AF bar chart with constant intensity, Zernike polynomial number 7. 91

Figure 82. Optical aberration evaluation using image type front lit AF bar chart with random intensity, Zernike polynomial number 7. 91

Figure 83. Optical aberration evaluation using image type letter with constant intensity, Zernike polynomial number 9. 93

Figure 84. Optical aberration evaluation using image type letter with random intensity, Zernike polynomial number 9. 93

Figure 85. Optical aberration evaluation using image type backlit AF bar chart with constant intensity, Zernike polynomial number 9. 94

Figure 86. Optical aberration evaluation using image type backlit AF bar chart with random intensity, Zernike polynomial number 9. 94

Figure 87. Optical aberration evaluation using image type front lit AF bar chart with constant intensity, Zernike polynomial number 9. 95

Figure 88. Optical aberration evaluation using image type front lit AF bar chart with random intensity, Zernike polynomial number 9. 95

Figure 89. Reconstructed image quality of monochromatic point-like source with constant intensity. 100

Figure 90. Reconstructed image quality of monochromatic point-like source with random intensity. 100

Page

Figure 91. Reconstructed image quality of monochromatic letter with constant intensity. 101

Figure 92. Reconstructed image quality of monochromatic letter with random intensity. 101

Figure 93. Reconstructed image quality of monochromatic backlit bar chart with constant intensity. 102

Figure 94. Reconstructed image quality of monochromatic backlit bar chart with random intensity. 102

Figure 95. Reconstructed image quality of monochromatic front lit bar chart with constant intensity. 103

Figure 96. Reconstructed image quality of monochromatic front lit bar chart with random intensity 103

Figure 97. Reconstructed image quality of monochromatic random intensity 400x400 pixel image. 104

Figure 98. Reconstructed image quality of point like source with constant intensity, 100 nm separation. 104

Figure 99. Reconstructed image quality of point like source with random intensity, 100 nm separation. 105

Figure 100. Reconstructed image quality of letter with constant intensity, 100nm separation. 105

Figure 101. Reconstructed image quality of letter with random intensity, 100 nm separation. 106

Figure 102. Reconstructed image quality of backlit bar chart with constant intensity, 100 nm separation. 106

Figure 103. Reconstructed image quality of backlit bar chart with random intensity, 100 nm separation. 107

Figure 104. Reconstructed image quality of front lit bar chart with constant intensity, 100 nm separation. 107

Page

Figure 105. Reconstructed image quality of front lit bar chart with random intensity, 100 nm separation. 108

Figure 106. Reconstructed image quality of random 400x400 pixel, 100 nm separation. 108

Figure 107. Reconstructed image quality of point-like source with constant intensity, 20 nm separation. 109

Figure 108. Reconstructed image quality of point-like source with random intensity, 20 nm separation. 109

Figure 109. Reconstructed image quality of letter with constant intensity, 20 nm separation. 110

Figure 110. Reconstructed image quality of letter with random intensity, 20 nm separation. 110

Figure 111. Reconstructed image quality of backlit AF bar chart with constant intensity, 20 nm separation. 111

Figure 112. Reconstructed image quality of backlit AF bar chart with random intensity, 20 nm separation 111

Figure 113. Reconstructed image quality of front lit AF bar chart with random intensity, 20 nm separation. 112

Figure 114. Reconstructed image quality of random intensity 400x400 pixels with 20 nm separation. 113

Figure 115. Reconstructed image quality of point like source with constant intensity, 10 nm separation 113

Figure 116. Reconstructed image quality of point like source with random intensity, 10 nm separation 114

Figure 117. Reconstructed image quality of letter with constant intensity, 10 nm separation 114

Figure 118. Reconstructed image quality of letter with random intensity, 10 nm separation 115

Page

Figure 119. Reconstructed image quality of backlit AF bar chart with constant intensity, 10 nm separation 115

Figure 120. Reconstructed image quality of backlit AF Bar chart with random intensity, 10 nm separation 116

Figure 121. Reconstructed image quality of front lit AF bar chart with constant intensity, 10 nm separation 116

Figure 122. Reconstructed image quality of front lit AF bar chart with random intensity, 10 nm separation 117

Figure 123. Reconstructed image quality of random intensity 400x400 pixel, 10 nm separation 117

Figure 124. Reconstructed image quality of point like source with constant intensity, 5 nm separation 118

Figure 125. Reconstructed image quality of point like source with random intensity, 5 nm separation 118

Figure 126. Reconstructed image quality of letter with constant intensity, 5 nm separation 119

Figure 127. Reconstructed image quality of letter with random intensity, 5 nm separation 119

Figure 128. Reconstructed image quality of backlit AF bar chart with constant intensity, 5 nm separation 120

Figure 129. Reconstructed image quality of backlit AF bar chart with random intensity, 5 nm separation 120

Figure 130. Reconstructed image quality of front lit AF bar chart with constant intensity, 5 nm separation 121

Figure 131. Reconstructed image quality of front lit AF bar chart with random intensity, 5 nm separation 121

Figure 132. Reconstructed image quality of random intensity image, 5 nm separation 122

Figure 133. Reconstructed image quality of point source with constant intensity, 1 nm separation 122

Page

Figure 134. Reconstructed image quality of point source with random intensity, 1 nm separation 123

Figure 135. Reconstructed image quality of letter with constant intensity, 1 nm separation 123

Figure 136. Reconstructed image quality of letter with random intensity, 1 nm separation 124

Figure 137. Reconstructed image quality of backlit AF bar chart with constant intensity, 1 nm separation 124

Figure 138. Reconstructed image quality of backlit AF bar chart with random intensity, 1 nm separation 125

Figure 139. Reconstructed image quality of front lit AF bar chart with constant intensity, 1 nm separation 125

Figure 140. Reconstructed image quality of front lit AF bar chart with random intensity, 1 nm separation 126

Figure 141. Reconstructed image quality of random 400x400 intensity image, 1 nm separation 126

List of Tables

Page

Table 1: The first nine Zernike polynomials defined in Zemax for a Zernike Fringe Phase Mask representing up to third order optical aberrations. [20] 18

Table 2: Zemax Image Simulation Settings Used In Experiment..... 31

Table 3: Initial target configuration table. Identifies the spatial and spectral configuration of the initial target hypercubes and how many images were used. With the exception of the monochromatic configurations all spectral spacing is centered on 600 nm..... 55

COMPARATIVE ANALYSIS OF RECONSTRUCTED IMAGE QUALITY IN A SIMULATED CHROMOTOMOGRAPHIC IMAGER

I. Introduction

This thesis presents a physics-based model of the chromotomographic experiment (CTEx) developed by the Air Force Institute of Technology (AFIT). The simulation and optical model was constructed using Zemax and MATLAB.

The model was used to explore three parameters associated with the reconstructed image quality. The first was to determine how the prism angle selection impacts the reconstructed image quality. The second was to evaluate a new reconstruction algorithm which attempts to identify and remove off wavelength artifacts improve the reconstructed image quality. The third area looks at a how optical aberrations impact the reconstructed image quality in which four different optical aberrations were used in the form of Zernike polynomials.

In addition to the optical model, three other software tools were developed in MATLAB. The first was a reconstruction program that enables multiple reconstruction algorithms to be used. The second was an analysis tool to assist in evaluating the reconstructed image quality. The third was a conversion tool that converts GCTEx experimental data file format to enable it to be used with the reconstruction tool and viewed with the analysis tool. All three of the software tools were designed to be modular and function like a hub connecting the principle components of the optical design, reconstruction algorithms, and evaluation. This design enables new optical designs and reconstruction algorithms to be quickly tested and evaluated.

The model helped identify a distortion-like effect in the current prism design. This effect is more pronounced in the shorter wavelengths and increases as a function of radial distance from the optical axis of the system. Due to this effect a new prism design was modeled and used during the course of this work.

1.1 Motivation

Hyperspectral imagers (HSI) record both the spatial and spectral energy distribution of a scene. Several traditional HSI's exist in the field today which typically operates with either a scanned-slit or optical-filtered mechanism. Both techniques are capable of producing high quality hyperspectral images but due to their recording mechanism are inherently slow. This weakness makes them ill-suited in recording quickly varying scenes.

Chromotomographic instruments utilize a dispersive element such as a direct vision prism (DVP) to capture both the spatial and spectral energy distribution simultaneously. Combined with a high speed camera, chromotomographic instruments have the potential of recording quickly varying scenes. This ability to record quickly varying scenes could be used in applications such as recording bomb explosions to determine their chemical composition from their spectrum. These gains come at a cost in terms of the complexity and time required in the reconstruction algorithms and suffers from image degradation due to artifacts introduced by the reconstruction algorithms.

1.2 Research Goals

This research aims to complement previous work undertaken by AFIT and has the end goal of assisting in determining the necessary design parameters required to achieve a specified performance capability. Specific goals include:

- Develop a tool set to expedite evaluation of future CTEx designs and reconstruction algorithms.
  - Provide users a GUI interface which saves the settings used.
  - Enable batch and parallel processing.
  - Provide automatic file and directory management
- Evaluate a new CTEx optical design.
- Evaluate how the range of prism angles and number of projections used in the reconstruction impacts the reconstructed image quality.
- Evaluate a new reconstruction algorithm.
- Evaluate the impact of optical aberrations to the reconstructed image quality.

1.3 Organization

Chapter 2 provides an overview of the basic theory of chromotomography, its origins in the medical community, and how the Shift and Add reconstruction algorithm works. It also describes the fundamental information limit imposed by the limited angle problem. In Chapter 3, the experiment methodology is discussed as well as the MATLAB tools that were developed for the simulation, reconstruction, and analysis. This chapter contains the details of the optical model in Zemax and the proposed prism geometry. The cross correlation function is described showing how the target images are compared to the reconstructed images. It concludes with why the new reconstruction

algorithm was developed and how it operates. Chapter 4 starts with the basic target designs that will be used in the assessment of the three areas of investigation. These areas of investigation include the angle range and number of projections used in the reconstruction, comparisons of the new reconstruction algorithm to the Back Projection, and the impact of optical aberrations. Chapter 5 summarizes the results and makes recommendations for future research.

II. Background

This chapter serves to provide a foundational understanding of chromotomography. It starts by defining what hyperspectral imaging is. It then describes tomography in general, the origins of computed tomography in the medical field, and the fundamental principles of chromotomography. An overview of a basic reconstruction algorithm is then provided. The mathematical basis in which chromotomography operates is presented as well as the central slice theorem, which is the fundamental limiting factor of how much information can be ascertained from projections. This chapter concludes with a brief summary of how optical aberrations are formed, their classifications, and how they can be represented in the simulation.

2.1 Hyperspectral Remote Sensing

Imaging systems record the spatial distribution of the electromagnetic power in a scene. Spectrometry measures the power variation with respect to wavelength or frequency. Spectrometry is used in diverse fields ranging from astronomy to molecular biology because it is a highly effective way to determine the chemical composition of a given material or substance. The combination of imaging and spectrometry is known as hyperspectral imaging.

Hyperspectral imaging records two spatial dimensions and a third dimension of spectral information. This combination of two spatial dimensions and a third spectral dimension gives rise to a three dimensional data structure commonly referred to as a hypercube. Depicted in Figure 1 a hypercube can be visualized as a stack of two

dimensional images in which each image contains the spatial distribution for a specific wavelength band or bin.

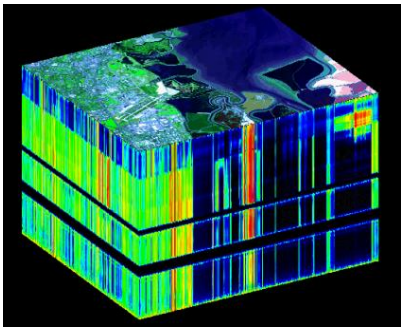

Figure 1. This is a classic spectral hypercube in which each layer contains the spatial distribution for a different wavelength bin or frequency band. On the top surface all of the layers are superimposed forming the image of a landscape. [7]

Perhaps the two most common methods of hyperspectral imaging are the scanning and filter techniques. The scanned, or slit, method breaks the scene up into slices and records all of the spectral information for one spatial slice at a time. The filter method takes multiple images of the object in which each image captures a different wavelength band. In both cases the only two dimensions are recorded at a time and because of this fact these techniques are inherently slow. Chromotomography is unique in that it records both the spatial and spectral information simultaneously. Figure 2 graphical depicts the three hyperspectral imaging techniques discussed.

2.2 Computed Tomography Origins

Tomography seeks to use lower dimensional projections of an object to define the higher dimensional object and has its origins in the medical industry with the advent of x-ray machines. X-ray machines are used to take images of internal structures of an object by sending a set amount of radiation into the object. The x-ray image shows only the

total amount of energy that successfully transmitted through the object in two dimensions but not where it was absorbed in the third dimension of space.

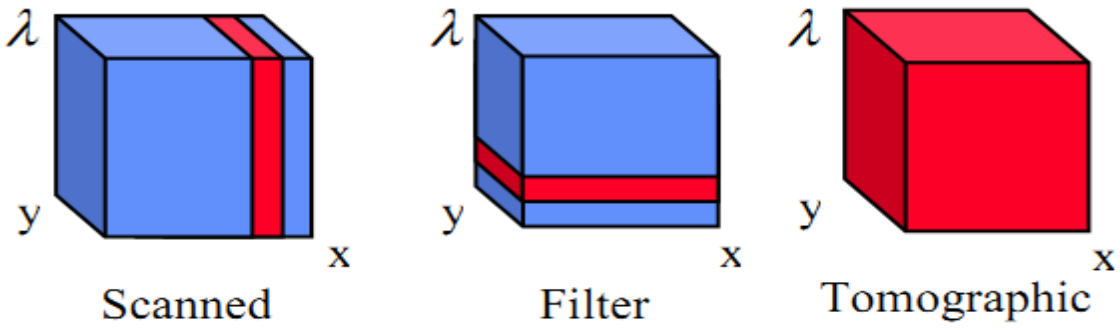

(a) **(b)** **(c)**

Figure 2. Graphical representation of different scanning techniques. (a) Represents the Scanning method. (b) Represents the Filter method. (c) Represents the Tomographic technique. [11]

For example, a chest x-ray will show the cumulative radiation absorbed of a person's ribs, lungs, and heart. The x-ray image defines where the objects are positioned in two dimensions of space but does not contain any information about their location in the third dimension of space. In principle the heart and lungs could be sitting inside or outside the person's body. If the organs were otherwise properly aligned the x-ray image would show the same result. While this particular example is extreme it does illustrate the inherent weakness of single x-ray images which, in part, led to the development of tomography.

An x-ray image can be considered a two dimensional projection of a three dimensional object. Tomography seeks to take multiple projections, in this case two dimensional x-ray images, to determine information concerning the three dimensional

object. Attempts were made, even without the assistance of computers, to use multiple projections to further define the three dimensional objects being imaged with x-rays. This idea of using lower dimensional projections to define objects of higher dimensions is the basis of tomography and its concepts were patented by Gabriel Frank in 1940 [8].

Consider the x-ray example again but suppose two images are now used to determine the 3D object. The first image of a person's chest straight on and the second image taken when the person, or x-ray machine, has been rotated 90 degrees. Each image is a two dimensional projection but between the two images all three spatial dimensions, at least in part, can be observed. Since both images are projections of the same object they can both be used to define the object's structure far more than either image alone. The placement of the person's ribs, lungs, and heart can now be determined definitively. With the advent of computers came computed tomography (CT). With the help of computers virtually any number of projections can be used to define an object by means of advanced reconstruction algorithms.

2.3 Fundamental Principles of Chromotomography

Chromotomography works on the same principle as x-ray tomography in that it takes projections to create a hypercube. A typical chromotomographic instrument used in tomography is depicted in Figure 3.

This is similar to x-ray tomography but there are some key differences. The first primary difference is what the three dimensions represent. In the case of x-ray tomography all three dimensions are spatial. In chromotomography only two dimensions are spatial and the third is spectral.

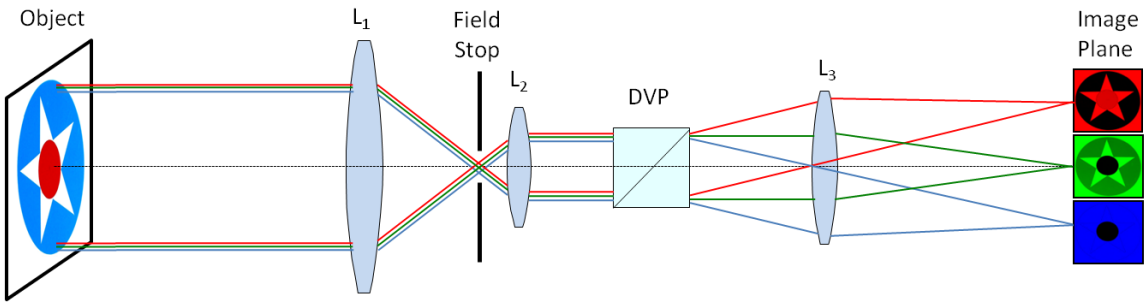

Figure 3. A typical chromotomographic instrument. The first two lenses are used to collimate the light. The light is then dispersed by the dispersive element and then focused by the third lens onto the focal plane array. The resultant image is a two dimensional projection of the three dimensional object. By rotating the direct vision prism, multiple projections can be recorded and used in a reconstruction algorithm to create a hypercube.

The second major difference is how the projections are produced. In the case of x-ray tomography the object is imaged at differing angles, but in chromotomography the projections are produced by a dispersive element. The dispersive element greatly reduces the total number of angles available to produce the projections. The hypercube projections are depicted in Figure 4.

The strength of using chromotomography as a hyperspectral imager is the time required to record the hypercube projections is typically faster than the scanning or slit method. In addition chromotomography is always recording the entire scene rather than only a portion of it at a time. This provides superior situational awareness as any changes in the scene can be identified. The cost of using projections is that the reconstruction algorithms used to build the hypercube are more complicated and the ultimate performance of the system is limited by the number of projection angles available.

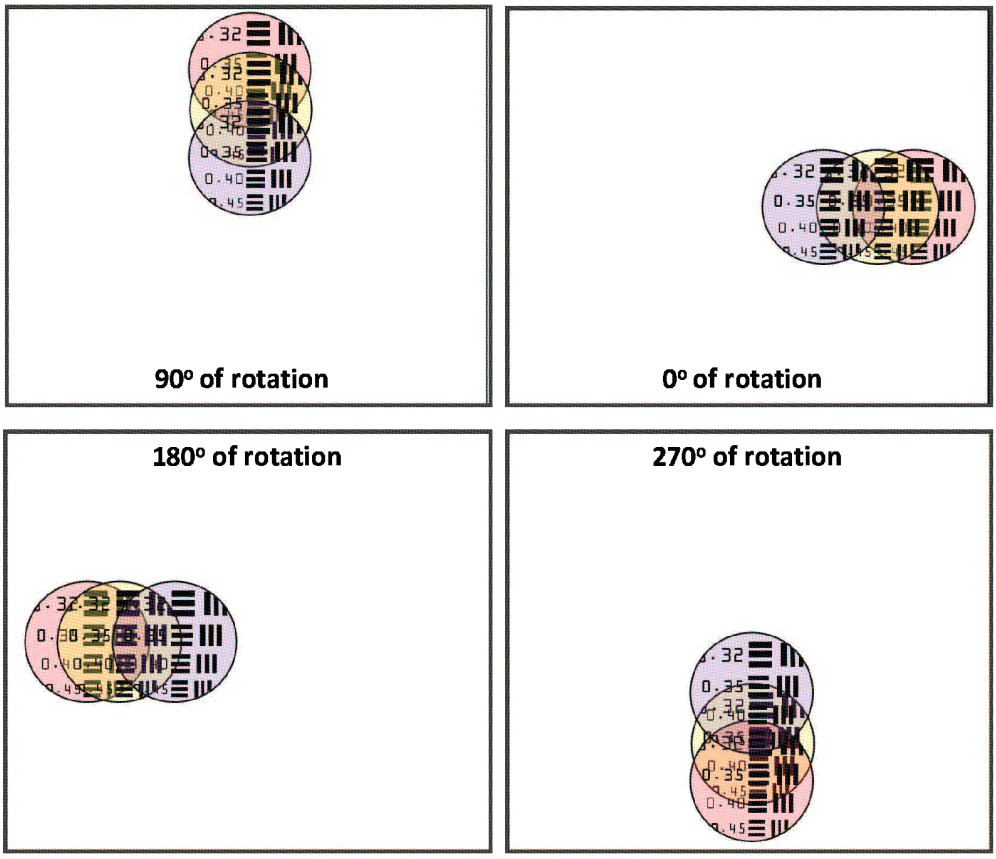

Figure 4. Each box contains a recorded image and contains a unique projection of a segment of an Air Force Bar Chart in which three wavelengths are present. The displacement of each image is a function of wavelength but the direction of the displacement is determined by the prism angle. [12]

2.4 Basic Reconstruction Algorithm

Once the projections are recorded they are processed through a reconstruction algorithm. The primary purpose of these algorithms is to take the recorded images, two dimensional projections, and create a three dimensional hypercube. Several reconstruction algorithms have been developed but perhaps the easiest to understand is the Shift and Add technique.

The Shift and Add reconstruction algorithm takes advantage of the fact that the dispersive element displaces each image in the hypercube a unique distance based on

wavelength and the direction determined by the prism angle. The Shift and Add technique takes the recorded projections and shifts each image a set distance along the prism angle and sums all of the shifted images together. When these new shifted images align, it represents an image from the object hypercube. By knowing the prism characteristics the displacement distance can be associated with a wavelength. This process is repeated to find all of the images in the target hypercube as seen in Figure 5.

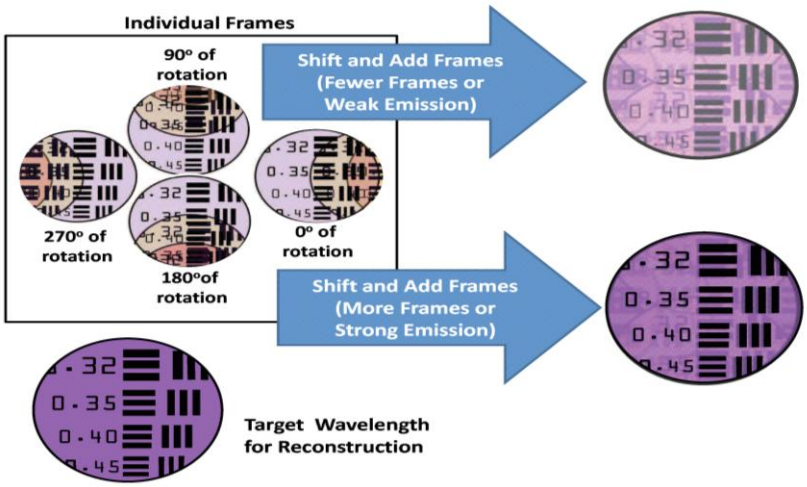

Figure 5. This depicts the Shift and Add reconstruction algorithm. [12] In the box are four recorded projections or frames of a portion of an AF Bar chart in which three wavelengths are visible. Outside the box are images produced by shifting and adding the projections on one of the hypercube wavelengths in which a set of images align. The artifacts from the other wavelengths are more pronounced when only a limited number of projections are used. The impact of these artifacts is reduced as the number of projections is increased.

2.5 Mathematical Basis of Chromotomography

This research is based on mathematics described by Mooney. This section provides an overview of the work he completed in [10]. The unique distance by which the prism displaces the images is described by the System Transfer Function (STF). The STF is a matrix that contains the location of the spectral Point Spread Function (PSF)

created by the prism. In Equation 1, $f(x, y, \lambda)$ represents the original initial target hypercube that is being imaged through the chromotomographic instrument. The variables *x* and *y* are the spatial coordinates of the hyperspectral image. Hyperspectral images are three dimensional images in which λ represents the spectral coordinate or wavelength of the hyperspectral image. The response of the prism is provided by *k(λ)* and prism angle is given by ϕ.

Based on the angle and the spectral response of the prism each image in the target hypercube is dispersed a unique distance. Mooney showed that the superposition of the dispersed images produces a projection. Mathematically this can be written as a convolution of *f(x, y, λ)* with the prism's PSF over λ, or

$$g(x, y, \phi) = \int_{-\infty}^{\infty} f(x, y, \lambda) ** \delta(x - k(\lambda)\cos(\phi), y - k(\lambda)\sin(\phi)) d\lambda, \quad (1)$$

where '**' is the symbol for a two dimension convolution. A more compact way of representing Equation 1 is

$$g(\bar{x}, \phi) = \int_{-\infty}^{\infty} f(\bar{x} - k(\lambda)\bar{p}_{\phi}, \lambda) d\lambda, \quad (2)$$

where $(\bar{x}) = (x, y)$ and $\bar{p}_{\phi} = (\cos(\phi), \sin(\phi))$.

Fourier Transforms can be used to simplify the convolution in Equation 1. Using a 2D Fourier transforms Deming [2] was able to turn Equation 2 into Equation 3. The variable $\bar{\xi}$ is the transformed coordinates of $\bar{x}$ and $\bar{\xi} \cdot \bar{p}_{\phi}$ is a vector dot product. The transformed functions are represented using the capital letters of the original functions as seen in

$$G(\bar{\xi},\phi) = \int_{-\infty}^{\infty} \exp[-2\pi k(\lambda)\bar{\xi}\cdot\bar{p}_{\phi}]F(\bar{\xi},\lambda)d\lambda \ . \tag{3}$$

The simulation cannot truly represent continuous functions. The best it can do is sample the image both spatially and spectrally. As a result the integral can be converted into a summation so Equation 3 can be turned into

$$G_m(\bar{\xi}) = \sum_{n=0}^{N-1} \exp[-2\pi n\bar{\xi}\cdot\bar{p}_m]F_n(\bar{\xi},\lambda)\Delta\lambda \, . \tag{4}$$

In Equation 4, *m* is the integer representing the projection, *n* is an integer representing a spectral band, and *M* is the number of projections. The variable $\bar{p}_m$ is defined as $(\cos(2\pi m/M),\sin(2\pi m/M))$. In Fourier Space Equation 4 can be represented as $G(\bar{\xi}) = A(\bar{\xi})F(\bar{\xi})$ in which $A(\bar{\xi})$ is the STF. If we know $A(\bar{\xi})$ and are able to record $G(\bar{\xi})$ then $F(\bar{\xi})$ can be solved for by taking A^H and multiplying both sides of $G(\bar{\xi}) = A(\bar{\xi})F(\bar{\xi})$ we get $F'(\bar{\xi},\lambda)$ which equals

$$F'(\bar{\xi},\lambda) = [A^H G](\bar{\xi},\lambda) = \int_0^{2\pi} \exp[2\pi ik(\lambda)\bar{\xi}\cdot\bar{p}_{\phi}]G(\bar{\xi},\phi)d\phi \, . \tag{5}$$

An Inverse Fourier Transform can then be applied to $F'(\bar{\xi},\lambda)$ in order to convert the function back from frequency space to regular space to provide $f'(x,y,\lambda)$.

At this point a large number of images have been identified. For clarity the following list has been established to provide the general description and mathematical representation.

- Initial target hypercube.
    - A 3D image composed of a set of 2D images in which each 2D image has a unique wavelength associated with it.
    - $f(x, y, \lambda)$
- Wavelength specific image in the initial hypercube.
    - $f(x, y, \lambda_z)$, in which *z* specifies a wavelength.
- Single dispersed image or dispersed image.
    - A single wavelength specific image from the initial hypercube that has been imaged through the chromotomographic instrument.
    - g_i, in which *i* specifies a specific dispersed image.
- Recorded/Simulated Projection
    - The superposition of all of the dispersed images.
    - $g(\bar{x}, \phi)$
- Shifted Projection
    - The superposition of all of the dispersed images have been shifted by the reconstruction algorithm in the direction of the prism angle.
    - $g(\bar{x}, \phi)_{shifted}$
- Wavelength specific image in the reconstructed hypercube.
    - Created using projections in a reconstruction algorithm.
    - $f'(x, y, \lambda_z)$, in which z identifies a specific wavelength.
- Reconstructed hypercube.
    - A 3D image composed of a set of 2D images in which each 2D image has been created using a reconstruction algorithm and recorded/simulated projections.
    - $f'(x, y, \lambda)$

Figure 5 and Equation 5 suggest that with enough projections the initial hypercube could be fully defined. Unfortunately, as mentioned earlier, the number of angles available in chromotomography is limited because of the way the projections are created, namely the dispersive element. This is known as the limited angle problem [9] and is the single greatest limiting factor in chromotomography. The impact of the limited angle problem combined with the central slice theorem sets the stage for what is known as the "cone of missing information".

2.5.1 Cone of Missing Information

Fourier transforms and inverse Fourier transforms provide the ability to change the domain in which an object is represented. It changes an object's description from the space domain to the frequency domain or vice versa. A key point is that whether an object is described in the space domain or in the frequency domain it is still the same object being described. Real world objects that can be fully described in one domain can typically be fully described in the other domain as well. Objects described in one dimensional space are described in one dimensional frequency domains just as objects described in two dimensional spaces are described in two dimensional frequency space.

The Fourier slice or central slice theorem relates where the information contained in the projections is located in frequency space.

Definition. *The Fourier transform of a parallel projection of an object f(x, y) obtained at an angle θ equals a line in a 2D Fourier transform of f(x, y) taken at the same angle*. [8]

An important point about the definition is that the line that is referred to will always go through the origin. Let's consider the implications of this statement first using

one dimensional projections to reconstruct a two dimensional object. In this case the information contained in a one dimensional projection is represented as a line in a two dimensional frequency domain that passes through the origin that is perpendicular to the projection direction. In theory an infinite number of projections taken at an infinite number of angles would produce an infinite number of lines filling in the entire frequency domain. Once this information has been collected an inverse Fourier transform can be applied to describe the object in the space domain.

Extending this to three dimensions a similar scenario is observed but contains one major exception. Now the two dimensional projections are taken and used to reconstruct a three dimensional object. The information contained in the two dimensional projection is represented as a plane in three dimensional frequency space that passes through the origin. In theory, if an infinite number of projections were taken then an infinite number of planes would pass through the origin and all of the information in frequency space would be known. An inverse Fourier transform could then be used to fully describe an object in the space domain.

There is a limit to how many projection angles are available because of the fixed properties of the system. As a result there is always information in the frequency space that is unknown. Furthermore because each projection's information is described as a plane that passes through the origin and is perpendicular to the projection direction in a three dimensional frequency space, one can imagine that all of the intersecting planes would sweep out a cone shape in frequency space as seen in Figure 6. This inability to describe an object fully in frequency domain directly limits how well an object can be described in the space domain.

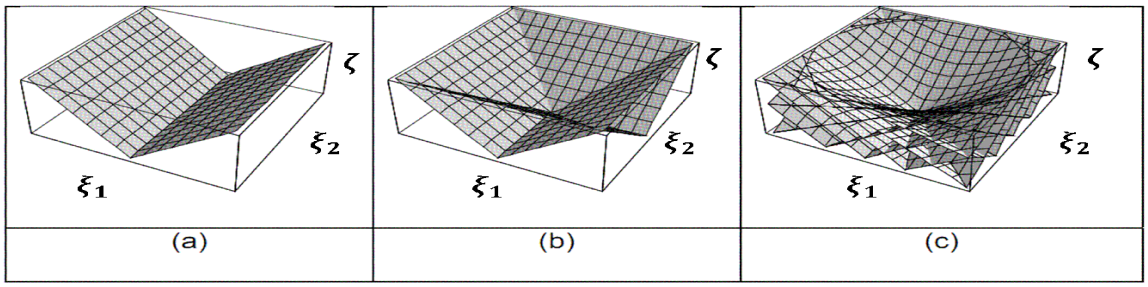

Figure 6. Represents information recorded in the frequency domain. (a) Represents the information distribution in the frequency domain of two projections. (b) Represents the information distribution in the frequency domain of three projections. (c) Represents the information distribution in frequency space in the limit of a large number of projections. [3]

2.6 Optical Aberrations

Chromotomographic instruments are imaging devices and as such are susceptible to optical aberrations. Maxwell formulated three conditions that must be met in order for a lens to produce a perfect geometric image. The first condition is that all rays emanating from a point J in object space that pass through the lens must also go through the point J' in image space. [4] Violation of this principle results in optical aberrations. All real world optical components suffer from optical aberrations to varying degrees. The best any imaging system can do is focus the rays from a point in object space down to a minimal spot size, not an infinitesimal point. Aberrations are classified as either monochromatic or chromatic.

Monochromatic aberrations impact all wavelengths and are the result of optical component geometries in which rays in object space from point J have different optical path lengths to its associated image point J' [4]. Monochromatic aberrations arise when optical components operate in regions in which the paraxial approximation is no longer appropriate. These deviations from the paraxial approximation can be described in terms

of wavefront error. The Taylor series is an infinite series but fortunately using the first several terms in the series usually provides an excellent approximation because the series converges quickly. A third order approximation can generally be used to make accurate enough predictions for most applications.

One convenient way of describing optical aberrations is using Zernike polynomials, see Table 1. These are convenient for a number of reasons [14].

- Zernike polynomials are orthogonal functions and form a complete basis set.
- The first nine Zernike polynomials can represent first and third order optical aberrations.
- Typical laboratory instruments can measure the Zernike coefficients of optical components.
- Zemax enables optical aberrations to be incorporated into its image simulation function by specifying the Zernike polynomial coefficient inputted as a number of waves making them ideal to use in the simulation.

Table 1: The first nine Zernike polynomials defined in Zemax for a Zernike Fringe Phase Mask representing up to third order optical aberrations. [13]

Term #	n	m	Polynomial	Description
1	0	0	1	Piston
2	1	1	$\rho \cos \theta$	X-Tilt
3	1	-1	$\rho \sin \theta$	Y-Tilt
4	2	0	$2\rho^2 - 1$	Focus
5	2	2	$p^2 \cos 2\theta$	Astigmatism @ 0° off x-axis & Focus
6	2	-2	$p^2 \sin 2\theta$	Astigmatism @ 45° off x-axis & Focus
7	3	1	$(3\rho^2 - 2)\rho \cos \theta$	Coma & X-Tilt
8	3	-1	$(3\rho^2 - 2)\rho \sin \theta$	Coma & Y-Tilt
9	4	0	$6\rho^4 - 6\rho^2 + 1$	Spherical & Focus

III. Methodology

A robust and highly versatile simulation is essential to the continued success and development of chromotomography experiment (CTEx). The simulation provides AFIT the ability to design, test, and evaluate the CTEx system at a fraction of the cost of fabricating new optical components. In addition the simulation also provides greater capability in evaluating different target sets. The CTEx simulation uses Zemax and MATLAB.

The overall experiment was configured to run as a three stage process which starts with a target hypercube, $f(x, y, \lambda)$, that is processed in a chromotomographic instrument simulation. The simulation produces simulated projections or $g(\bar{x}, \phi)$ which can then be used to produce the reconstructed hypercube $f'(x, y, \lambda)$. The analysis stage compares the initial target hypercube, $f(x, y, \lambda)$, to the reconstructed hypercube, $f'(x, y, \lambda)$.

At each stage a MATLAB tool was designed to assist in execution in which the outputs of a previous stage are the inputs of the next. This has the advantage of speed because in many cases parallel and batch processing can be utilized. To enable each tool to work effectively and efficiently together a folder structure and standard file formats were established.

The benefit of using a modular design is that all of the foundational, non changing portions, serve as a hub which connects all of the major components. A file conversion tool was built to enable the actual recorded CTEx instrument data to be processed by the reconstruction tool and viewed in the analysis tool. This flexibility enables direct validation of the model.

3.1 Simulation

The simulation was written in both MATLAB and Zemax. MATLAB serves as a controller of Zemax and performs all of the housekeeping functions required to make Zemax successful. Zemax is responsible for performing the image simulation. MATLAB interfaces with Zemax by way of dynamic data exchange or DDE.

The simulation takes the initial target hypercube and optical model and processes them with Zemax's image simulation tool which will be discussed in more detail in Section 3.1.5. Each image in the target data cube, $f(x, y, \lambda_z)$, must be processed individually for each prism angle used in the simulation. It saves these images individually in the Zemax directory folder. Once all of the target images, $f(x, y, \lambda_z)$, have been simulated for each prism angle, MATLAB uploads the simulated images, g_i, and combines or sums all of the images for each prism angle to create the simulated projection image or $g(\bar{x}, \phi)$. This produces one image per angle. These simulated projections, $g(\bar{x}, \phi)$, can then be used in the reconstruction and analysis tools.

The interface between MATLAB and Zemax using DDE is limited because it can only exchange strings of data. Images cannot be sent directly from MATLAB to Zemax. Instead MATLAB takes the image file and places it into a directory accessible to Zemax as a bitmap. After the image has been saved, MATLAB then provides Zemax the path information to the bitmap image, tells Zemax to simulate the target image, and instructs Zemax where to save the new simulated image. This means that for every image simulated the hard drive is accessed five times.

3.1.1 Simulation Tool

The simulation tool was written in MATLAB and has a GUI interface in which the basic setup parameters are set. This includes selecting the Zemax model, MATLAB target file, and defining the detector size by specifying the number of pixels in the detector and the individual pixel length in microns. It also enables the first nine Zernike polynomial coefficients and prism rotation angle information to be entered. During the simulation this tool performs file management; uploading the optical model into Zemax, and updating values like the wavelength and prism angle. In addition it provides file conversion from MATLAB file format to the bitmap image format, changing the settings as required in the simulation, and recombining output images to produce the simulated recording as seen in Figure 7.

The simulation interface tool does not make the Zemax image simulation settings available. These parameters instead have been left in the simulation interface code and must be changed manually. It was designed this way because those settings can dramatically change the results of the simulation and processing time so they should be changed with caution.

3.1.2 Optical Model

The optical model was programmed in Zemax. Figure 8 depicts the optical model used to simulate the chromotomographic instrument. The first two lenses are used to collimate the light into the prism. The prism disperses the light. The third lens is then used to focus the light onto the focal plane array.

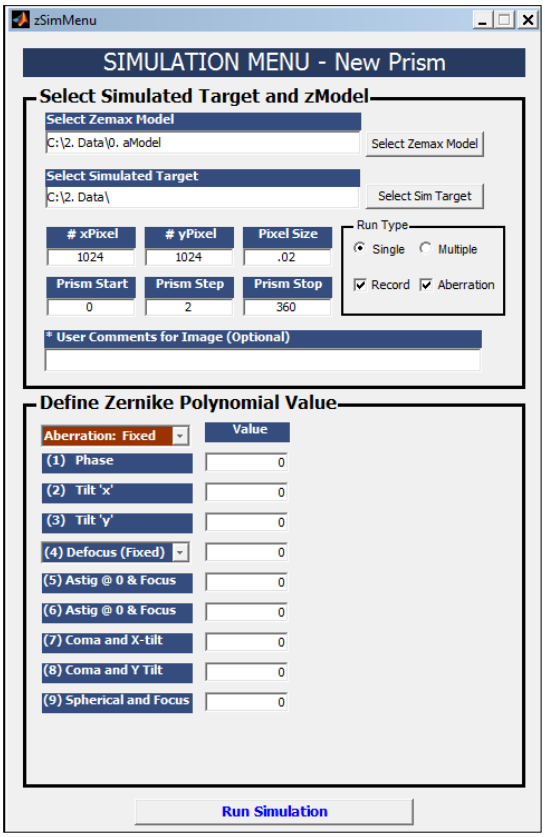

Figure 7. The simulation tool interface.

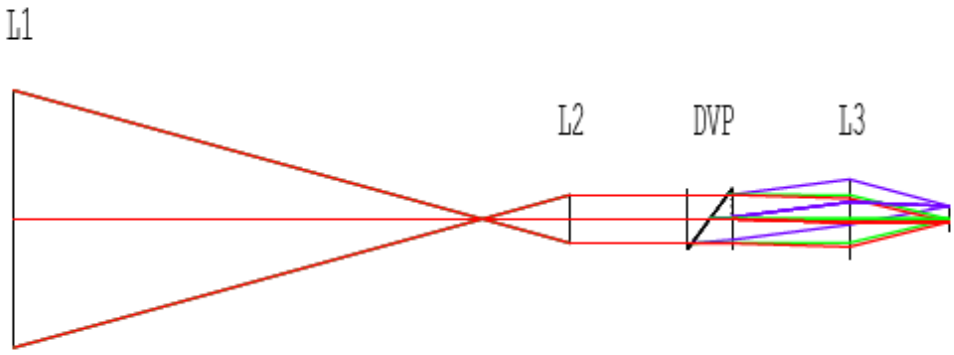

Figure 8. A standard chromotomographic optical model using paraxial lenses and direct vision prism. The first two lenses (L1 and L2) collimate the light into the direct vision prism or DVP. The third lens (L3) focuses the light onto the focal plane array. [12]

In addition, a Zernike mask is placed concurrently with the third lens and is used to set specific amounts of optical aberration into the system as Zernike coefficients. The Zernike mask enables the optical model to be very flexible in that it can be used to model virtually any combination of first and third order aberrations with any given CTEx instrument. Since the Zernike coefficients are defined in terms of number of waves the impact of the optical aberration is dependent upon wavelength of the image being simulated. Figure 9 demonstrates this.

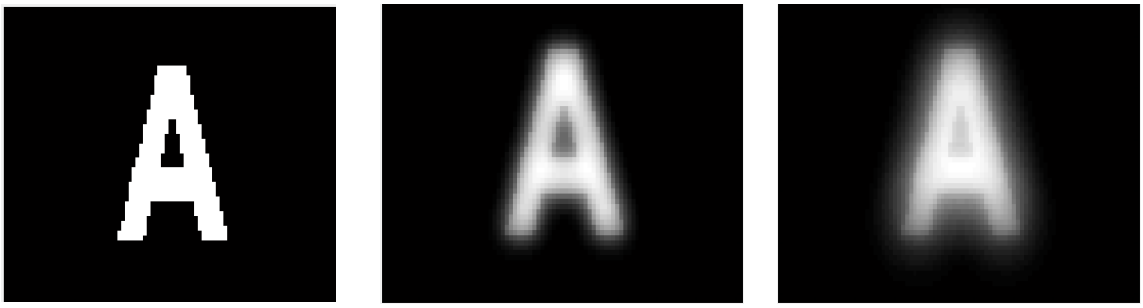

(a) **(b)** **(c)**

Figure 9. Comparison of optical aberration using same image at different wavelengths. (a) is the initial target image. (b) and (c) were individually processed through the Zemax simulation tool in which the same amount of optical aberration using the Zernike Mask were applied. The only difference between (b) and (c) in the simulation was that (b) was defined at 400 nm while (c) was defined at 800 nm.

3.1.3 Need for a New Prism Design

The optical model used in this project includes a proposed new prism design. The primary motivation to make this change was the discovery of a previously undetected distortion-like effect being introduced by the current prism geometry. The unwanted effect is an image magnification along a single axis that increases with the angle away from the optical axis. Since the prism is rotating, the axis of magnification is rotating as

well. The result is that each projection recorded, which has a unique prism angle, has been uniquely changed from the other projections in addition to being displaced in a different direction. This effect is particularly damaging when the recorded projections are used in the reconstruction algorithms to produce the hypercube. This effect is illustrated in Figure 10. Ideally the prisms dispersion curve would only depend on the wavelength of the light and would not depend on the radial distance from the optical axis. To verify if the current prism design dispersion curve was dependant on the wavelength and the radial distance from the optical axis the simulation was used to compare the dispersion curves of a on axis source to an off axis source. The on axis source had an angle of incidents of zero degrees while the off- axis source had an angle of incidents of 2.93 degrees. As seen in Figure 11 (a) the two dispersion curves are not the same and the difference between the two curves has a wavelength dependence in which the greatest difference is at 400 nm and cross each other at approximately 550 nm. Figure 11 (b) demonstrates the dispersion angle at a constant wavelength increases as the angle of incidents increase.

The Shift and Add method depends on each recorded projection to be displaced a set distance along the direction of the prism and works to shift each of the recorded projections back into alignment. If each projection is uniquely changed then it is no longer possible to realign the images as they are all different.

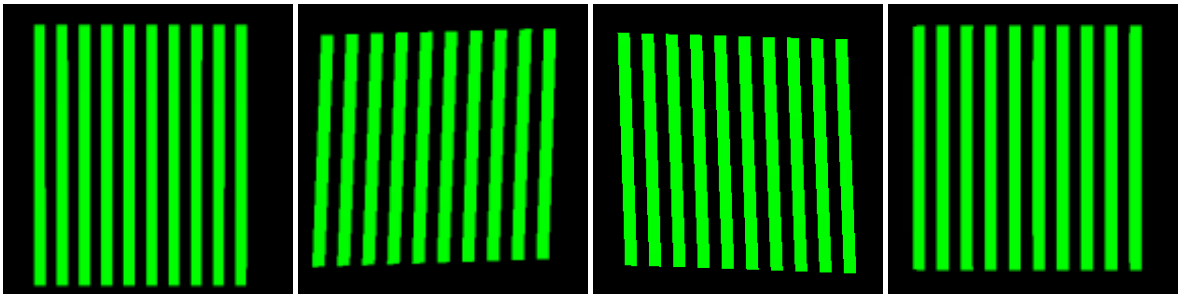

(a) **(b)** **(c)** **(d)**

Figure 10. Each image has been simulated in the Zemax Image Simulation tool using the same target image of vertical bars with the current CTEx optical model. The angles these images were simulated at are (a) at zero degrees, (b) at 45 degrees, (c) at -45 degrees, and (d) at 90 degrees. The prism is magnifying the image along the axis in which the prism is dispersing the images which gives the effect of the image being stretched in different directions.

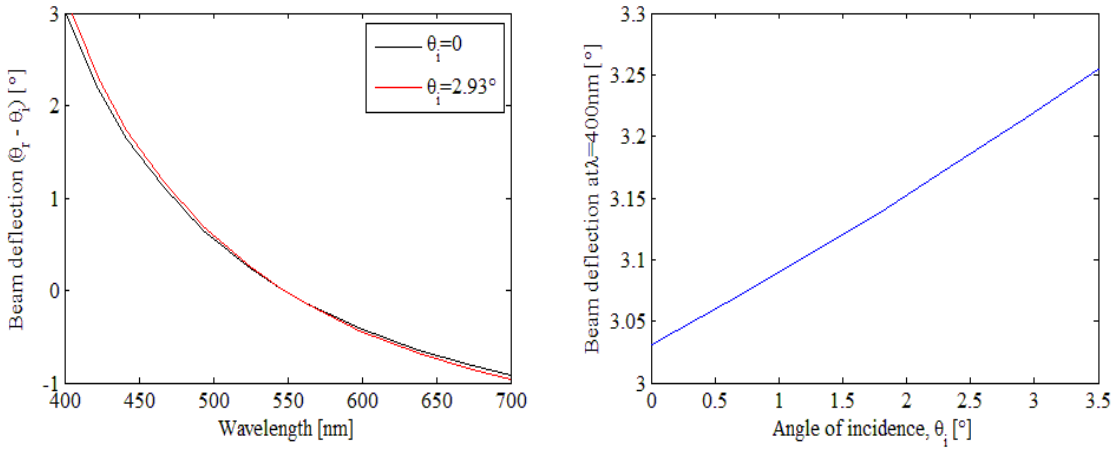

(a) **(b)**

Figure 11. Comparison of dispersion curves for an on axis source to an off axis source demonstrating the wavelength and location dependence. (a) Demonstrates the difference between the two curves is wavelength dependant. (b) Further demonstrates that the dispersion angle is highly sensitive to the angle of incidence in which as the angle of incident increases so does the dispersion angle.

Figure 12 shows the impact it can have on a reconstructed image at 400, 500, 600, and 700 nm. The results in Figure 12 are consistent with Figure 11 in that the reconstructed image at 400 nm is the worst. At 500 nm the image quality improves and by 600 nm the image quality does not show any visible sign of the distortion effects at all.

This correlates well to Figure 11 (a) in which the dispersion curve values are nearly identical around 500 to 600 nm. At 700 nm the image quality decreases only slight at the outer edges but is overall much better than the reconstructed image at the 400 nm. The radial dependence is seen in that the center portion of all of the reconstructed images does not look blurry. The only part of the image that is negatively impacted is sufficiently off axis for the distortion-like effects to become evident.

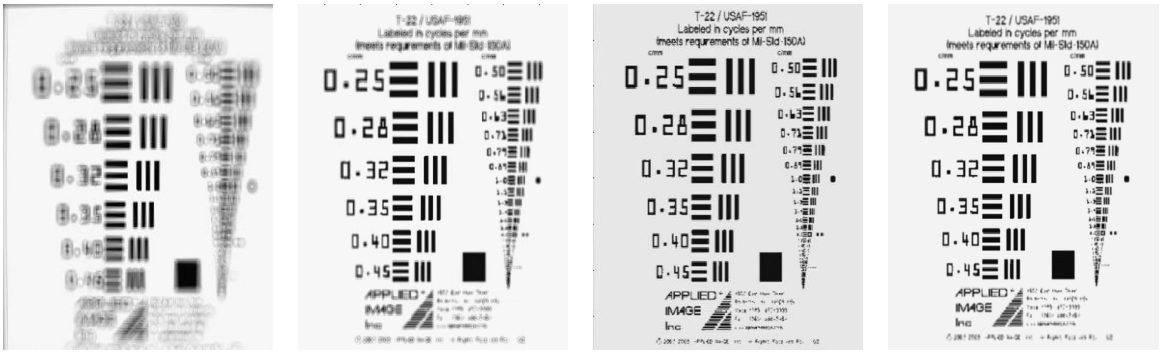

(a) **(b)** **(c)** **(d)**

Figure 12. Comparison of reconstructed images using the current prism design. (a) is the reconstructed image at 400 nm, (b) at 500 nm, (c) at 600 nm, and (d) at 700 nm. The distortion-like effect is the worst at 400 nm. At 500 nm the effect is noticeable primarily in the upper and lower writing. At 600 nm, (c), the image does not appear to be blurry anywhere. At 700 nm (d) the effect is only slightly noticeable in the upper and lower text. All of these observations are in agreement with the results of Figure 11.

In Figure 12 (b-d) the impact of the distortion-like effect is only primarily seen on the outer portions of the image. In order to more clearly see the differences between the images Figure 13 provides the same comparison but only uses only the top of the AF bar chart to do the comparison. This allows for that portion of the image to be magnified and the differences are more easily seen, especially between images Figure 13 (c) and (d).

(a) **(b)** **(c)** **(d)**

Figure 13. Comparison of reconstructed images using the current prism design. (a) is the reconstructed image at 400 nm, (b) at 500 nm, (c) at 600 nm, and (d) at 700 nm. The distortion-like effect is the worst at 400 nm. At 500 nm the image quality is better. The 600 nm, (c), image is the best. At 700 nm (d) the effect is only slightly noticeable. All of these observations are in agreement with the results of Figure 11.

3.1.4 Current and Proposed CTEx Prism Design

The current prism is comprised of two triangular prisms which have been optically bonded together. One triangular prism is made of SF L6 and the other is LaSF N30 seen in Figure 14. The proposed prism design consists of two materials and four pieces of glass. The outer two pieces are made of H-LAK12 and the inner two are made of ZF10. The tilt angle between the inner connected pieces of glass is 25 degrees off vertical, which is significantly less than the current prism as seen in Figure 15. Figure 16 provides a side by side comparison of the dispersion curve of the current prism and the proposed prism design.

There are a couple of key differences between the current prism dispersion curve and proposed prism dispersion curve. The first is that the maximum and minimum deviation angles are symmetric about zero. This means the focal plane array may be smaller and still capture all of the dispersed images or g_i's. The second is the undeviated

wavelength. The original prism wavelength was nearly .55 microns, the new prism is approximately .47 microns. The third major difference is the maximum difference in angles. With the current prism the maximum difference is over 4 degrees, the new prism is only about 1.3 degrees. This is a significant change. To increase the displacement distance of the dispersed images on the focal plane array the focal distance of the third lens was increased from 100 millimeters to 200 millimeters.

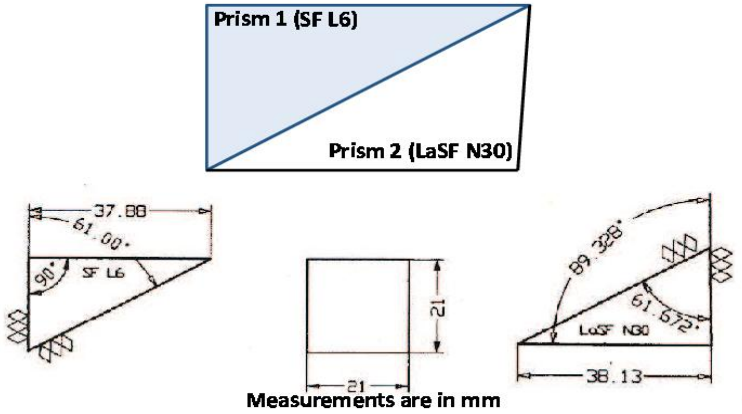

Figure 14. Current CTEx prism design. It is comprised of two triangular prisms. [12]

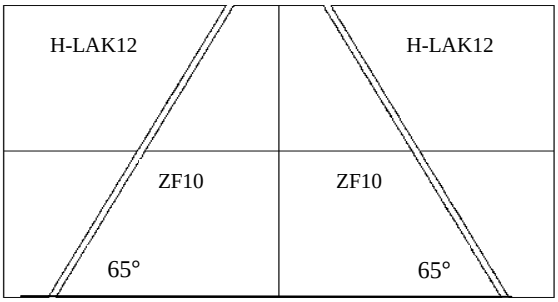

Figure 15. The proposed prism design. It is four individual pieces of glass which are comprised of two materials. The outer two pieces are made of H-LAK12 and the inner two pieces are made of ZF10. All four pieces of glass are dimensionally the same. [6]

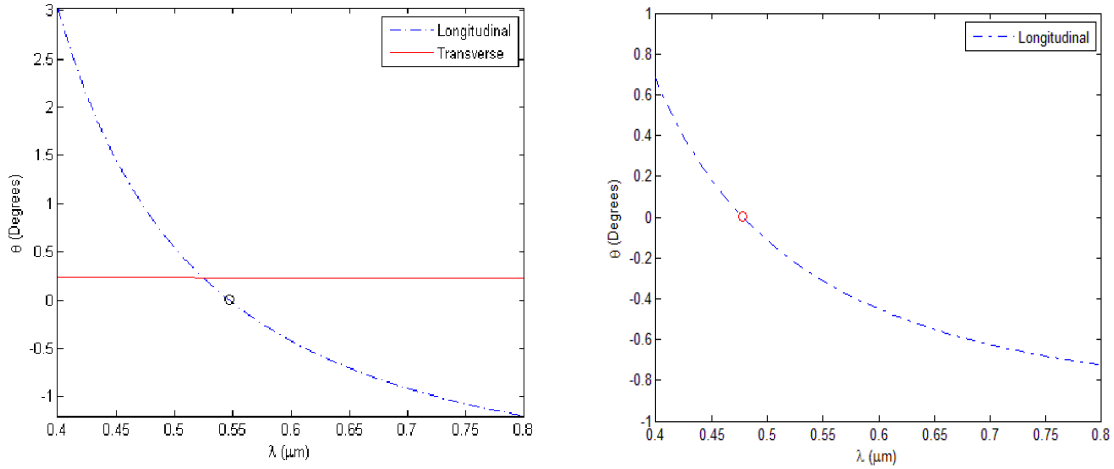

(a) **(b)**

Figure 16. (a) is the dispersion curve for the current prism in the CTEx optical system. There is a transverse error that is nearly constant and is denoted by the red line. The dashed blue line represents the wavelength dependant dispersion. (b) is the dispersion curve for the proposed prism. The dashed blue line is the dispersion curve. The red dot denotes the location of the undeviated wavelength.

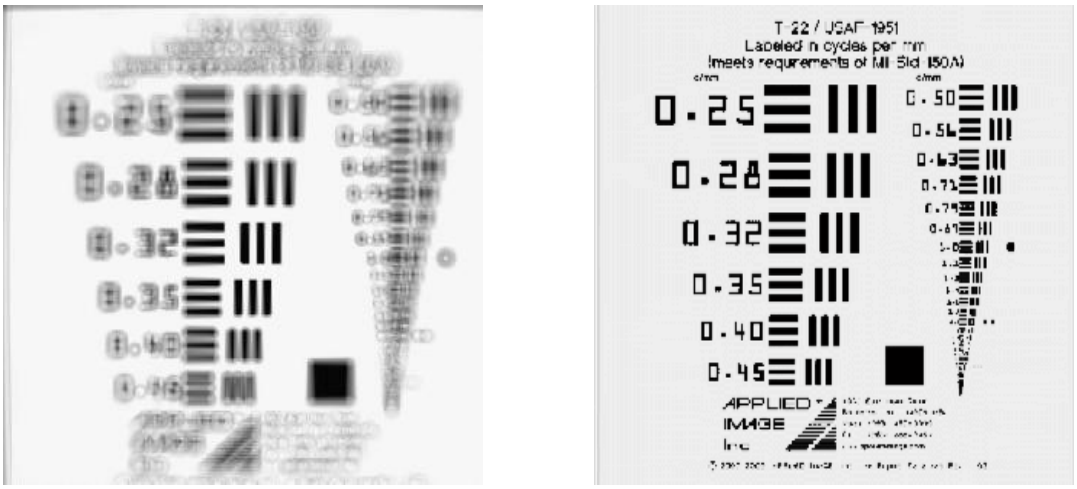

(a) **(b)**

Figure 17. Comparison of reconstructed images using the current and proposed prism design at 400 nm. They are different due to the impact of the prism induced distortion like effect in current prism design. Both images are reconstructed AF Bar charts using simulated projections. (a) Used the current CTEx optical model. Distortion-like effects have minimal impact when the radial distance from the optical axis is small. On the outer edges the effect is more pronounced. (b) is the same reconstructed image using the new optical model with the proposed prism design. Without the effect the reconstructed image is much clearer at all distances from the optical axis.

3.1.5 Zemax Image Simulation

Quoted from the Zemax manual [13] the image simulation is defined as:

> The Image Simulation algorithm consists of the following steps to compute the appearance of the image.
>
> -The source bitmap is oversampled, rotated, and a guard band is applied, if these options are selected.
>
> -A "grid" of Point Spread Functions (PSFs) are computed. The grid spans the field size, and describes the aberrations at selected points in the field of view defined by the bitmap and field size settings. The PSF grid also includes the effects of polarization and relative illumination.
>
> -The PSF grid is interpolated for every pixel in the modified source bitmap. At each pixel, the effective PSF is convolved with the modified source bitmap to determine the aberrated bitmap image.
>
> -The resulting image bitmap is then scaled and stretched to account for the detected image pixel size, geometric distortion, and lateral color aberrations.

In order for Zemax to understand how to simulate the image properly a few basic image parameters must be defined. Three of the most important are the field position, wavelength, and field height. The simulation sets the field position to zero which centers the input image on the optical axis. The wavelength is defined in the initial target hypercube. The field height was defined in terms of the paraxial image height field.

The major benefit of defining the field height in this manner is that, provided that the target image is a square image, it enables a pixel to pixel comparison to be used in the analysis stage. This significantly strengthens the interpretation of the analysis as differences between the target images, $f(x, y, \lambda_z)$, and the reconstructed image, $f'(x, y, \lambda_z)$, are the result of reconstruction algorithms not resampling or magnification.

There are a number of simulation parameters that must be set in the Zemax simulation tool. These settings, for the CTEx simulation, made very little observable difference in the simulated images when no optical aberrations were present. When the Zernike mask was used to introduce optical aberrations, the simulation settings made a difference in both the output image and computation time.

Table 2 shows the settings used for all simulations. Two driving forces were used in their selection. The first was the image quality. In many instances increasing a simulation setting made little or no observable change to the simulated images. If there was no significant improvement in the image quality the setting was not raised. The second factor was time. A typical simulation produced between 3,000 and 18,000 images for a single target. In order to be process all of the target sets there had to be a reasonable completion time.

Table 2: Zemax Image Simulation Settings Used In Experiment

Setting Name	Settings Used
Oversampling	None
Aberration Type	Geometric
Pupil Sampling	32x32
Image Sampling	32x32
PSF-X-Points	1
PSF-Y-Points	1
Reference	Vertex

3.2 Reconstruction

Once the simulated images have been created the reconstruction tool takes those files and uses the reconstruction algorithms to reconstruct the hypercube. The reconstruction tool was written in MATLAB and has a GUI interface in which the basic reconstruction parameters are set. This tool can process both the simulated images and

the experimental images from the CTEx instrument that has been processed in the conversion tool. A user comment section is also available. See Figure 18.

Similar to the simulation tool there are two run modes, single and multiple. Single mode will reconstruct the specific image file selected. When multiple mode is selected it will reconstruct all of the image files in the specified directory. Parallel processing has been incorporated, if available on the machine being used, to help decrease the processing time.

The reconstruction algorithms currently programmed are the Back Project, Filtered Back Project, and the newly developed Shift and Place. The remaining four slots have been built into the interface and underlying architecture of the program for future expansion. Since each simulation can potentially create seven reconstruction files, the simulation tool provides basic file management. It does this by creating a directory for each target file being reconstructed and storing the associated files in the directory. In the case of multiple simulations of a single target file in which aberrations are incrementally varied it will place the set of simulations of the same target file into the same directory.

The reconstructed image file format is a cell structure array that functions like a database table in which each row functions like a record. The first column contains the reconstructed wavelength in nanometers. The second column contains the reconstructed image. A MATLAB data structure is used to maintain all of the parameters used in the reconstruction and is saved as a variable with the reconstructed image file so the parameters can be referenced at a future date.

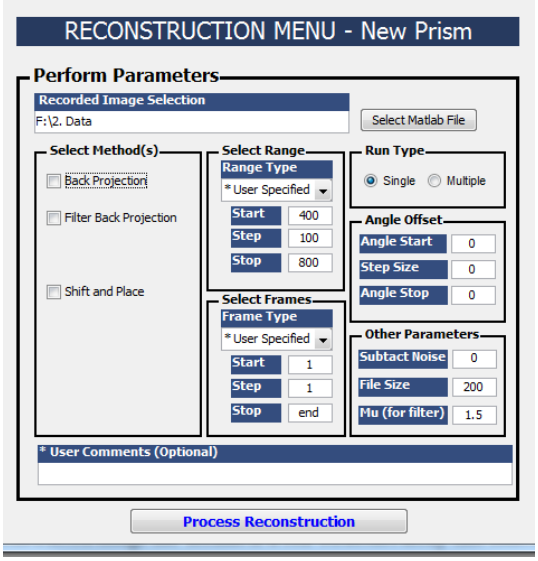

Figure 18. The reconstruction tool. It allows the reconstruction parameters to be quickly set.

3.2.1 Primary Reconstruction Algorithm

Back Projection is the primary reconstruction algorithm used in the analysis. It is identical to the Shift and Add technique in principle. Shift and Add takes each projection, $g(\bar{x},\phi)$, and shifts them a set distance to create a set of shifted projections, $g(\bar{x},\phi)_{shifted}$, and sums them to create a $f'(x,y,\lambda_z)$. The distance is associated with a wavelength based on the properties of optical system and is along the direction of the prism angle. When the shift distance corresponds to one of the wavelength specific images in the target hypercube, $f(x,y,\lambda_z)$, the shifted projected images, $g(\bar{x},\phi)_{shifted}$, will align in such a way that when summed an image of $f(x,y,\lambda_z)$ is produced. Back Projection works the same way but instead of moving the image directly, it converts the image into frequency space using Fourier Transforms. The images are multiplied by an exponential phase factor and summed in frequency space. An inverse Fourier transform is used to produce the new image in the space domain.

3.3 Analysis

The last stage of the simulation is the analysis portion in which the original target hypercube and the reconstructed hypercube are compared. The analysis tool was written in MATLAB and has a GUI interface. It is much more interactive than the previous interfaces and was built primarily to make it easier to quickly view and compare the reconstructed images to the initial target images. It enables up to three data cubes to be loaded simultaneously for side by side comparisons to be made visually. When displaying the images it does so using the scaled intensities image. The program is flexible to allow all of the images to be synced together or independently controlled as seen in Figure 19.

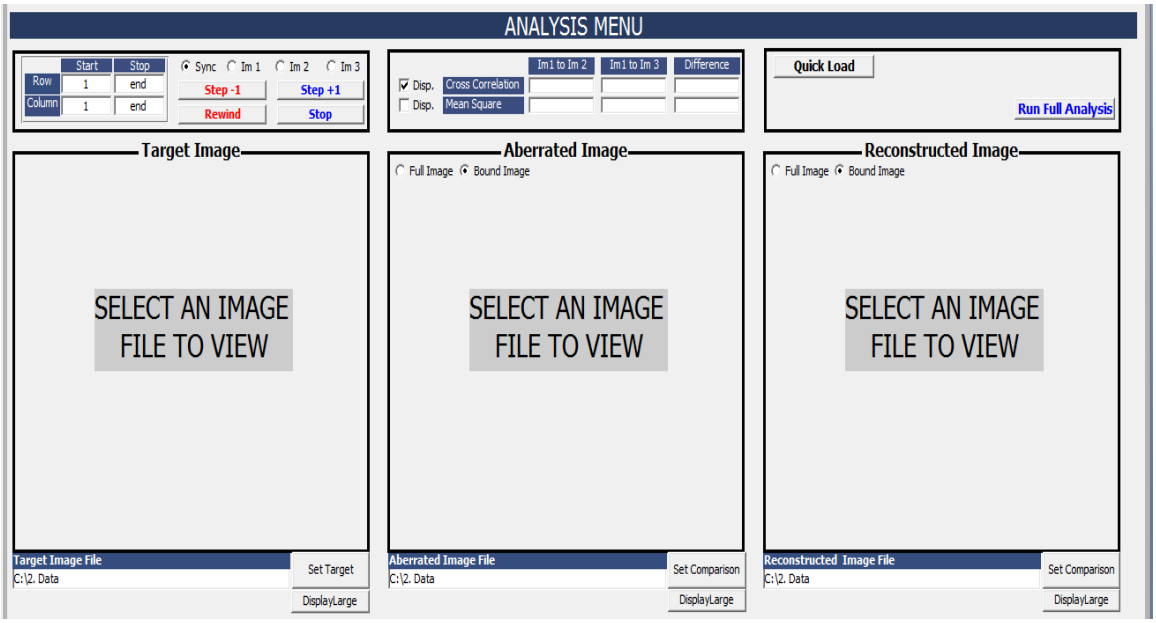

Figure 19. The analysis tool. It enables a side by side comparison of multiple hypercube images. It will also display the normalized cross correlation and mean square error calculations if selected. The controls enable each image parameter to be set individually or they can be synchronized together. This tool can also perform the cross correlation function on each image in the hypercube and save the results in a MATLAB file.

The analysis tool also provides a quantitative analysis on the target hypercube and the reconstructed hypercube in two ways. The first is the normalized cross correlation between the images and the second is the total root mean square error. These are displayed on the tool itself for the current wavelength being displayed. A full analysis on all of the images is also available and will produce a MATLAB file containing all of the analysis information.

3.3.1 Reconstructed Image Analysis Method

Cross correlation provides the means of comparing two images to determine how similar they are two each other [5]. The cross correlation process involves taking the Fourier Transform of each image. Since the images in the simulation are digital it is appropriate to use the discrete Fourier Transform. After each image has been transferred into frequency space the two functions are multiplied together and then the inverse Fourier Transform is applied. The greater the cross correlation value is the greater the similarity between images.

In order to perform the cross correlation each image must be expressed as a function. Since most digital images are represented as a matrix of numbers the image can be represented as $a_{1,2}(x,y)$, in which x and y are spatial variables. Digital images are discrete so the convolutions uses the discrete Fourier transform function, by

$$\mathcal{A}_{1,2}\{\xi_1,\xi_2\} = \sum_{y=0}^{N-1}\sum_{x=0}^{M-1} a_{1,2}(x,y)\exp(-2\pi i(\frac{\xi_1 x}{M}+\frac{\xi_2 y}{N})). \quad (6)$$

M and N are the number of pixels on the focal plane array. ξ_1 and ξ_2 are the spatial frequency variables. The transformed images are multiplied together and an inverse Fourier Transform is applied by

$$b(x,y) = \frac{1}{MN}\sum_{y=0}^{N-1}\sum_{x=0}^{M-1}\mathcal{A}_1\{\xi_1,\xi_2\}\mathcal{A}_2\{\xi_1,\xi_2\}\exp(2\pi i(\frac{\xi_1 x}{M}+\frac{\xi_2 y}{N}))\,. \tag{7}$$

In many respects the cross correlation is like taking the dot product of two vectors in which,

$$v_1 \bullet v_2 = |v_1||v_2|\cos(\theta)\,. \tag{8}$$

The value of the dot product depends on the magnitude of each vector and the cosine of the angle between the vectors. A straight forward way to determine how similar the two vectors are in direction is the take the dot product of the two normalized vectors. Then the dot product would only contain information on the angle between the two vectors as $|v_1|$ and $|v_2|$ would equal one. In that case the absolute maximum value of cosine would be one.

If we consider images to be analogues to vectors then the overall magnitude of the image would correspond to the magnitude of the vector and the image pattern would correspond to the direction. Just like comparing how similar two vectors are in direction if the two images were first normalized the cross correlation would provide information only on how similar the two images were in terms of their pattern without regard to the actual intensities. Just like using normalized vectors the normalized cross correlation would have an absolute maximum value of one.

For instance if two images were identical and the cross correlation was applied the maximum cross correlation value would represent how similar the two images are to each other. Since the images were identical that number would represent a perfect match. Now if we were to take the same two images as before and apply a perfect neutral density filter that reduces the image intensity by half to the second image and then do the cross

correlation the maximum value would change. In one sense the first comparison without the neutral density filter is a better match because the intensities match each other. From an image pattern standpoint, however, both cases are just as equally valid. They both should be "perfect" matches because the patterns in all three images are identical. The strength of using the normalized cross correlation is that it essentially looks at the pattern within the two images being compared and ignores the specific intensity values.

MATLAB offers a normalized two dimensional cross correlation function that is ideal for analyzing the results of the original target hypercube, $f(x, y, \lambda)$, and the reconstructed hypercube, $f'(x, y, \lambda)$, in this way. Two images that match perfectly will have a maximum normalized cross correlation of one. Images that do not match at all will have a normalized correlation of zero. Comparing images this way provides a clear understanding of how well the reconstruction performed.

MATLAB's two dimensional normalized cross correlation function provides multiple values depending on how the functions or images line up with each other. For the purposes of the analysis the maximum normalized correlation value will be utilized when comparing two images to each other. The assumption is the maximum value of the cross correlation function will occur when the images are in line with each other.

The normalized two dimensional cross correlation function provides excellent means of comparing 2D images but hypercubes are 3D images. In order to evaluate the 3D image we can treat it as a set of 2D images. In order to perform the analysis the initial target 2D images, $f(x, y, \lambda_z)$, will be matched to the reconstructed 2D image, $f'(x, y, \lambda_z)$, with the same wavelength to form an image pair. Each image pair will be

processed with the normalized cross correlation function in which the maximum value is selected and used. The analysis will use the mean and standard deviation of the resulting normalized cross correlations over all wavelengths.

For example, if an initial hypercube contains five 2D images, $f(x, y, \lambda_z)$, then the analysis will match each 2D image in the initial target hypercube to the corresponding 2D image in the reconstructed hypercube, $f'(x, y, \lambda_z)$, that has the same wavelength. In this case there will be five image pairs. Each image pair will each be evaluated using the normalized cross correlation value. The mean of the five cross correlation values and the standard deviation values will be used as the basis of how well the reconstructed image quality was.

Monochromatic hypercubes will be treated slightly differently since they only have a single wavelength specific image, $f(x, y, \lambda_z)$, and a single cross correlation value does not produce a useful standard deviation. In those cases multiple monochromatic hypercubes, $f(x, y, \lambda)$, will be constructed using the same image but each having a unique wavelength that range from 400 to 800 nanometers. The results of the monochromatic hypercubes of similar image types will then be averaged and the standard deviation provided.

3.4 Video Conversion Tool

A video conversion tool was also built to enable data taken with the CTEx instrument to be processed with the reconstruction tool and displayed with the image analysis tool. It does this by taking the actual CTEx instrument recorded image file and

associated angle file and converting them into a MATLAB format identical to the simulated image MATLAB file. This enables the recorded images from CTEx to be processed and reviewed with the reconstruction tool and viewed with the analysis tool.

The conversion tool was written in MATLAB and has a GUI interface which takes the selected CTEx recorded images and the associated angle file and converts them into a MATLAB recorded image file. The recorded image file format is an cell array structure that functions like a database table. A MATLAB data structure was established to save the file names and paths used in the conversion as well as any user comments that may have been entered. This data structure is saved as a variable with the MATLAB file. Batch processing is not available with this tool.

3.5 New Reconstruction Algorithm

This section will first describe how Back Projection works in much greater detail using three examples. The first two examples use a monochromatic hypercube, $f(x, y, \lambda)$, of a point source and the letter 'A'. These targets will be simulated and then reconstructed at both the correct wavelength and off-wavelengths to illustrate how the Back Projection algorithm is placing the information from the projections, $g(\bar{x}, \phi)$, into the reconstructed hypercube or $f'(x, y, \lambda)$.

The third example uses an initial hypercube, $f(x, y, \lambda)$, with five wavelength specific image or $f(x, y, \lambda_z)$ Each wavelength specific image $f(x, y, \lambda_z)$ is spectrally spaced 100 nm apart from each other. This example is used to explain the fundamental problem of the Back Projection method. Once the problem has been fully developed the

proposed new reconstruction algorithm will be explained. The following section relies on a large number of figures to help illustrate the points described.

3.5.1 Back Projection Reconstruction Examples and Fundamental Problem

The first Back Projection example involves the simplest object, a monochromatic point-like source. The Back Projection algorithm makes the assertion that the dispersed light from the point source in the hypercube must exist somewhere on the line segment that is parallel to the direction of the prism and goes through the point the light was recorded. At this point there no information as to where on the line the point source originated from in the target hypercube. For example, it could be the undeviated wavelength in which case the dispersion distance was zero and the recorded projection is in fact where the point sources exists spatially. It could also be at one of the ends of the visible spectrum in which case the light was dispersed a great distance, or anywhere in between these two extremes. With a single image it is not possible to make a determination as to where on the line the point belongs. This is very similar to the x-ray image example trying to determine where the patient's ribs, lungs, and heart exist in the third dimension of space. A single recorded projection does not contain that information.

In the case of a monochromatic point source, multiple projections are recorded and processed through the reconstruction algorithm. Back Projection takes the projections, $g(\bar{x},\phi)$, and shifts them individually to create shifted projections, $g(\bar{x},\phi)_{shifted}$, and then combines the shifted images together to make a reconstructed image or $f'(x,y,\lambda_z)$. When the reconstructed wavelength is incorrect the reconstructed image, $f'(x,y,\lambda_z)$, appears to form a circle. When the correct wavelength is used the

reconstructed image, $f'(x,y,\lambda_z)$, appears to be the original image, in this case a point-like object as seen in Figure 20.

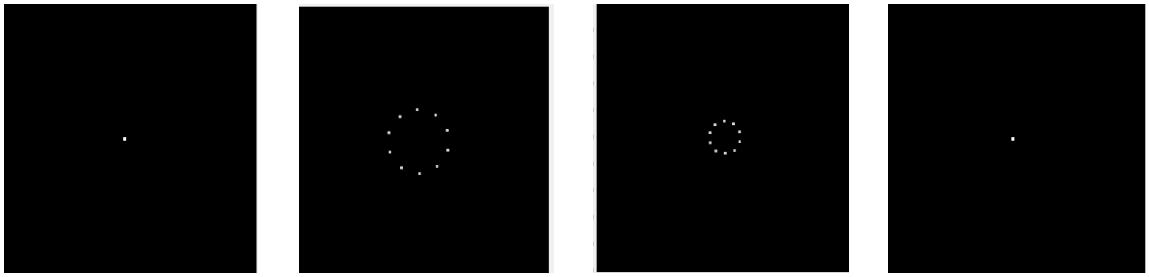

(a) **(b)** **(c)** **(d)**

Figure 20. A monochromatic hypercube using a point source and three reconstructed images at three wavelengths. The initial target is a point source shown in (a) with a wavelength of 600 nm. There are 10 projections used in the reconstruction. (b) and (c) are reconstruction at the incorrect wavelength of 500 nm and 700 nm respectively. (d) is the reconstructed image at the correct wavelength of 600 nm. In (d) all of the projections converge producing a point.

The second example is only slightly more complicated but demonstrates the same basic situation occurs for more complicated objects. In this case the target is a monochromatic hypercube, $f(x,y,\lambda)$, consisting of a small letter 'A' as seen in Figure 21. When the wrong wavelength is used the reconstructed image, $f'(x,y,\lambda_z)$, looks like multiple copies of the letter 'A' are forming a circle around a center point. Each letter 'A' in reconstructed image, $f'(x,y,\lambda_z)$, is from a projection, $g(\bar{x},\phi)$, that was not shifted the correct distance to have those images converge. Once the correct wavelength is selected all of the shifted projection images, $g(\bar{x},\phi)_{shifted}$, converge and the reconstructed image, $f'(x,y,\lambda_z)$, matches the original hypercube image or $f(x,y,\lambda_z)$. The on-wavelength reconstructed image, $f'(x,y,\lambda_z)$, is the combined intensity contributions of the

individual projections or $g(\bar{x},\phi)$. For example, in Figure 19 the intensity of the letter 'A' in panel d is six times the intensity of the individual letters in panel b and c.

In part the reconstruction algorithm is successful. It accurately shows, in Figure 21(d), the correct spatial and spectral information that was present in the initial hypercube wavelength specific image ($f(x,y,\lambda_z)$) shown in Figure 21(a). Images in Figure 21(b) and Figure 21(c) are the reconstructed images, $f'(x,y,\lambda_z)$, taken at off-wavelength. The expectation is that for off-wavelength reconstructions the image should be blank since the initial target hypercube, $f(x,y,\lambda)$, was monochromatic but as seen in Figure 21(b) and Figure 21(c) this is not the case.

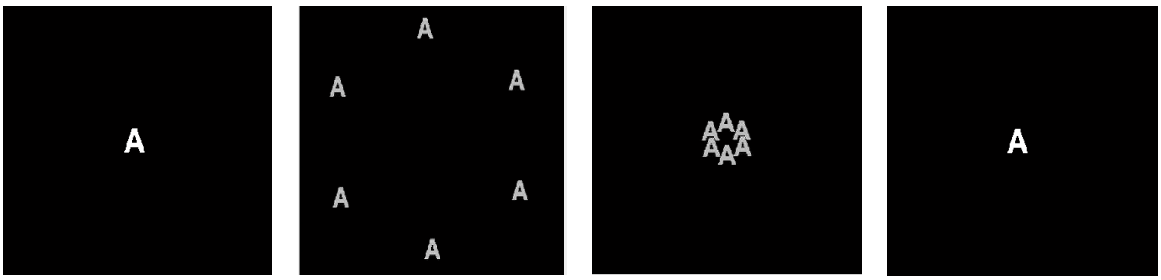

Figure 21. A monochromatic hypercube using a small letter reconstructed at three wavelengths. In (a) is the initial target image of a letter 'A' at a wavelength of 600 nm. Six projections were used in the reconstruction in (b) and (c). (b) and (c) are reconstructed at the wrong wavelength of 400 nm and 700 nm respectively. (d) was reconstructed at the correct wavelength of 600 nm as seen by all of the projections converging.

The next example demonstrates the full extent of the problem. This target hypercube, $f(x,y,\lambda)$, contains five images, $f(x,y,\lambda_z)$, at five different wavelengths in which six projections, $g(\bar{x},\phi)$, were used in the reconstruction. The images, $f(x,y,\lambda_z)$, in the target hypercube are the first five letters of the alphabet. For display purposes only

the first three images in the target hypercube, $f(x, y, \lambda)$, and reconstructed hypercube, $f'(x, y, \lambda)$, are shown in Figure 22.

Figure 22 (a - c) contains the images in the initial target hypercube, $f(x, y, \lambda_z)$. Figure 22 (d - f) are the associated reconstructed images, $f'(x, y, \lambda_z)$. Ideally each image pair would match. What is observed is that multiple copies of the off-wavelength images, $f(x, y, \lambda_z)$, are present in the reconstructed images, $f'(x, y, \lambda_z)$, as artifacts. These artifacts have the potential of greatly limiting the reconstructed image quality.

The Back Projection algorithm does try to limit the impact of the artifacts introduced in the reconstruction. The way it does this is by using as many projections as possible in the reconstruction. The result is that the image at the correct wavelength, $f(x, y, \lambda_z)$, will increase in intensity because the on-wavelength images in the shifted projections, $g(\bar{x}, \phi)_{shifted}$, will all line up with each other. The off-wavelength images, $f(x, y, \lambda_z)$, will not line up in the shifted projections, $g(\bar{x}, \phi)_{shifted}$, and as a result their contribution will be diminished.

To demonstrate how using addition projections helps the reconstructed image quality the previous example will be repeated but this time instead of using only six projections the reconstruction will use 180 projections or $g(\bar{x}, \phi)$. The result is that while the artifacts of off-wavelength images are still present in the correct wavelength images, $f(x, y, \lambda_z)$, are clearly identifiable while the off wavelength images have been smeared out and their impact minimized as seen in Figure 23.

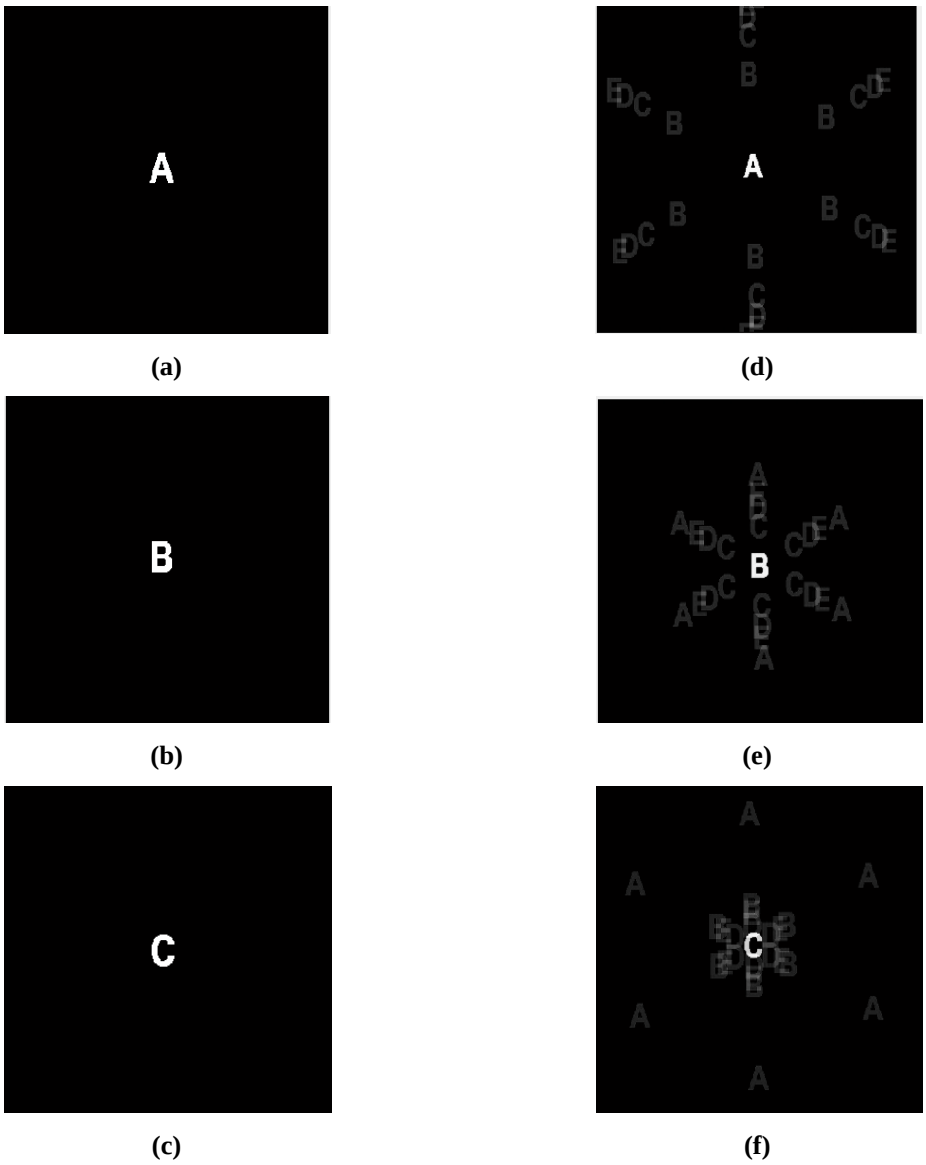

Figure 22. The initial target hypercube that contains five images of the first five letters of the alphabet each at different wavelengths. For display purposes only three images are shown. The three images in that hypercube are on the left as (a) - (c) with the wavelengths of 400 nm, 500 nm and 600 nm respectively. The corresponding reconstructed images are to their right in (d) - (f) using Back Projection of 400 nm, 500 nm, and 600 nm respectively.

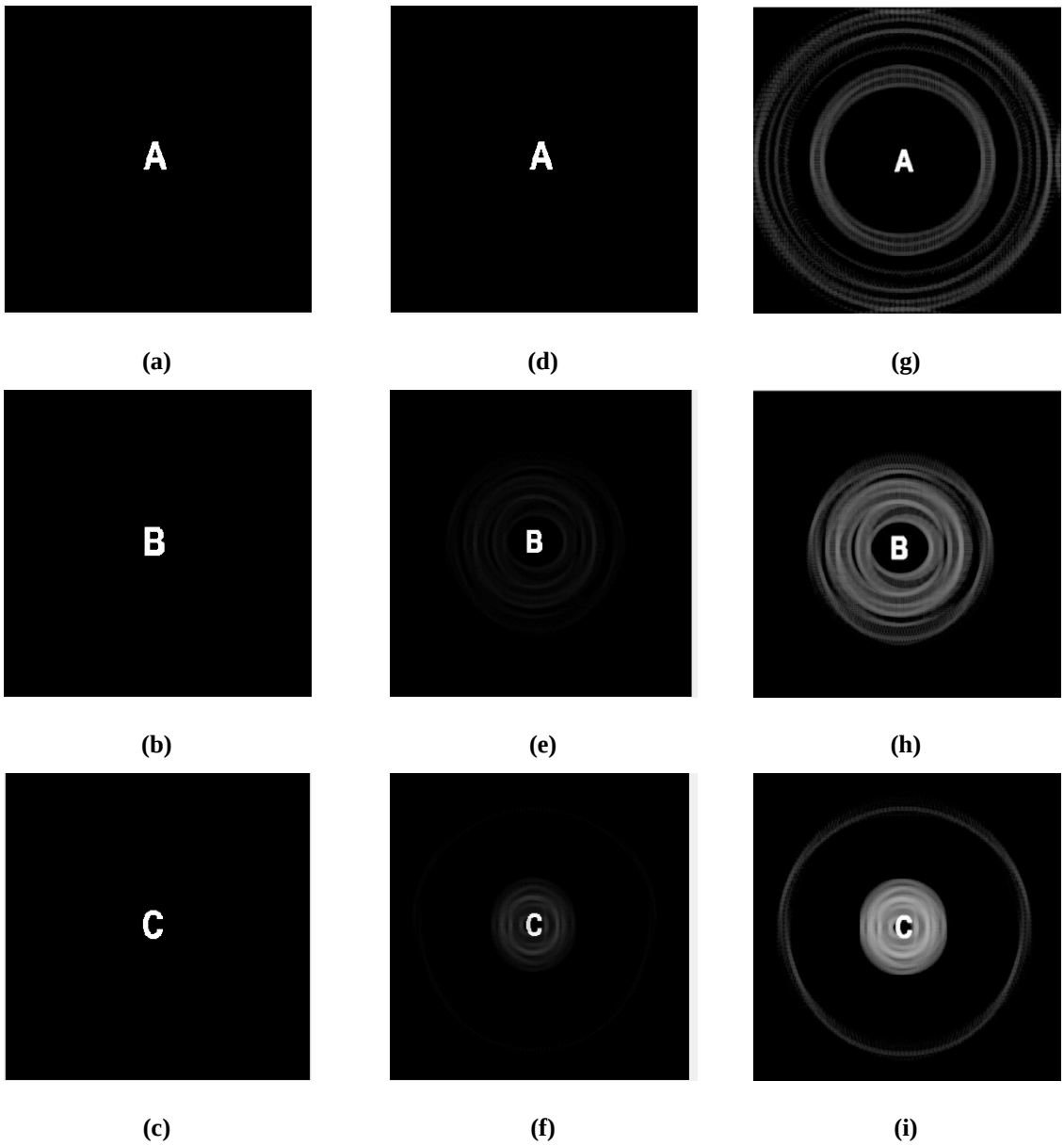

Figure 23. A hypercube that contains five images of the first five letters of the alphabet each at different wavelengths. Only three images are shown for display purposes. The initial target images are on the left, (a) - (c) with wavelengths of 400 nm, 500 nm, and 600 nm respectively. The reconstruction algorithm used 180 projections. The result is that the artifacts are still present but the image from the correct reconstructed wavelength is much easier to see and the off-wavelength images are essentially blurred out so their effect is minimized. The reconstructed images in (d) - (e) have been plotted a second time in (g) - (i) using the log of the intensity values to better highlight the off-wavelength artifacts.

The primary problem with Back Projection is that off-wavelength images, $f(x, y, \lambda_{off-wavelength})$, are present in the on-wavelength reconstructed images, $f'(x, y, \lambda_{on-wavelength})$. The impact of the artifacts can be reduced by using additional projections, $g(\bar{x}, \phi)$, but never fully eliminated. Instead of trying to diminish image artifacts using additional projections an alternate solution may be to find a way to remove the off-wavelength artifacts from the reconstructed image, $f'(x, y, \lambda_z)$, all together.

3.5.2 Proposed Solution to Back Projection Problem

The proposed solution is to determine what information in the shifted projection images, $g(\bar{x}, \phi)_{shifted}$, belong to the on-wavelength reconstructed image, $f'(x, y, \lambda_z)$, and what information in the shifted projection is an off-wavelength artifact. If during the reconstruction process there was a way to identify the information that belongs in the reconstructed image ($f'(x, y, \lambda_z)$), the rest of the information could be discarded. Additionally, the information that was identified to belong to a specific image in the hypercube, $f'(x, y, \lambda_z)$, could then be subtracted out of the remaining reconstructed images, $f'(x, y, \lambda_z)$, where it appears as artifacts.

The Shift and Place reconstruction algorithm attempts to do this in five steps. The first step starts by shifting each recorded image in the same fashion as the Back Projection method. This first step produces a set of shifted projections or $g(\bar{x}, \phi)_{shifted}$ for a specific wavelength. The second step determines which information belongs at the wavelength specific reconstructed image, $f'(x, y, \lambda_z)$, and defines it as placed information. The third step takes the placed information from step 2 and subtracts it out

of the set of projection images or $g(\bar{x},\phi)$. Steps two and three are repeated for all of the reconstructed wavelengths. Once the process is complete for all of the reconstructed wavelengths the resultant projections, $g(\bar{x},\phi)$, contain only the unplaced information. The fourth step takes all of the information that could not be placed and creates a second hypercube, $f'(x,y,\lambda)$, using the Back Projecting algorithm. Finally, in the fifth step, the hypercube ($f'(x,y,\lambda)_{placed}$) of placed information and the hypercube ($f'(x,y,\lambda)_{notPlaced}$) of not placed information are summed to create the final hypercube, $f'(x,y,\lambda)$. This prevents information from being lost or discarded. Figure 24 depicts a set of shifted images, $g(\bar{x},\phi)_{shifted}$.

The primary difference in the first step between Back Project and Shift and Place is that the Back Projection sums all of the shifted images, $g(\bar{x},\phi)_{shifted}$, together to create the reconstructed image, $f'(x,y,\lambda_z)$. Shift and Place does a comparison of the shifted images or $g(\bar{x},\phi)_{shifted}$ and makes a determination as what information should be placed and what information should not be to minimize the impact of artifacts.

(a) **(b)** **(c)** **(d)** **(e)**

Figure 24. Five shifted projections of a hypercube containing five wavelength specific images. (a) - (e) represent the shifted images produced when the reconstruction algorithm was reconstructing to the wavelength of the letter 'C'. It appears that the letter 'C' is stationary and the other letters are being rotated around it.

In order to determine if the information should be placed in the reconstructed image ($f'(x, y, \lambda_z)$), we compare each of the shifted images ($g(\bar{x}, \phi_1)_{shifted}$) for a given reconstructed wavelength. The comparison starts off by creating a temporary image and sets it equal to the first image in the set of shifted images or $g(\bar{x}, \phi_2)_{shifted}$. Any image in the set could be used to initiate the temporary image but for convenience the first image in the set of shifted images is used. This new temporary image is then compared to the second image in the set of shifted images or $g(\bar{x}, \phi)_{shifted}$. These two images are compared pixel by pixel to identify which image has the lower index value. A new temporary image is then created in which the individual pixels are set to the value of the lower pixel value between the two images. An example of a four pixel image is shown in Figure 25. This process is repeated until all of the shifted images, $g(\bar{x}, \phi)_{shifted}$, have been evaluated. At the end of all the comparisons the values of the last temporary image is identified as the placed information in the placed reconstructed hypercube, $f'(x, y, \lambda)$.

1	30
50	15

(a)

13	7
8	67

(b)

1	7
8	15

(c)

Figure 25. Three 2x2 matrixes demonstrating the placement technique used in Shift and Place. (a) represents the first image. (b) represents the second image. The comparison function creates image (c) using the lowest value between the image (a) and image (b) per pixel. Some information in image (c) came from image (a) and some from image (b). This process repeats for each of the shifted images.

The reason this method has the potential of making a correct selection is based on the fact that each recorded projection, $g(\bar{x}, \phi)$, contains all of the wavelength specific

images, $f(x, y, \lambda_z)$, in the initial target hypercube or $f(x, y, \lambda)$. When the reconstruction algorithm uses the wavelength that exists in the target hypercube, the resulting shifted images, $g(\bar{x}, \phi)_{shifted}$, contain one image, $f(x, y, \lambda_z)$, which appears to be stationary, as demonstrated in Figure 24. All of the off-wavelength images, $f(x, y, \lambda_z)$, in the shifted projections or $g(\bar{x}, \phi)_{shifted}$, are changing position. Since the selection process uses the minimum pixel values between the shifted images, $g(\bar{x}, \phi)_{shifted}$, the stationary image corresponding to $f(x, y, \lambda_z)$, should never drop below the corresponding pixel values in $f(x, y, \lambda_z)$.

The placed information is then used in a reverse Back Projection or a Forward Projection to subtract it from the projections or $g(\bar{x}, \phi)$. It takes the placed information and shifts it the opposite direction of the Back Projection algorithm but the same distance for $g(\bar{x}, \phi)$. Essentially this process is repeating what the prism did initially to the recorded images, namely shifting it a set distance based on the wavelength. These images are then subtracted out of the recorded images. Using the example from Figure 26 this would be subtracting out the image of the letter 'C' from the projections or $g(\bar{x}, \phi)$. By doing this when the next reconstructed wavelength is processed the projections will no longer have that image ($f(x, y, \lambda_z)$) where it would create off-wavelength artifacts.

Using now the new set of projections, $g(\bar{x}, \phi)_{new}$, the reconstruction algorithm repeats the process for each wavelength being reconstructed to create reconstructed

hypercube, $f'(x,y,\lambda)_{placed}$, of placed information,. Once all of the wavelengths have been reconstructed, the remaining information in the recorded image are used in the Back Projection Algorithm to produce a second hypercube $f'(x,y,\lambda)_{notPlaced}$. These two individual hypercubes, one of placed information and the other of non-placed information, are then added together to create the final hypercube.

Provided that information was not placed incorrectly, in principle, this algorithm should always perform better than the Back Projection. The reasoning is that if none of the information can be placed using the Shift and Place technique the default is Back Projection. If all of the information is successful placed then the reconstructed hypercube is a perfect representation of the target hypercube. If only some of the information is placed then it should be better than the Back Projection alone because at least some of the information has been removed from the projected images. In all three scenarios the worst it should do is be equal to the results of the Back Projection. Figure 26, Figure 27, and Figure 28 demonstrates the difference reconstruction results between Back Projection and the Shift and Place. The artifacts are extremely dim in Figure 26 so Figure 27 does the same comparison a second time but displays the log of the intensities to better display the artifacts. In Figure 28 provides a larger side by side comparison of a Back Projection to Shift and Place for a single reconstructed image.

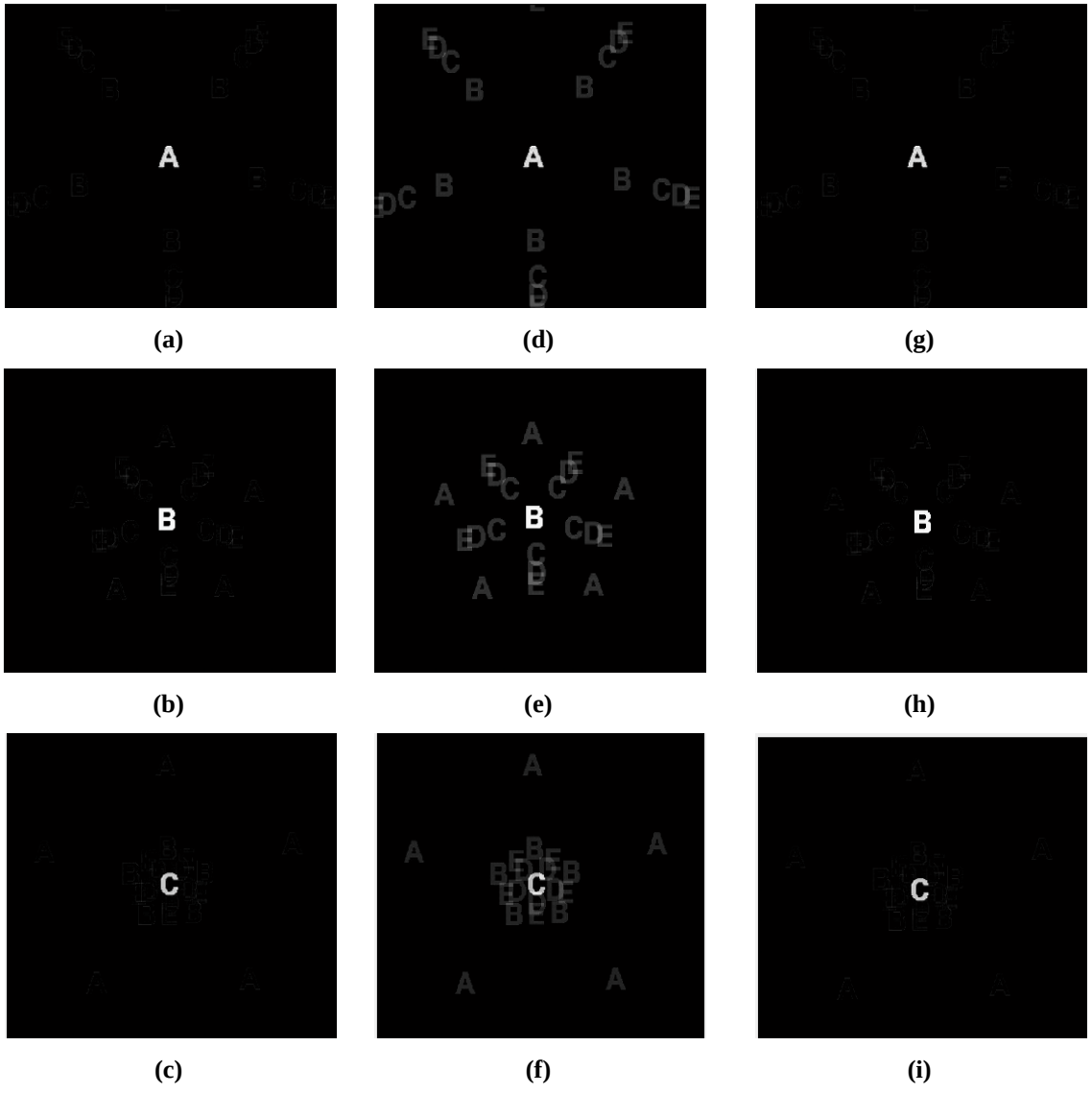

Figure 26. Comparison on the reconstruction results of Back Projection and Shift and Place. Images (a) - (c) are the images in the target hypercube. (d) - (f) are the respective reconstructed images produced by the Back Projection method using five prism angles. (g) - (i) are the reconstructed images using the Shift and Place algorithm. All of the target hypercube projections are present in the Back Project. The Shift and Place provided a much better reconstructed image because nearly all of the off reconstructed wavelength projections have been removed. An outline of the letters exists. The outlined portions were not successfully placed information so it was left in the recorded images and was used in the Back Projection.

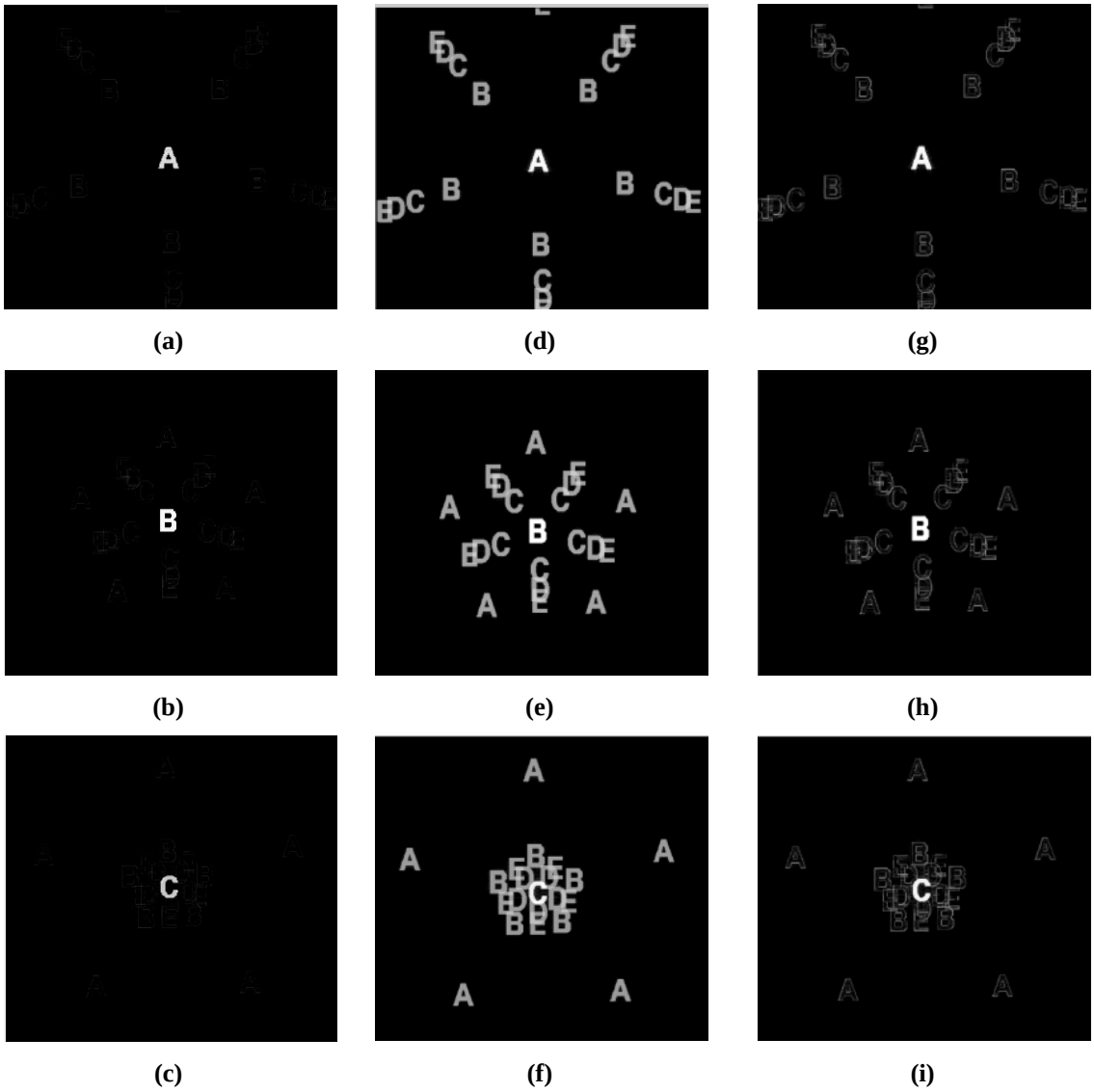

(a) **(d)** **(g)**

(b) **(e)** **(h)**

(c) **(f)** **(i)**

Figure 27. Comparison on the reconstruction results of Back Projection and Shift and Place as in Figure 26, but displayed on a log scale. Images (a) - (c) are the images in the target hypercube. (d) - (f) are the respective reconstructed images produced by the Back Projection method using five prism angles. (g) - (i) are the reconstructed images using the Shift and Place algorithm. All of the intensities shown are the log of the reconstructed intensities to better show the artifacts. The Shift and Place provided a much better reconstructed image because a majority of the off-wavelength artifacts have been removed. An outline of the off-wavelength letters still exists. The outlined portions were not successfully placed information so it was left in the recorded images and put in the not placed category. All of the not placed information is back projected and added to the placed datacube.

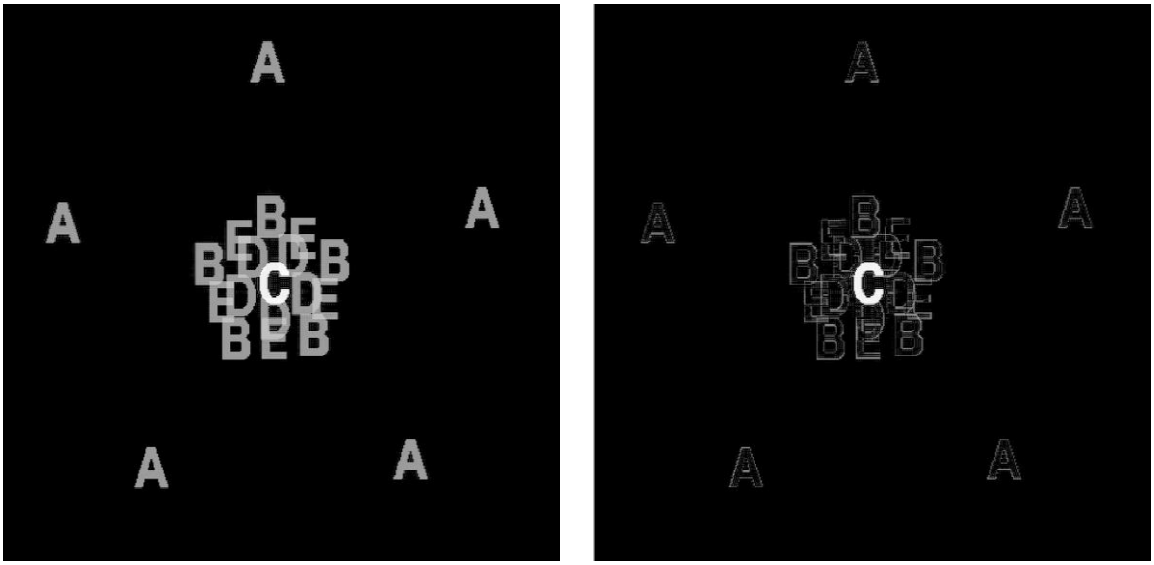

(a) **(b)**

Figure 28. A Side by side comparison of the reconstructed images using Back Projection in (a) and Shift and Place in (b). The initial hypercube consists of the first five capital letters. The reconstructed wavelength is on the letter 'C'. Shift and Place was able to identify and remove most of the off-wavelength artifacts. If using the full field of view the normalized cross correlation of (a) is .712 and (b) is .966. The removal of off-wavelength artifacts in the reconstructed image greatly improves the image quality. In both images the letter 'C' intensity is approximately log(100) or 4.6.

IV. Analysis and Results

This chapter starts by defining the basic target sets used in the simulation. These target sets will be used to evaluate three areas of investigation; how prism angle selection and range impact the reconstructed image quality, how well the new Shift and Place reconstruction algorithm performs compared to the traditional Back Projection method, and the impact of optical aberrations on the reconstructed image quality. Each area of investigation will have a section dedicated to it.

In all of the evaluations the normalized two dimensional cross correlation will be used to evaluate how closely the reconstructed image matches the initial target image. If the images are identical the normalized cross correlation will have a value of one. If the two images do not match at all it will have a value of zero. The primary benefit of using the normalized cross correlation is that reconstructed images of different sizes can be easily compared. Since the images are normalized only the relative intensities are used in the evaluation. This technique is not useful if an evaluation of the absolute intensities is required.

4.1 Initial Target Sets

The performance capability a chromotomographic instrument as a hyperspectral imager depends heavily on the initial target being used in the evaluation. In order to identify any general trends of the system's performance a wide range of initial targets, $f(x, y, \lambda)$, were used. Since CTEx is a hyperspectral imager the initial targets varied in spatial and spectral complexity.

Varying the target hypercube spatially was accomplished using five basic images or $f(x, y)$. These images are of a point-like source, small capital letters, a backlit Air Force bar chart, a front lit Air Force bar chart, and a 400 by 400 grid of random intensities. The point-like source was represented as a small 5 by 5 square of pixels. In addition each of these basic images, except the 400 by 400 grid of random intensities, are used with constant intensities and random intensities, see Figure 29.

Spectrally the targets were varied using different number and spectral spacing of the images depicted Figure 29. The spectral configurations includes monochromatic, 100 nm, 20 nm, 10 nm, 5 nm, and 1 nm. These combinations of spectral spacing serve to represent purely discrete spectral configurations approaching a continuous spectrum. All of the initial target configuration are provided in Table 3 as well as the total number of basic images or $f(x, y, \lambda_z)$ were used in the initial hypercube.

Table 3: Initial target configuration table. Identifies the spatial and spectral configuration of the initial target hypercubes and how many images were used. With the exception of the monochromatic configurations all spectral spacing is centered on 600 nm

	Monochromatic	**100 nm**	**20 nm**	**10 nm**	**5 nm**	**1 nm**
Point Like Source	1	5	21	21	21	21
Letters	1	5	21	21	21	21
Backlit AF Bar Chart	1	5	21	21	21	21
Front lit AF bar chart	1	5	21	21	21	21
Random Intensities	1	5	21	21	21	21

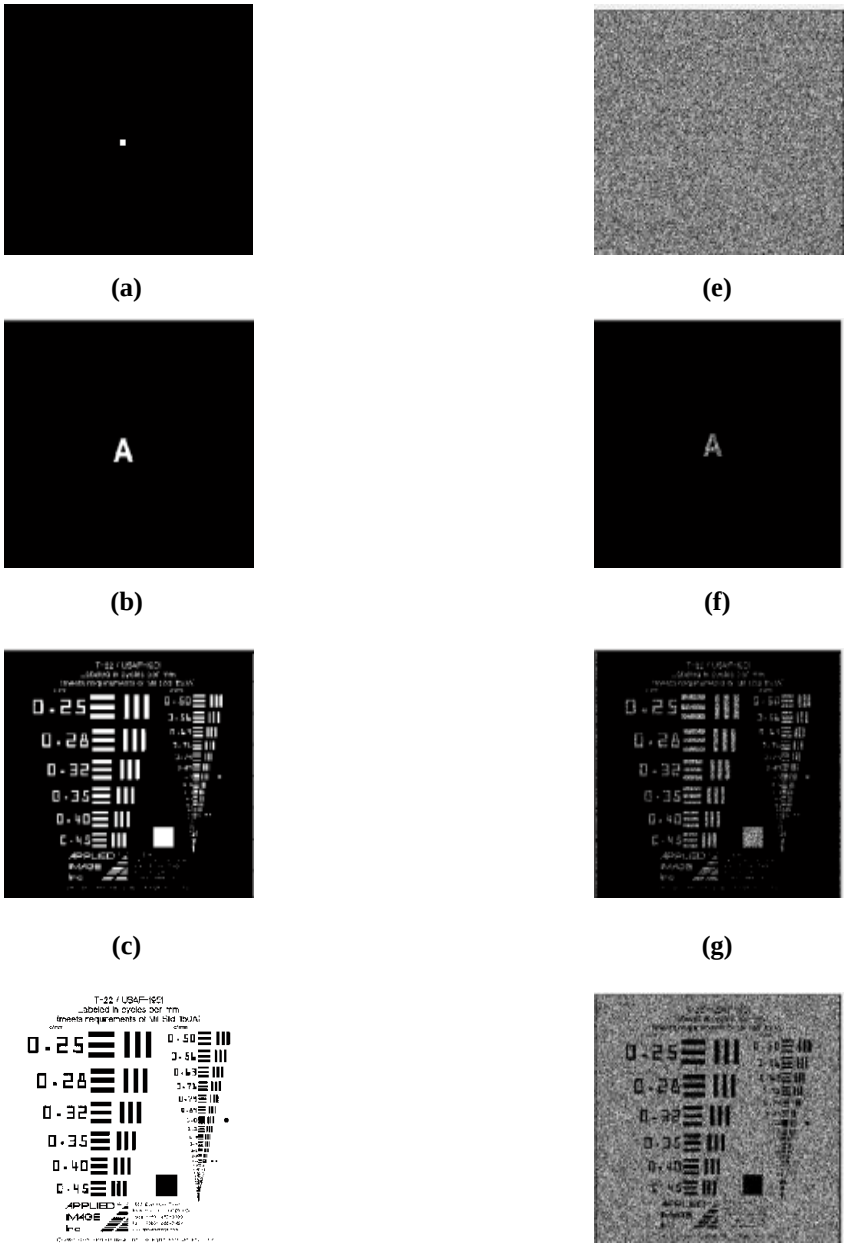

Figure 29. Basic images used in the target hypercube. (a) Is a point like source of 5 by 5 pixels and is the simplest image used in the simulation. In (e) each pixel has a randomly assigned intensity representing the most complicated image used. (b) - (d) are the small letter, back lit AF bar chart, and front lit AF bar chart in which the intensities are always either zero or one hundred. (f) - (h) are the same images as (b) - (d) but the intensities in the lit part are now randomly chosen except for the original zero intensities which remain zero.

4.2 Angle Selection

This area investigates how the range and number of prism angles used in the Back Projection algorithm impacts reconstructed hypercube image quality. The primary strength of chromotomography over other hyperspectral imagers is the speed at which it can record target hypercubes. The optimal prism angle range used in Back Projection algorithm will determine how fast the prism must rotate to capture transient events. Additionally the number of angles required to produce high quality reconstructed images will impact the camera recording speed.

Sections 4.2.1 will provide a step by step example of how the results were compiled for a single target. In Section 4.2.2 the results for using prism angle range of 360 degrees will be summarized as a function of spatial configurations with constant spectral spacing. Section 4.2.3 will again use the prism angle range of 360 degrees but will summarize the results as a function of spectral spacing with a constant spatial configurations. Section 4.2.4 will discuss the important trends that were discovered. Each target's full results are available in Appendix I.

4.2.1 Step By Step Example

The plot in Figure 30 uses five images ($f(x, y, \lambda_z)$) of the backlit AF bar chart, as depicted in Section 4.1, that are spaced 100 nm apart. Each curve represents a range of prism angles of 360, 180, or 90 degrees. The independent variable is the number of projections, $g(\bar{x}, \phi)$, used in the reconstruction. The dependant variable is the mean of the maximum two dimensional cross correlation values between $f(x, y, \lambda_z)$ and $f'(x, y, \lambda_z)$ with error bars representing the standard deviation over λ.

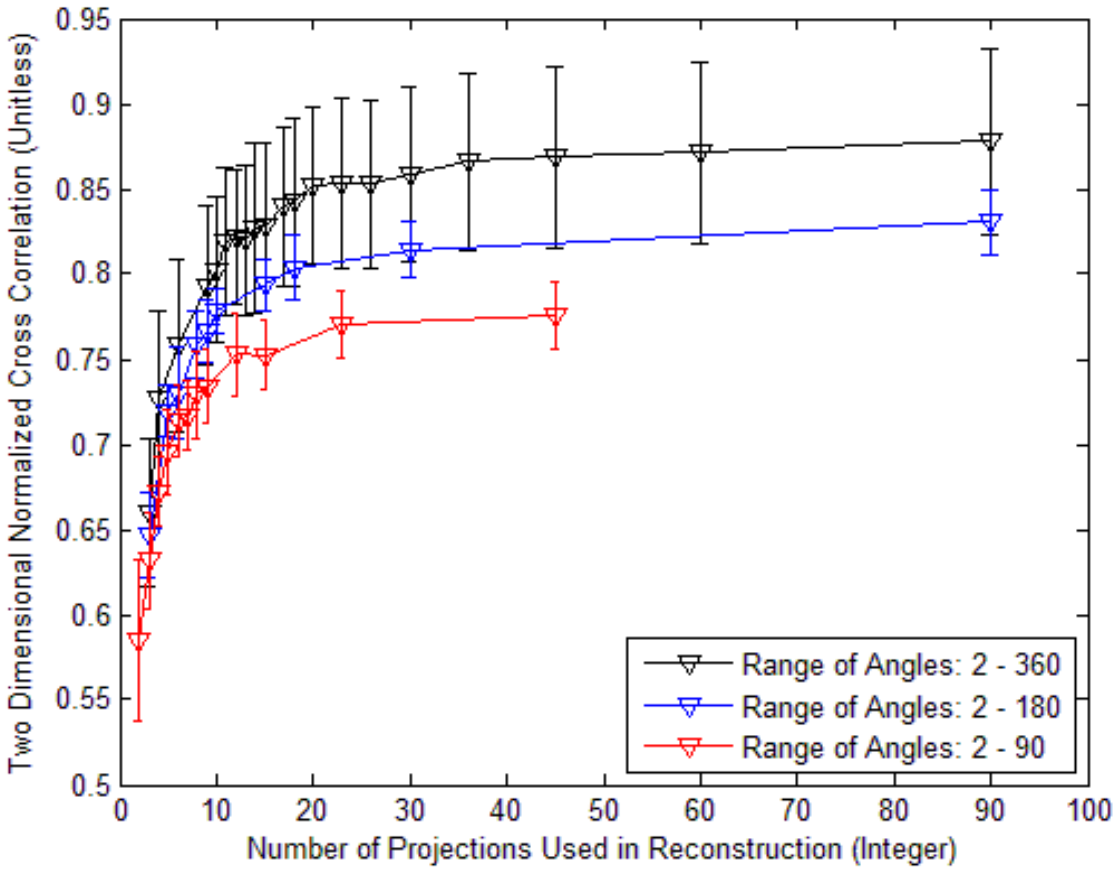

Figure 30. Example plot of how the range and number of prism angles impact reconstructed image quality. This example uses five basic images a backlit bar chart with random intensity, 100 nm separation.

A total of 54 initial target hypercubes were evaluated in this manner using the target sets described in Table 3 and the results are provided in Appendix I. For readability all of the results using the prism angle range of 360 degrees will be condensed into two subsections. In Section 4.2.2 the results will be grouped in terms of constant spectral spacing. In Section 4.2.3 the results will be grouped in terms of basic image

type. Using Table 3 Section 4.2.2 is summarizes the target results in the rows and Section 4.2.3 is summarizing the target results in terms of columns

4.2.2 Results of Summary

The following plots summarize the results of the 54 initial target hypercubes. For each spectral spacing a plot is provided. Each plot contains nine curves, one for each of the spatial configuration. For full results see Appendix I.

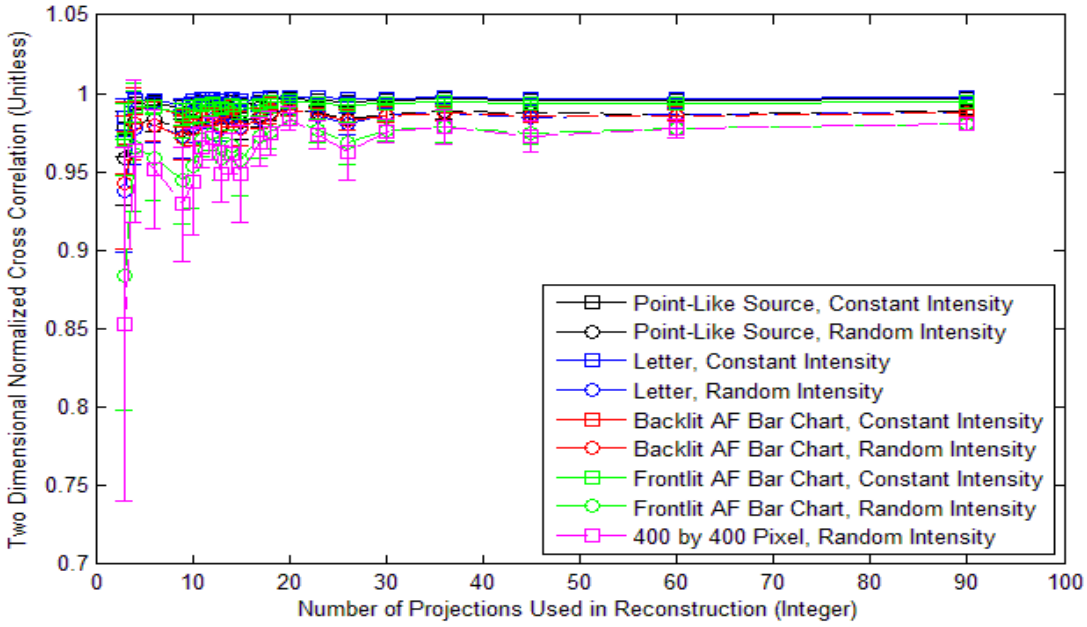

Figure 31. Results summary of monochromatic targets with prism angle range of 360 degrees.

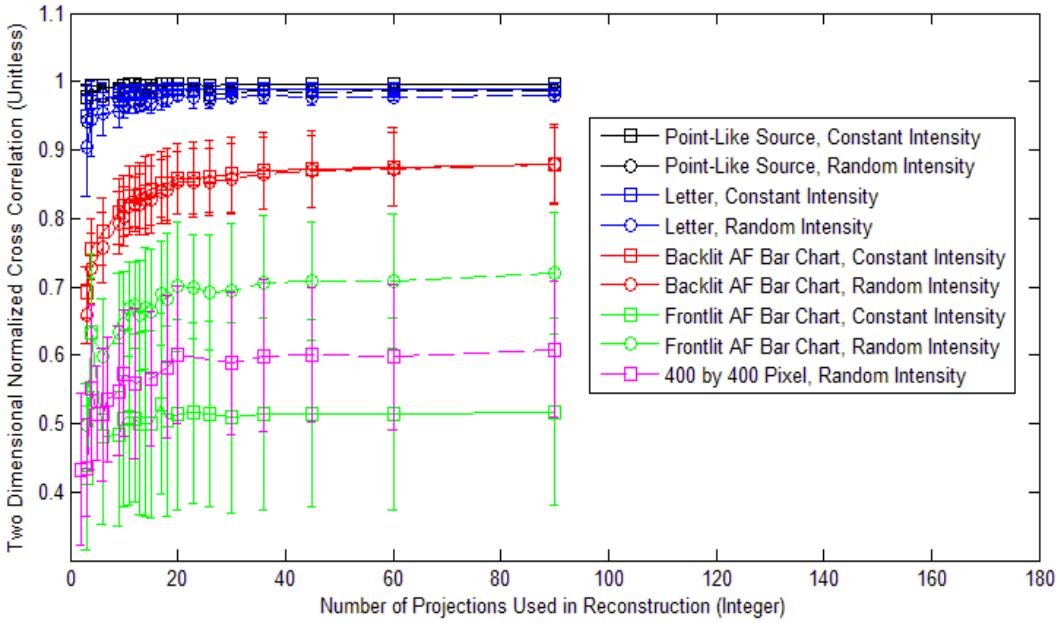

Figure 32. Results summary of 100 nm spaced images with prism angle range of 360 degrees.

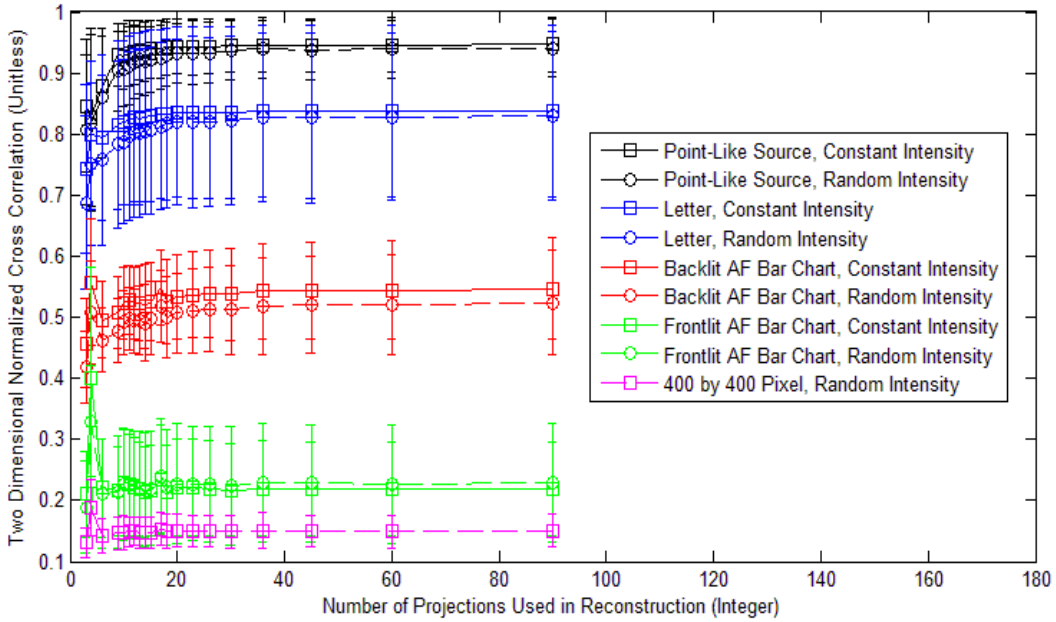

Figure 33. Results summary of 20 nm spaced images with prism angle range of 360 degrees.

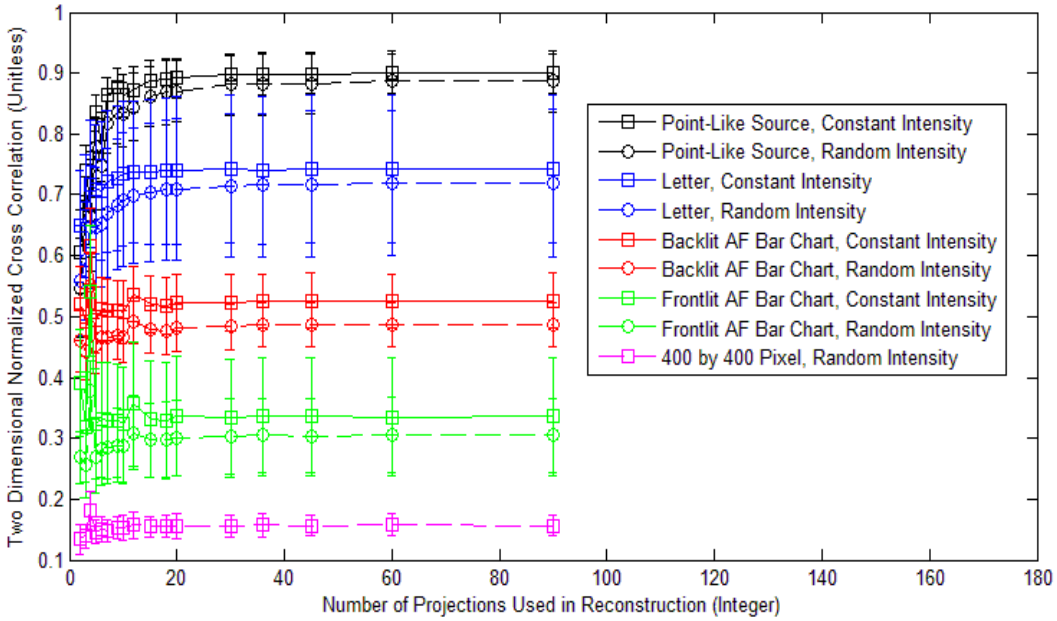

Figure 34. Results summary of 10 nm spaced images with prism angle range of 360 degrees.

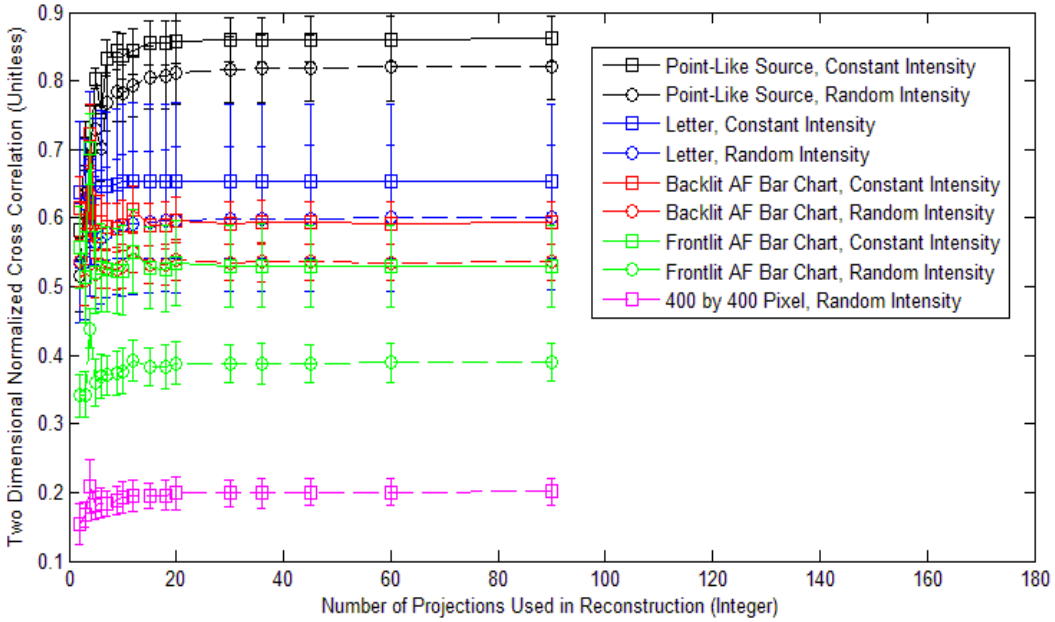

Figure 35. Results summary of 5 nm spaced images with prism angle range of 360 degrees.

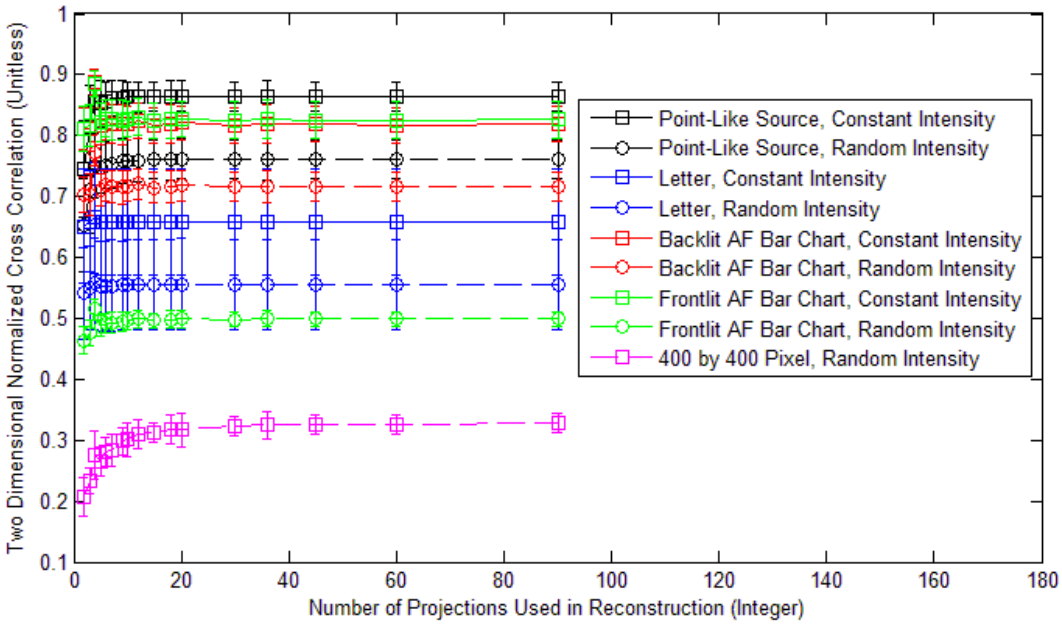

Figure 36. Results summary of 1 nm spaced images with prism angle range of 360 degrees.

4.2.3 Results of Summary

The following plots summarize the results of the 54 initial target hypercubes. For each spatial configuration a plot is provided. Each plot contains six curves, one for each of the spectral spacing. For full results see Appendix I.

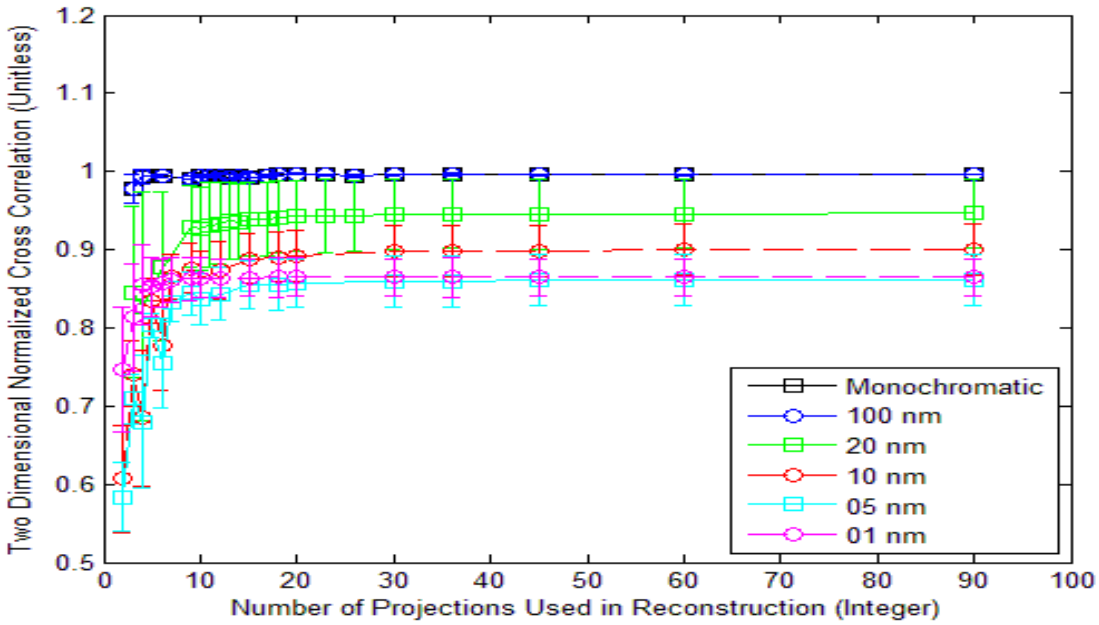

Figure 37. Results summary of point-like source with constant intensity.

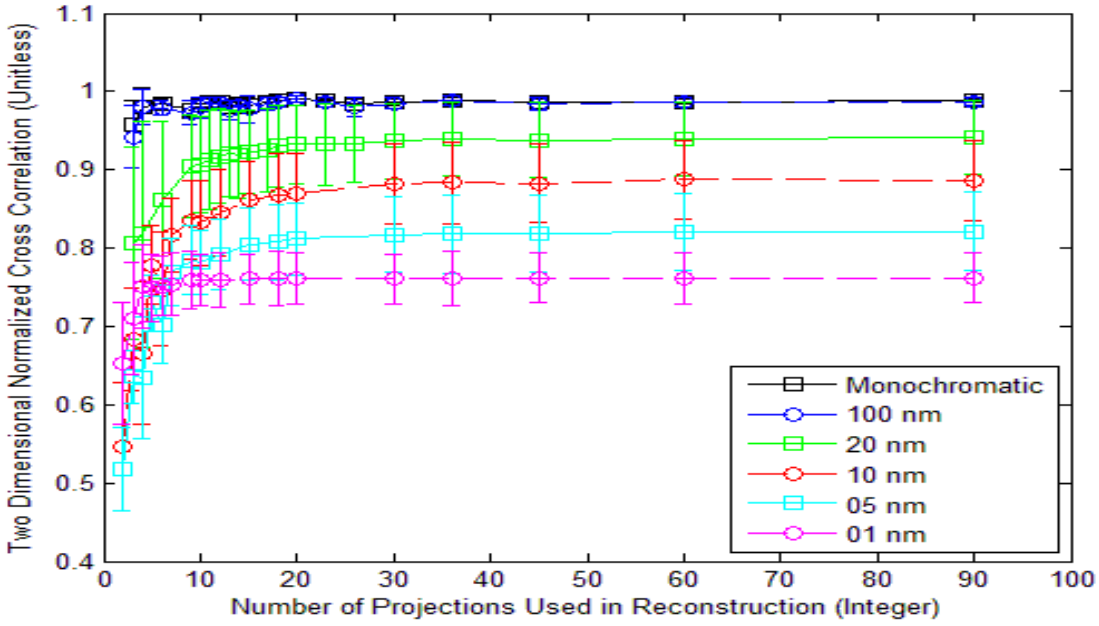

Figure 38. Results summary of point-like source with random intensity with prism angle range of 360 degrees.

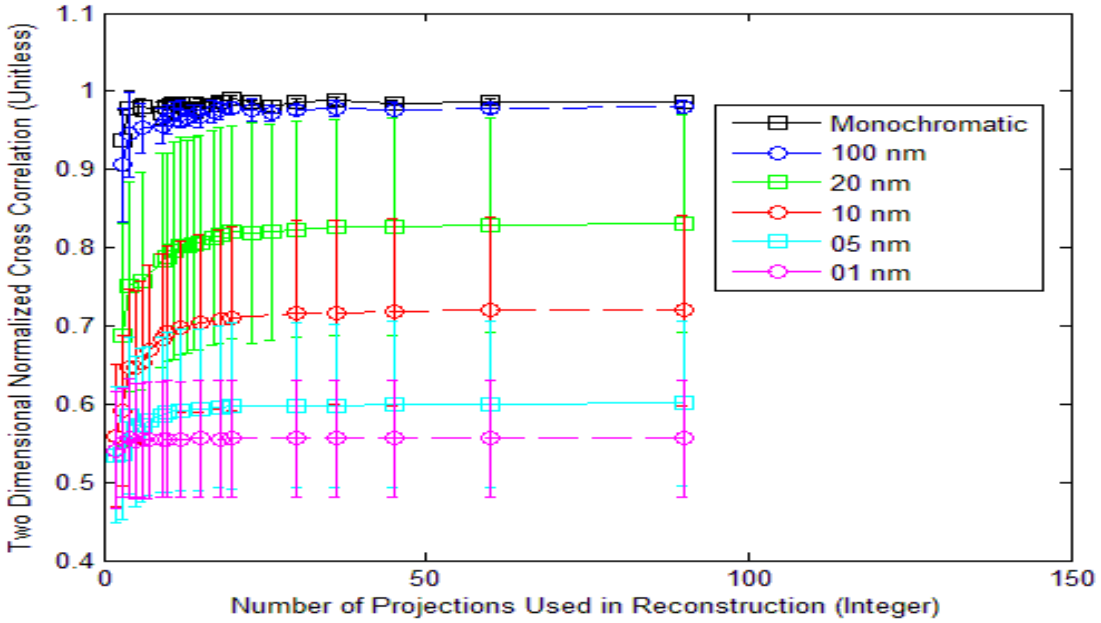

Figure 39. Results summary of capital letters with constant intensity with prism angle range of 360 degrees.

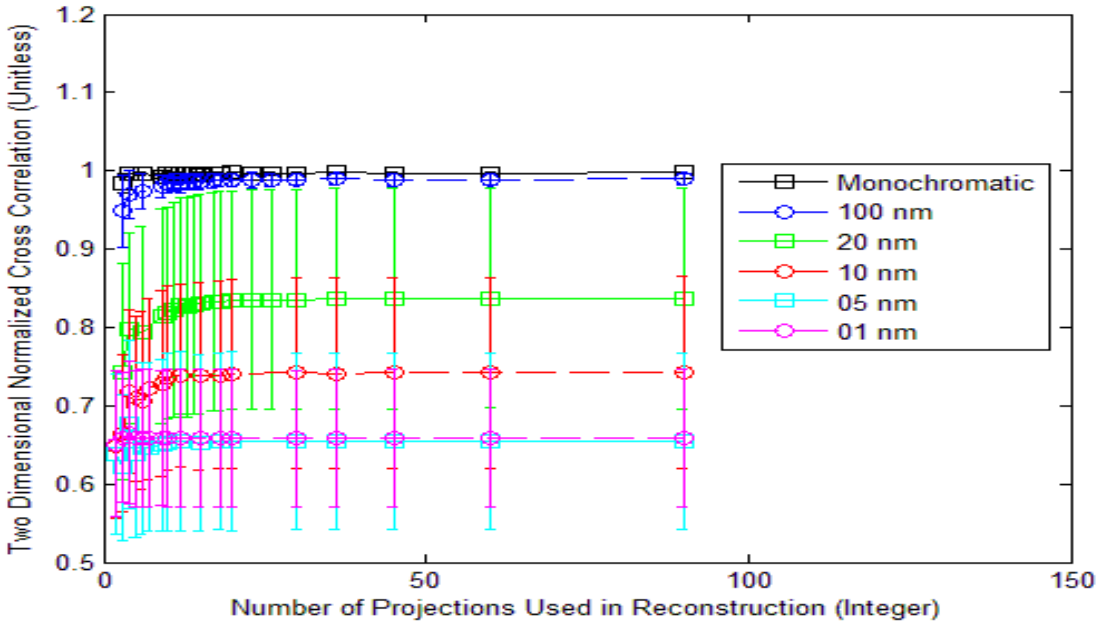

Figure 40. Results summary of capital letters with random intensity with prism angle range of 360 degrees.

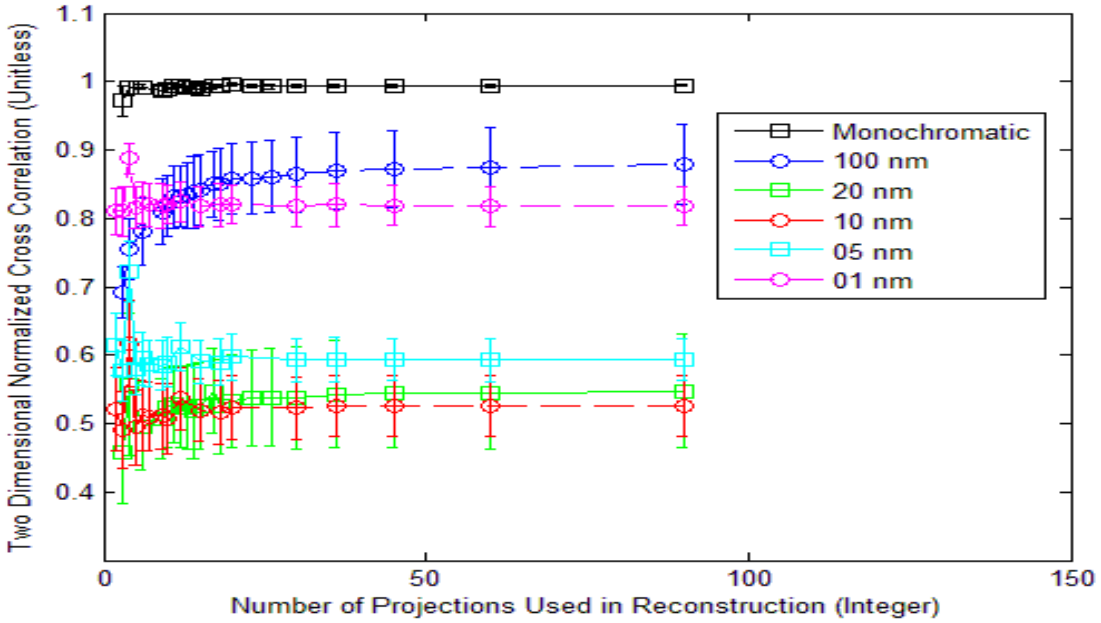

Figure 41. Results summary of backlit AF bar chart with constant intensity with prism angle range of 360 degrees.

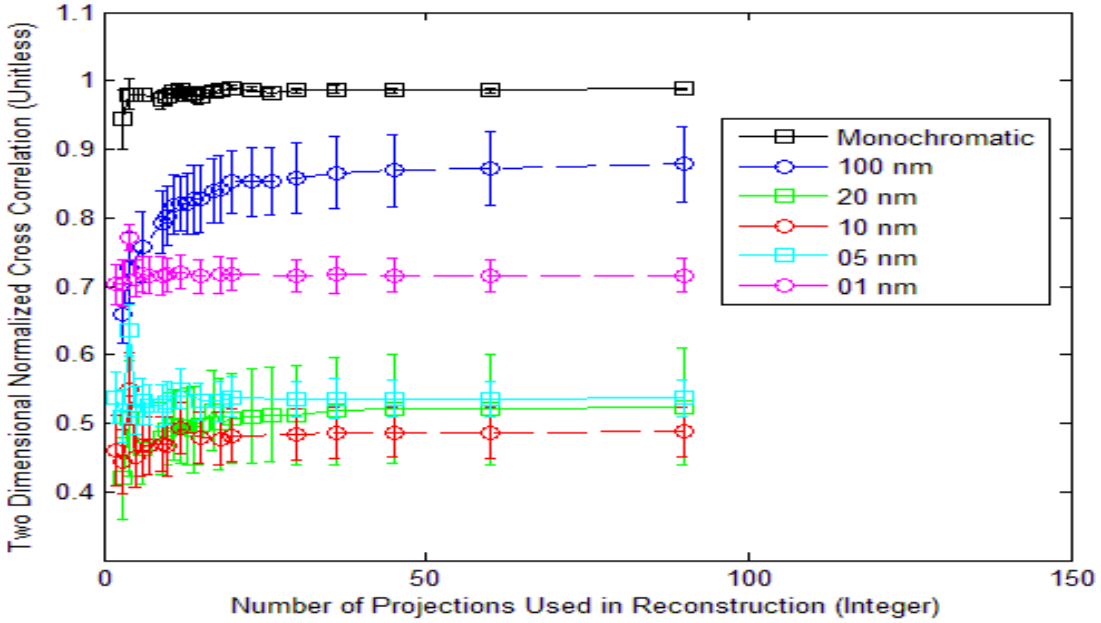

Figure 42. Results summary of backlit AF bar chart with random intensity with prism angle range of 360 degrees.

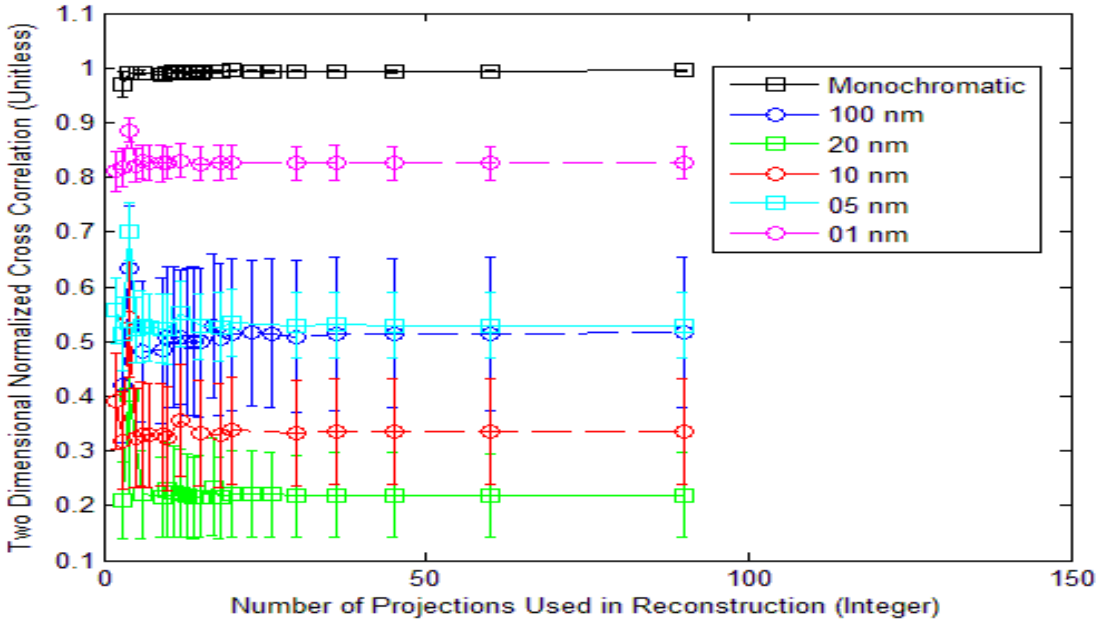

Figure 43. Results summary of front lit AF bar chart with constant intensity with prism angle range of 360 degrees.

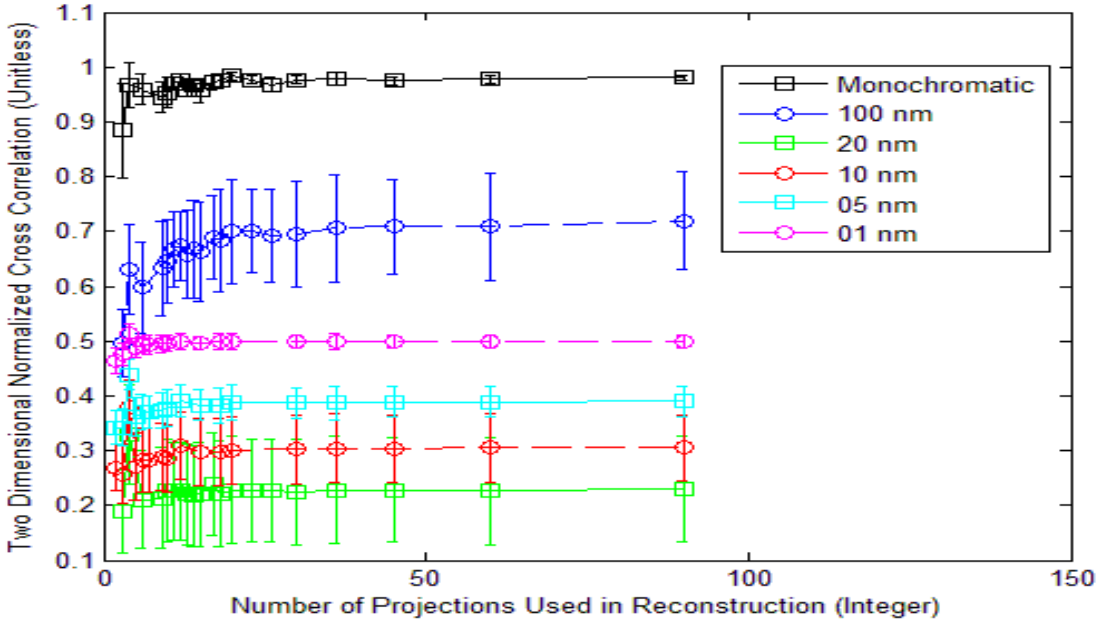

Figure 44. Results summary of front lit AF bar chart with random intensity with prism angle range of 360 degrees.

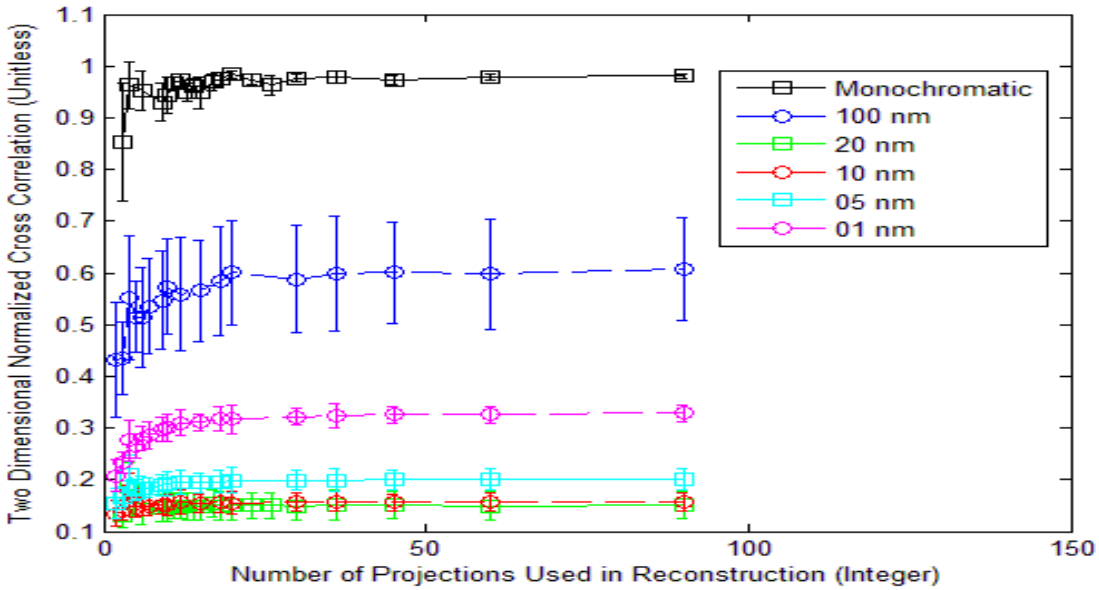

Figure 45. Results summary of 400x 400 random intensity with prism angle range of 360 degrees.

4.2.4 General Results

The best reconstructed image quality was observed in the monochromatic hypercubes in which the normalized cross correlation approached one. The benefit of using monochromatic target hypercubes is that there should not be any off-wavelength artifacts to degrade the reconstructed image quality. The range of prism angles used made very little difference in the image quality in these cases.

With the exception of the monochromatic hypercubes, all of the other reconstructed image quality approached a horizontal asymptote at approximately 20 projections. The value that the curves approached was dependent on the range of prism angles used in the reconstruction and the configuration of the initial target hypercube. In all cases the greater the prism angle range the greater the maximum normalized cross correlation.

4.3 Comparison of Back Projection to Shift and Place Reconstructed Images

In this portion the new algorithm Shift and Place will be compared to the Back Projection method. The results will be plotted individually for each basic image type as defined in Section 4.1. The independent variable is the number of projections used in the reconstruction. The dependent variable will be the normalized cross correlation between the reconstructed images and the initial target images. There will be two curves representing the two reconstruction algorithms being evaluated. The evaluation will use the prism angle range of 360 degrees.

4.3.1 20 Nanometer Separation

Each basic image, described in Section 4.1, will be used to create initial target hypercubes which contain 21 images that are spaced 20 nanometers apart from 400 to 800 nanometers. The analysis in this section is nearly identical to Section 4.2 with the exception of instead of comparing multiple ranges of prism angles the focus is on the two reconstruction algorithms.

.

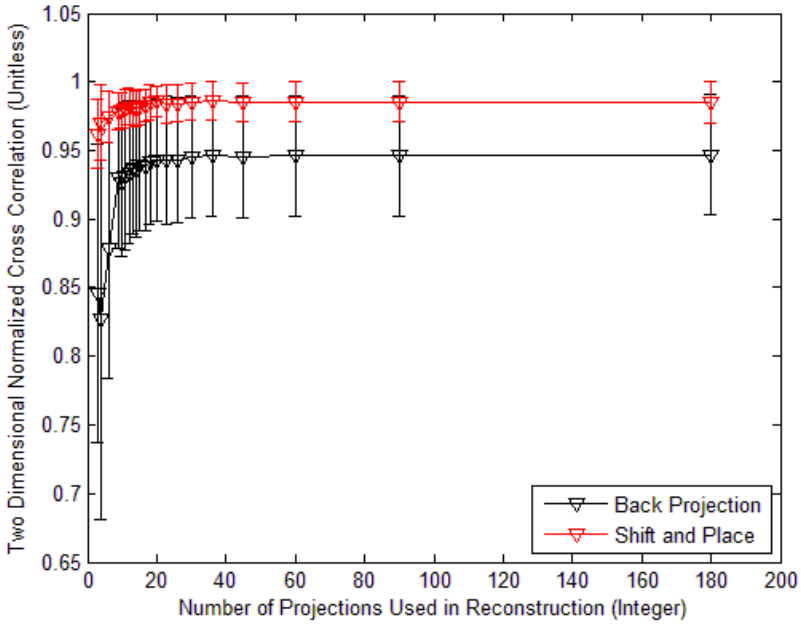

Figure 46. Comparison of Back Projection and Shift and Place using point like source with constant intensity target hypercube, 20 nm separation.

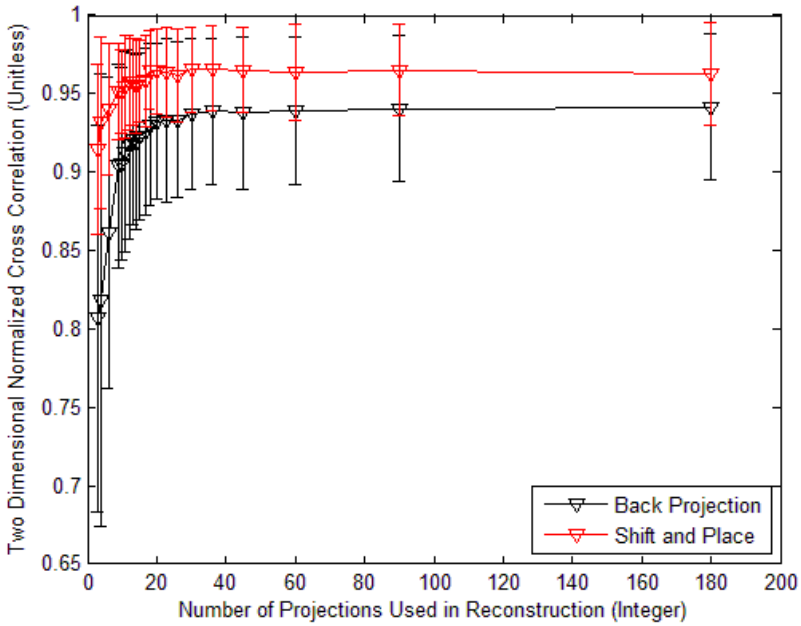

Figure 47. Comparison of Back Projection and Shift and Place using point like source with random intensity target hypercube, 20 nm separation.

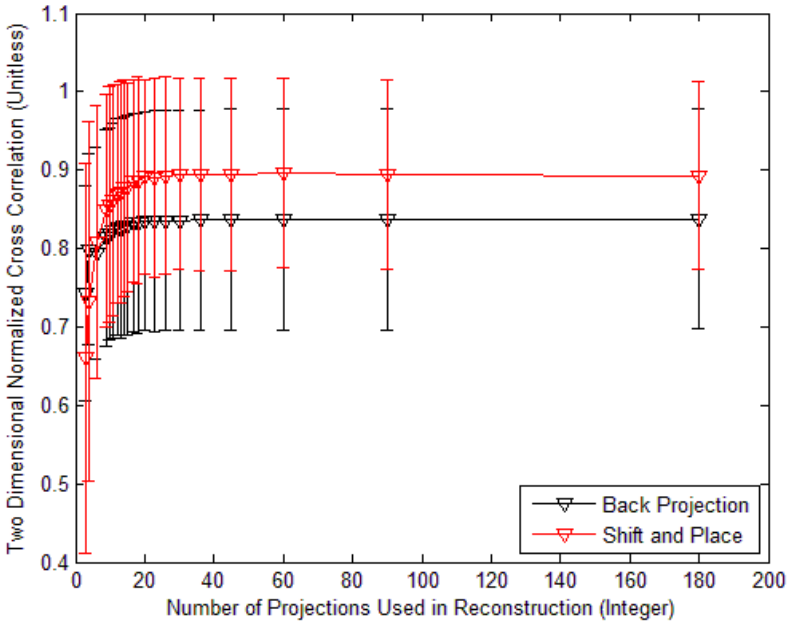

Figure 48. Comparison of Back Projection and Shift and Place using letter with constant intensity target hypercube, 20 nm separation.

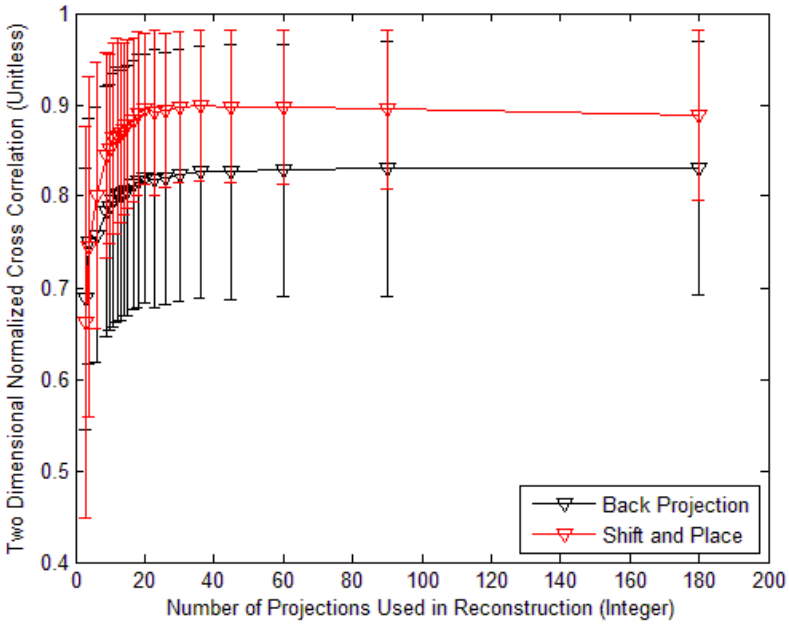

Figure 49. Comparison of Back Projection and Shift and Place using letter with random intensity target hypercube, 20 nm separation.

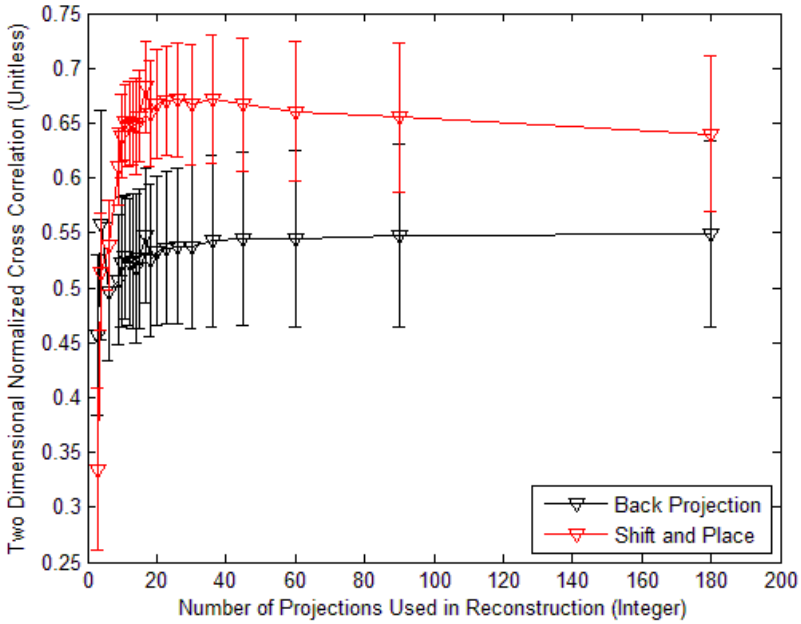

Figure 50. Comparison of Back Projection and Shift and Place using backlit AF Bar chart with constant intensity target hypercube, 20 nm separation.

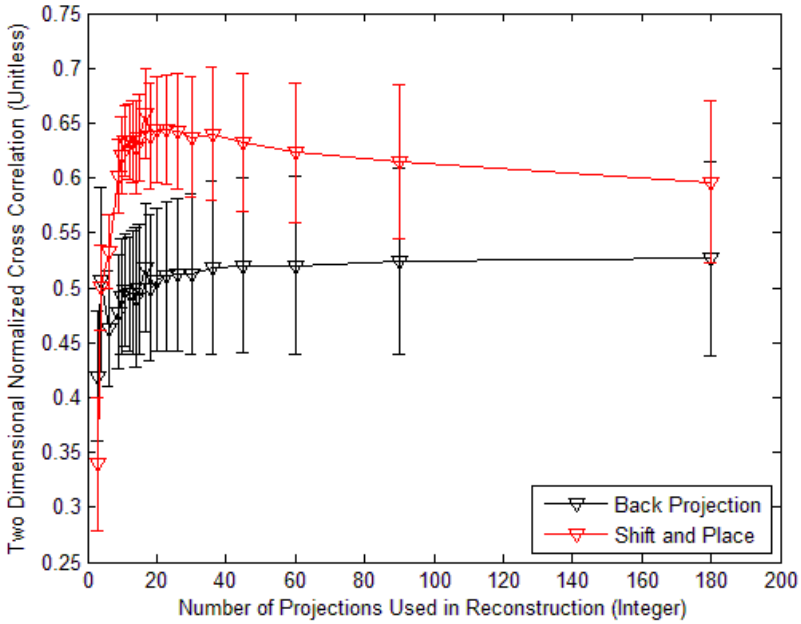

Figure 51. Comparison of Back Projection and Shift and Place using backlit AF Bar chart with random intensity target hypercube, 20 nm separation.

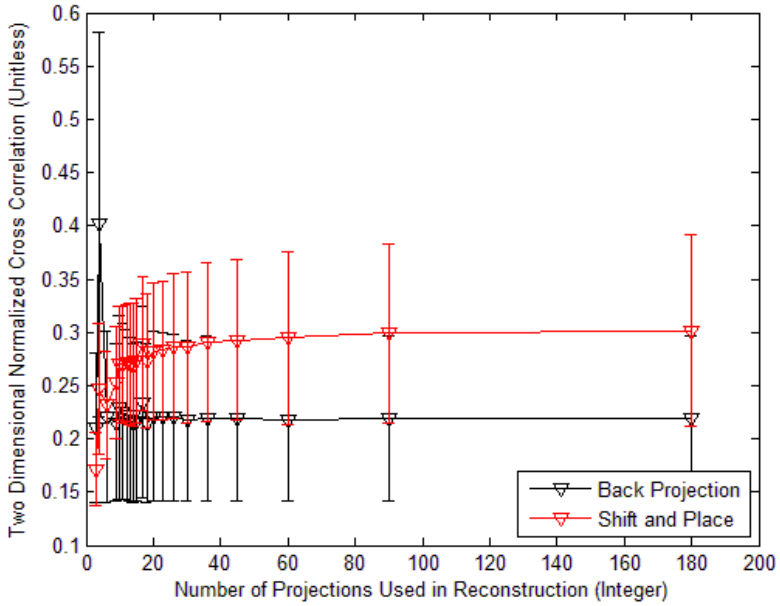

Figure 52. Comparison of Back Projection and Shift and Place using front lit AF Bar chart with constant intensity target hypercube, 20 nm separation.

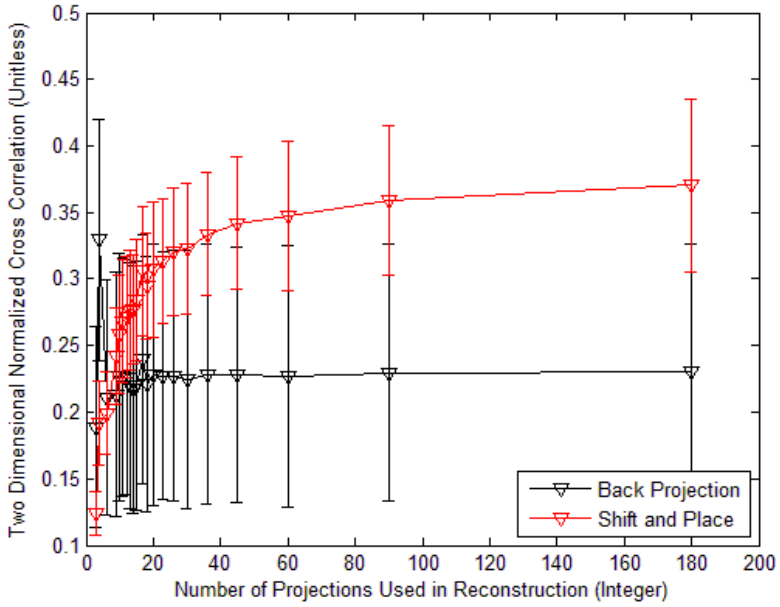

Figure 53. Comparison of Back Projection and Shift and Place using front lit AF Bar chart with random intensity target hypercube with 20 nm separation.

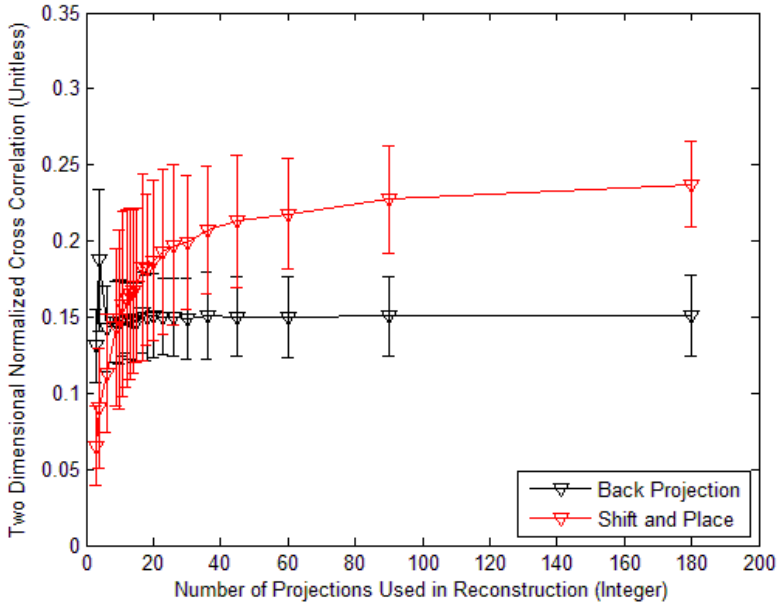

Figure 54. Comparison of Back Projection and Shift and Place using 400x400 random intensity target hypercube, 20 nm separation.

Provided at least 20 projections were used in the reconstruction, the Shift and Place algorithm performed better than the Back Projection algorithm. In five of the nine cases the reconstructed image quality actually started to decrease as the number of projections increased. This may indicate that the placement mechanism may be too sensitive to slight variations in the recorded projections.

4.3.2 5 Nanometer Separation

The analysis performed in this section is identical to Section 4.3.1 with the exception of the initial hypercube construction. Nine hypercubes will be evaluated in this section using the basic image type described in Section 4.1. Each target hypercube will contain 21 which are spaced 5 nanometers apart from 550 to 650 nanometers

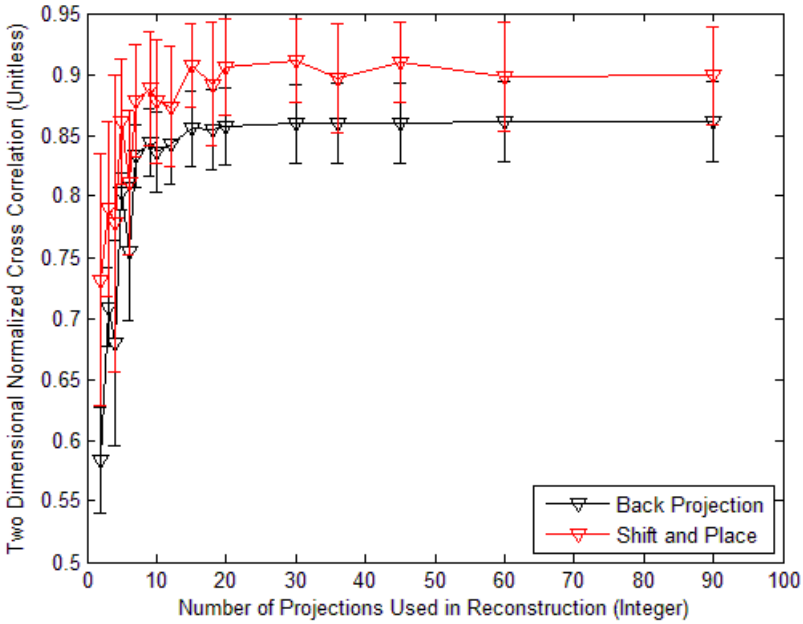

Figure 55. Comparison of Back Projection and Shift and Place using point like source with constant intensity, 5 nm separation.

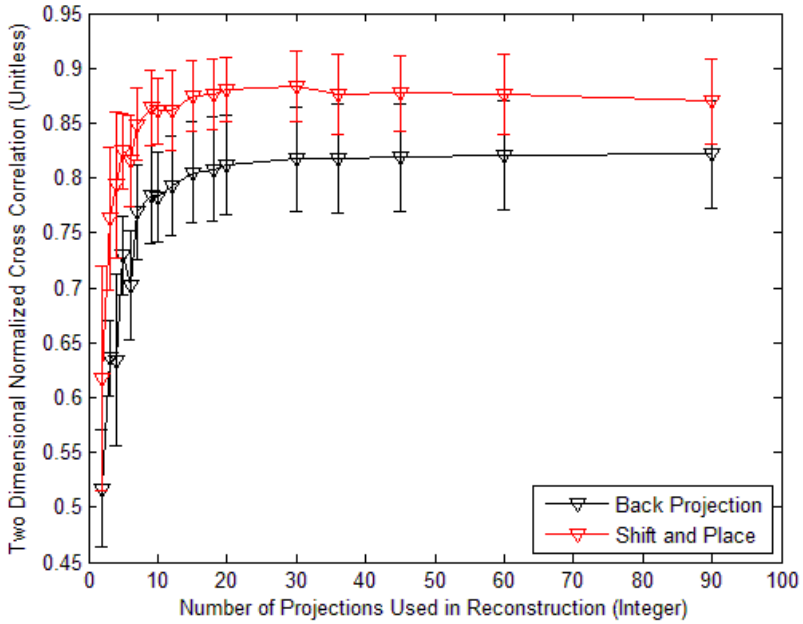

Figure 56. Comparison of Back Projection and Shift and Place using point like source with random intensity, 5 nm separation.

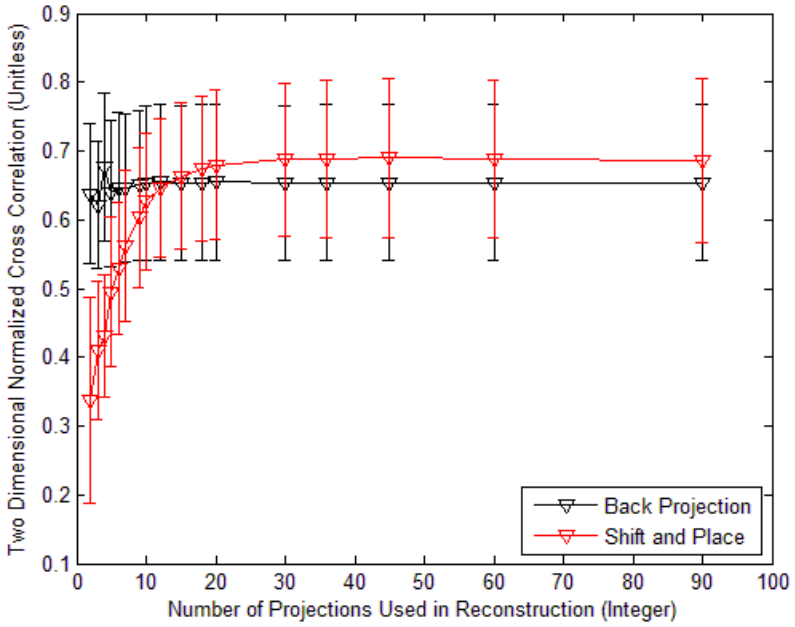

Figure 57. Comparison of Back Projection and Shift and Place using letter with constant intensity, 5 nm separation.

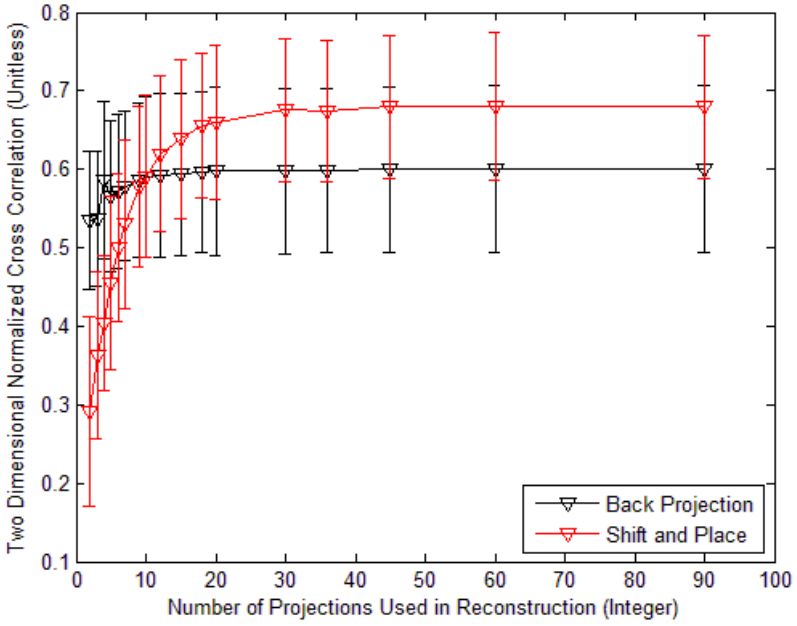

Figure 58. Comparison of Back Projection and Shift and Place using letter with random intensity, 5 nm separation.

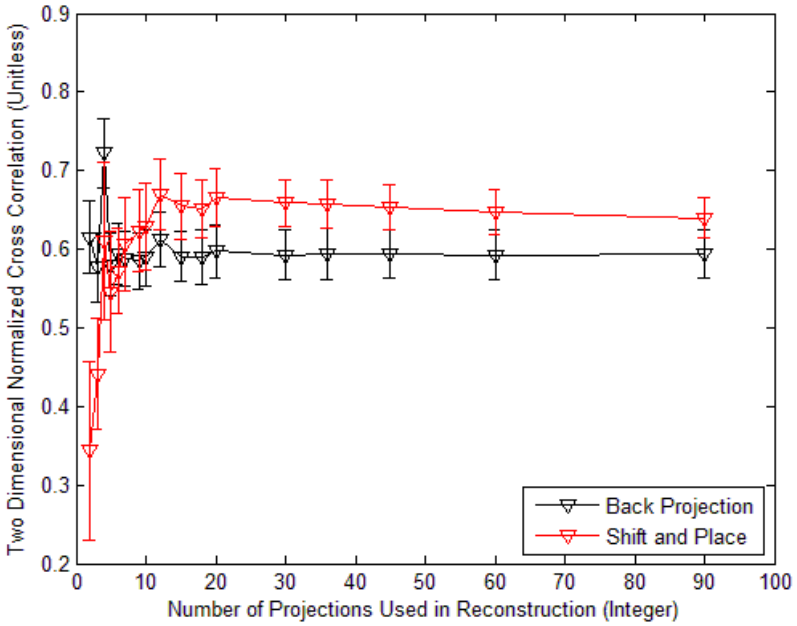

Figure 59. Comparison of Back Projection and Shift and Place using backlit AF bar chart with constant intensity, 5 nm separation.

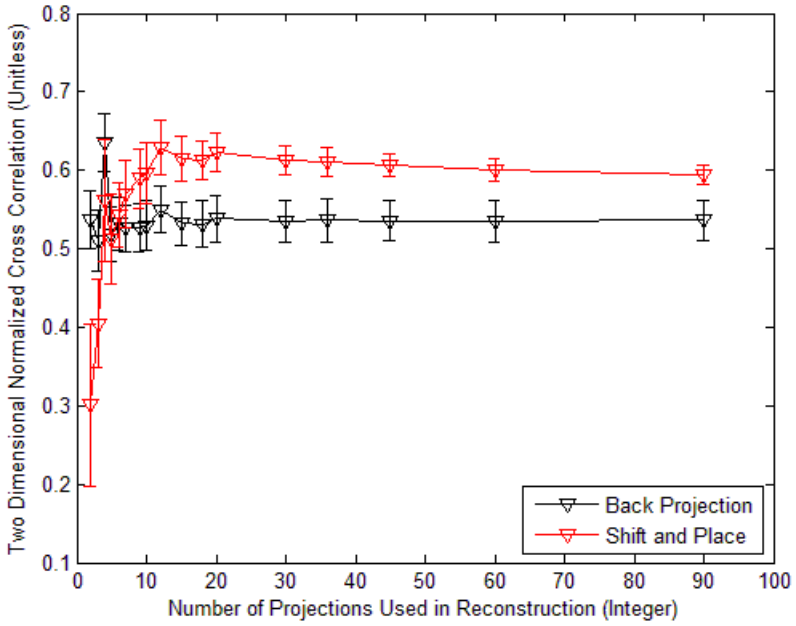

Figure 60. Comparison of Back Projection and Shift and Place using backlit AF bar chart with random intensity, 5 nm separation.

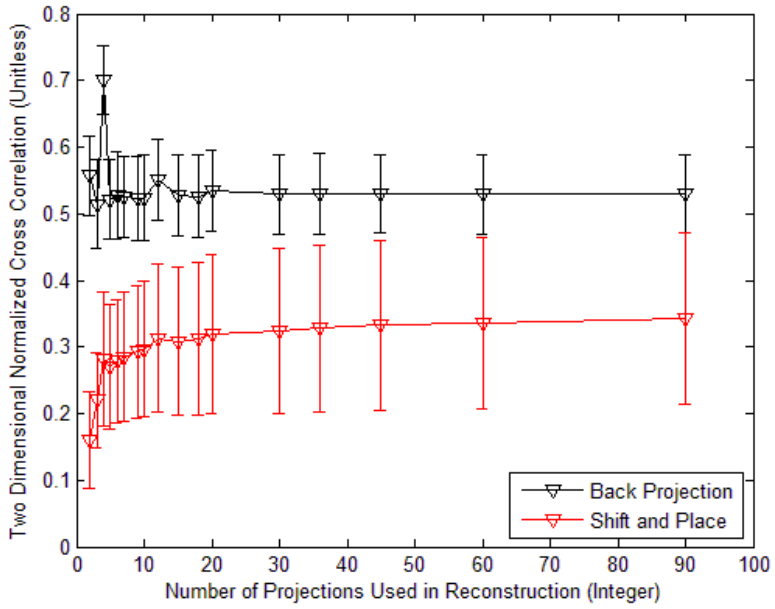

Figure 61. Comparison of Back Projection and Shift and Place using front lit AF bar chart with constant intensity, 5 nm separation.

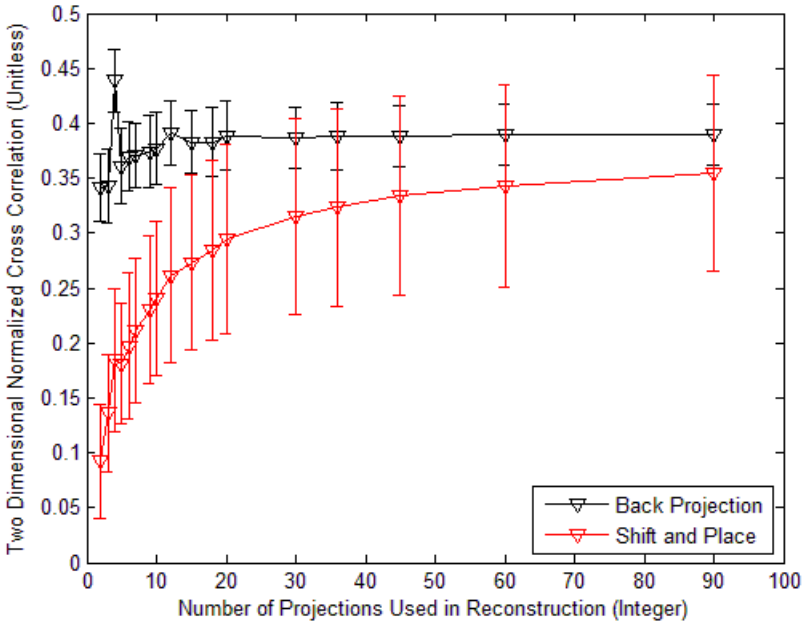

Figure 62. Comparison of Back Projection and Shift and Place using front lit AF bar chart with random intensity, 5 nm separation.

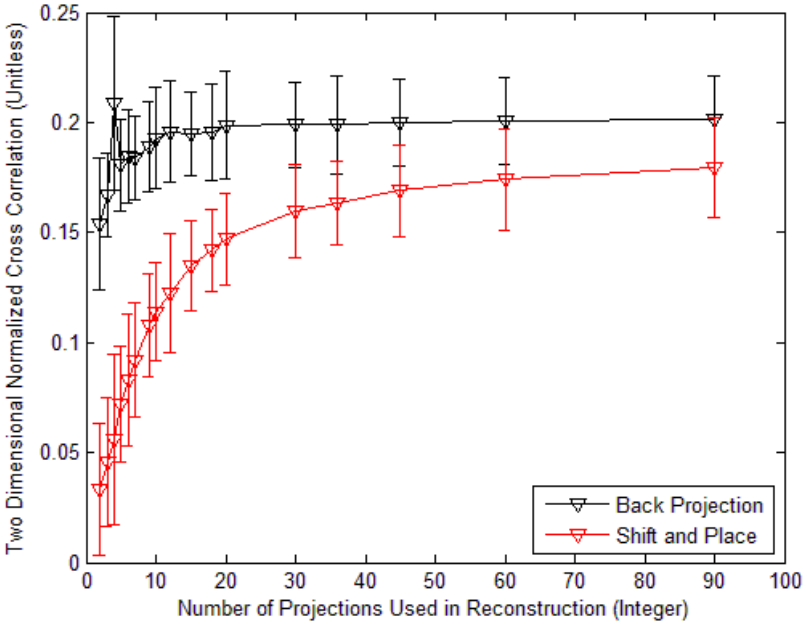

Figure 63. Comparison of Back Projection and Shift and Place using 400x400 random pixel intensity, 5 nm separation.

Provided at least 20 projections were used in the reconstruction the Shift and Place algorithm performed better than the Back Projection algorithm six out of the nine target sets. The six target sets it performed the best in were the point-like source, letters, and the back lit AF Bar chart, which were spatially the least complex hypercubes used in the evaluation. Back Projection worked better in the more spatially complex target sets.

4.4 Impact of Optical Aberrations

This section focuses on how optical aberrations in the recorded images impact the reconstructed image quality. A plot will be provided for each target hypercube in which the independent variable is aberration in terms of number of waves and the dependant variable is the reconstructed image quality. Each initial target hypercube will contain 21

images which are spaced 20 nanometers apart from 400 to 800 nanometers. Each reconstruction will utilize a prism angle range of 360 degrees and 90 projections equally spaced in 4 degree increments.

The reconstructed image quality, as seen in Section 4.2, is highly dependent on the complexity of the initial hypercube. As the spatial complexity of the initial hypercube increased the reconstructed image quality decreased. When evaluating a reconstructed hypercube with optical aberrations a determination needs to be made in whether the decreases in image quality is a result of reconstruction, or simply the optical aberration that is applied.

One way to determine the source of the decrease in image quality is to define three sets of images for comparison. The first image set is the initial target hypercube images. The second image set can be created from the initial target hypercube images in which the aberration is applied to the initial target hypercube. The third set is the reconstructed image.

The second set of images can be created by processing each target hypercube image individually through the Zemax optical model with the Zernike mask configured to apply the optical aberration, but without the prism. The result is a target hypercube image in which the optical aberrations have been applied, but no chromatic dispersion. For purposes of this paper the second image set will be referred to as Zernike images. It is important to note that these Zernike images, although produced by the optical model are not the same as the reconstructed images, which are based on using multiple projections ($g(\bar{x},\phi)$) and a reconstruction algorithm, as seen in Figure 64.

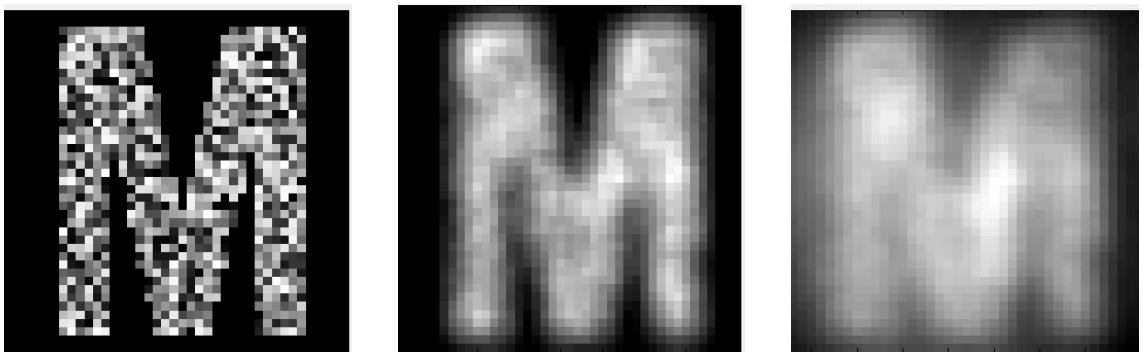

(a) **(b)** **(c)**

Figure 64. Comparison of an initial image to the Zernike image and reconstructed image. (a) contains the original hypercube image. Image (b) is an image with the optical aberrations applied to it or Zernike image. Image (c) is the reconstructed image.

These three sets of images enable a comparison to be made of the initial hypercube images to the Zernike images and the initial hypercube images to the reconstructed images. A third comparison can also be made of the Zernike image to the reconstructed image. These three comparisons will comprise the analysis of this section.

4.4.1 Optical Aberration using Zernike Polynomial 4: "Defocus"

The analysis in this section will utilize Zernike polynomial number four which closely resembles the defocus optical aberration and will be performed as described in Section 4.4. Six hypercubes will be used in the evaluation. The basic image types used are the letter, backlit AF bar chart, and front lit AF bar chart and the constant intensity and random intensities are used.

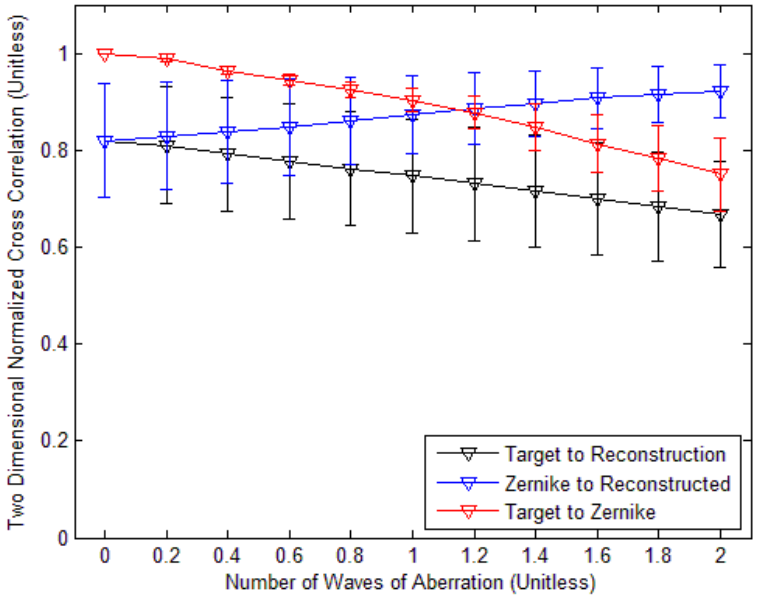

Figure 65. Optical aberration evaluation using image type letter with constant intensity, Zernike polynomial number 4.

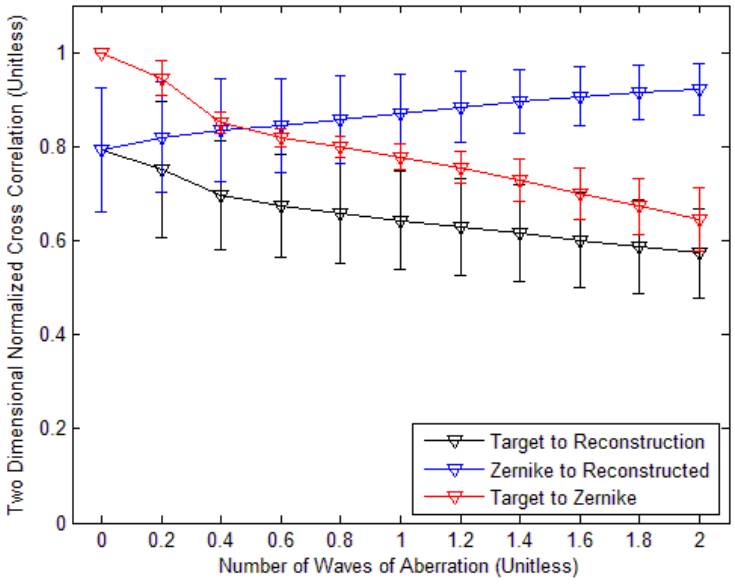

Figure 66. Optical aberration evaluation using image type letter with random intensity, Zernike polynomial number 4.

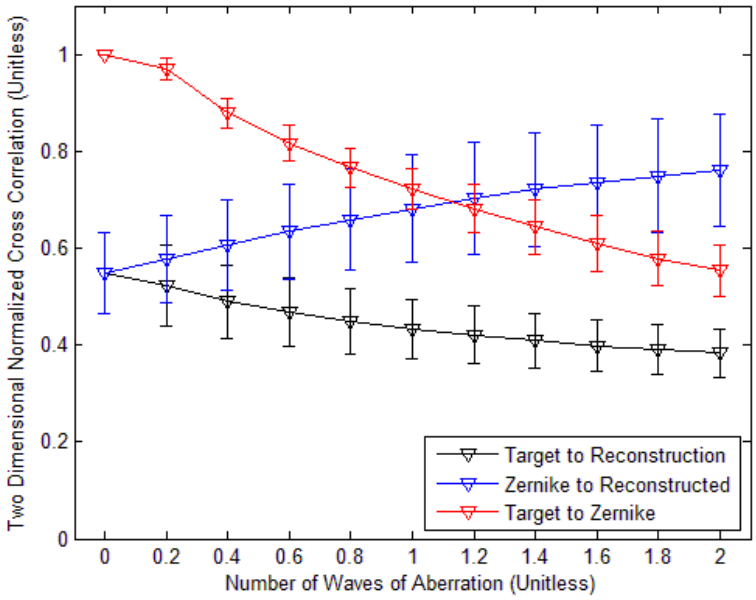

Figure 67. Optical aberration evaluation using image type backlit AF bar chart with constant intensity, Zernike polynomial number 4.

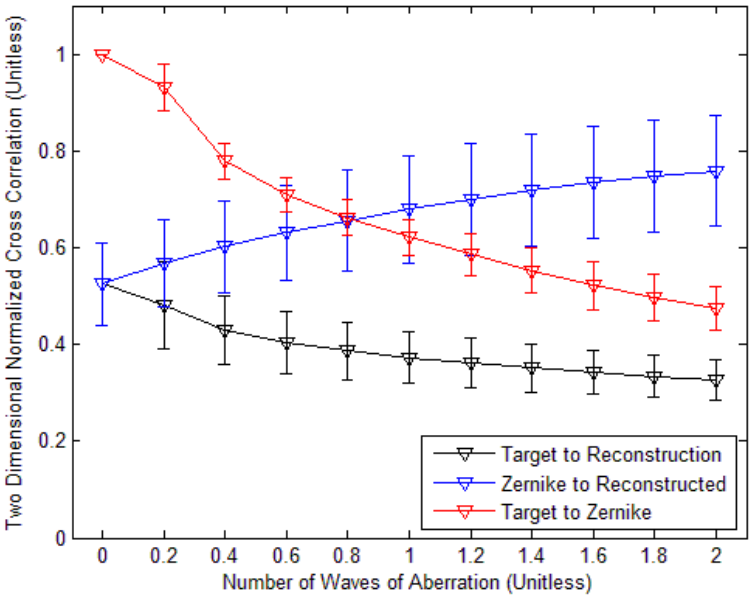

Figure 68. Optical aberration evaluation using image type backlit AF bar chart with random intensity, Zernike polynomial number 4.

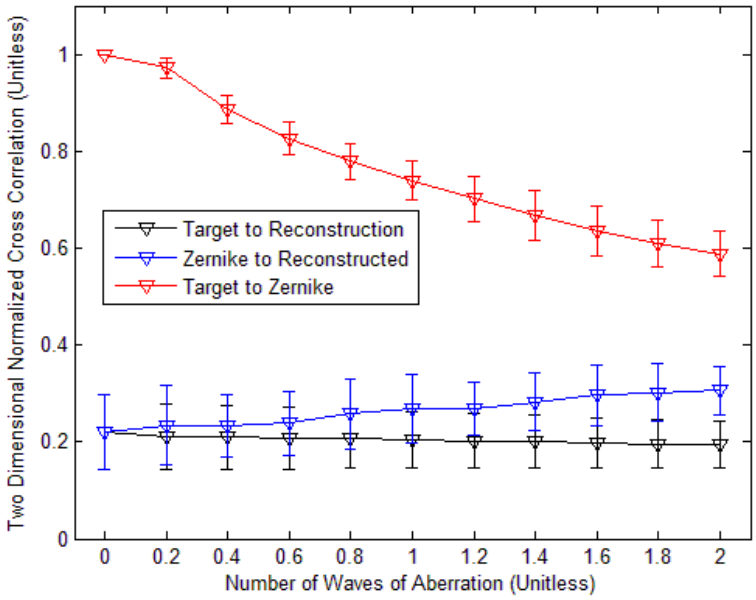

Figure 69. Optical aberration evaluation using image type front lit AF bar chart with constant intensity, Zernike polynomial number 4.

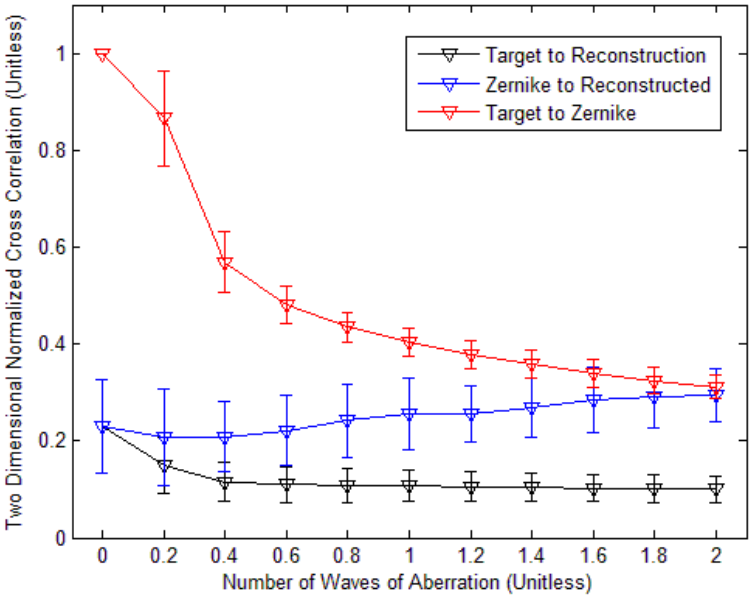

Figure 70. Optical aberration evaluation using image type front lit AF bar chart with random intensity, Zernike polynomial number 4.

A number of observations can be made. First the image quality decrease from the applied optical aberration, as seen in the Zernike images, varied greatly from image type to image type. Second, even minor amounts of optical aberrations immediately impact the reconstructed image quality. Third, at higher optical aberrations the reconstructed image more closely matches the Zernike image, which means the rate of image quality decrease between the optical aberration image and the reconstructed optical aberration image vary differently from each other.

4.4.2 Optical Aberration using Zernike Polynomial 5: "Astigmatism"

The analysis in this section will utilize Zernike polynomial number five which closely resembles the astigmatism optical aberration and will be performed as described in Section 4.4. Six hypercubes will be used in the evaluation. The basic image types used are the letter, backlit AF bar chart, and front lit AF bar chart with constant intensity and random intensities.

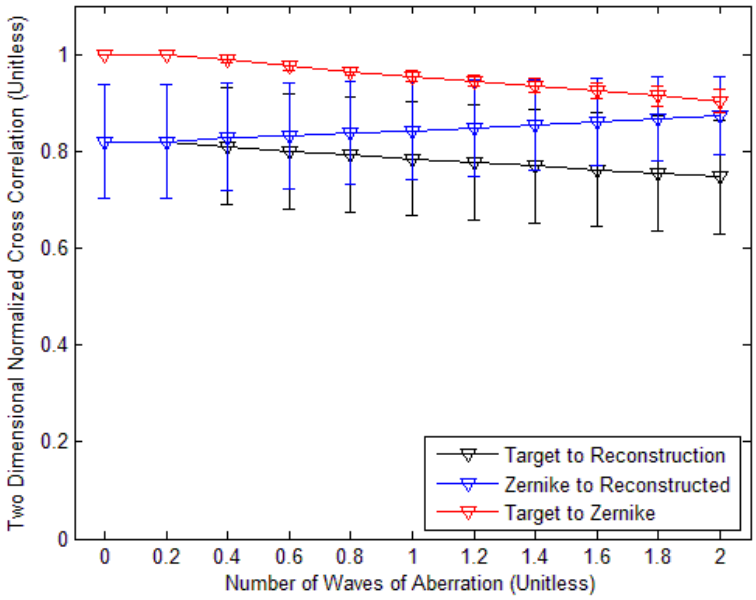

Figure 71. Optical aberration evaluation using image type letter with constant intensity, Zernike polynomial number 5.

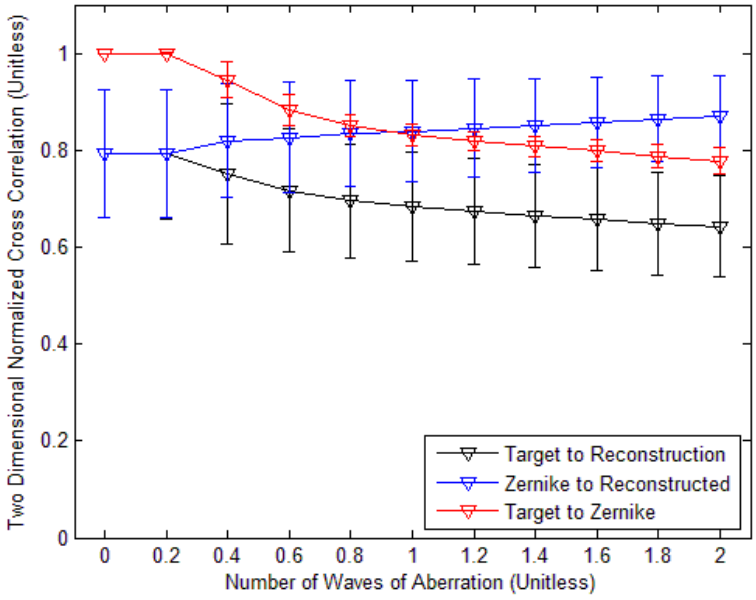

Figure 72. Optical aberration evaluation using image type letter with random intensity, Zernike polynomial number 5.

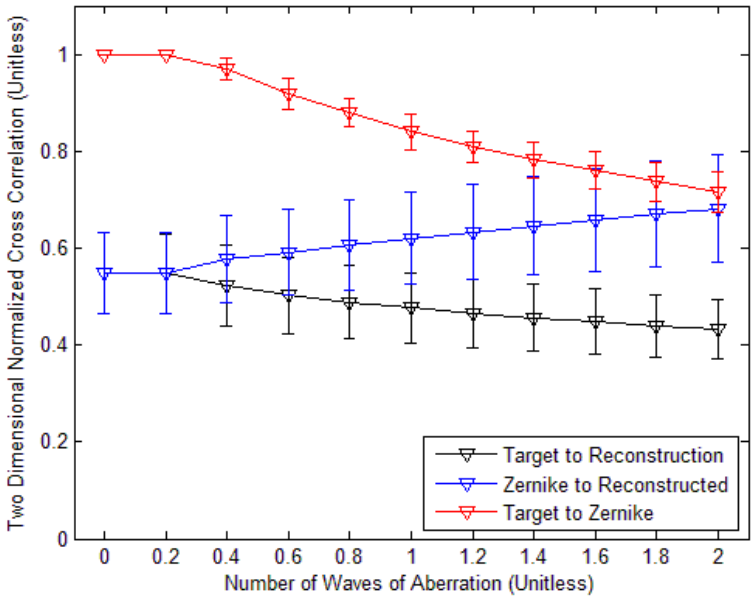

Figure 73. Optical aberration evaluation using image type backlit AF bar chart with constant intensity, Zernike polynomial number 5.

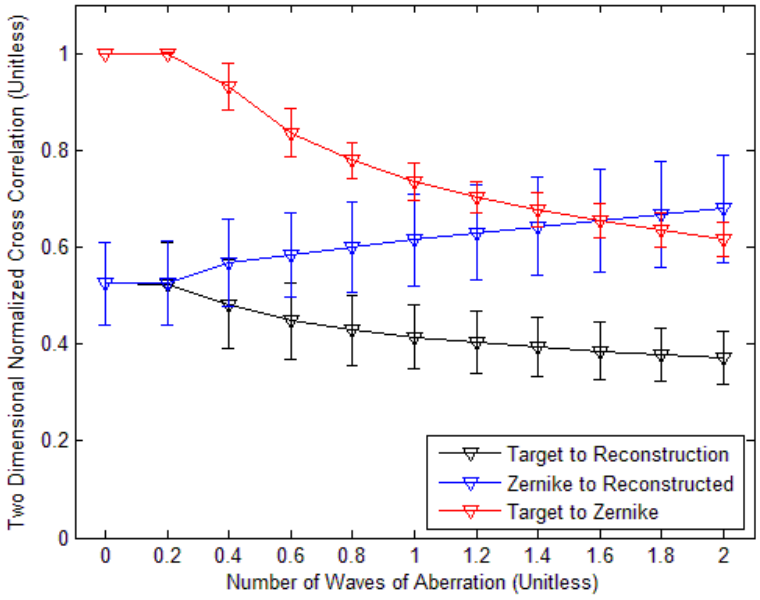

Figure 74. Optical aberration evaluation using image type backlit AF bar chart with random intensity, Zernike polynomial number 5.

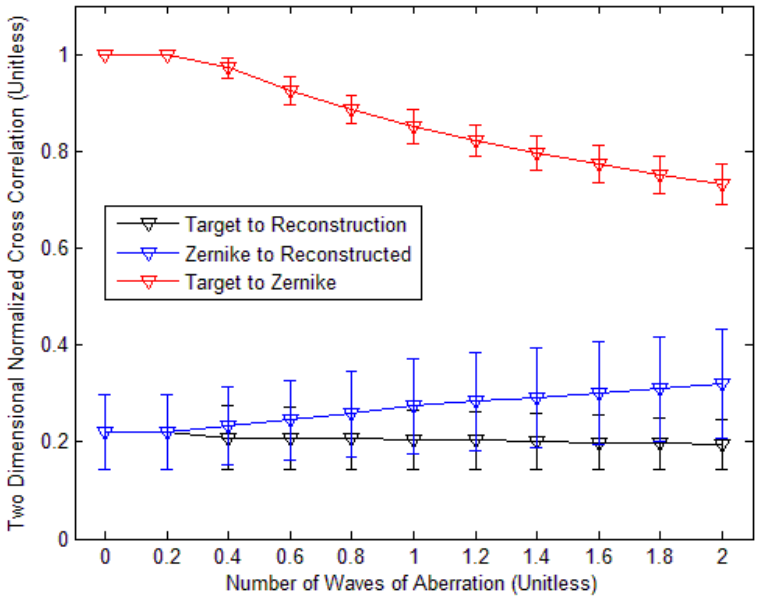

Figure 75. Optical aberration evaluation using image type front lit AF bar chart constant intensity, Zernike polynomial number 5.

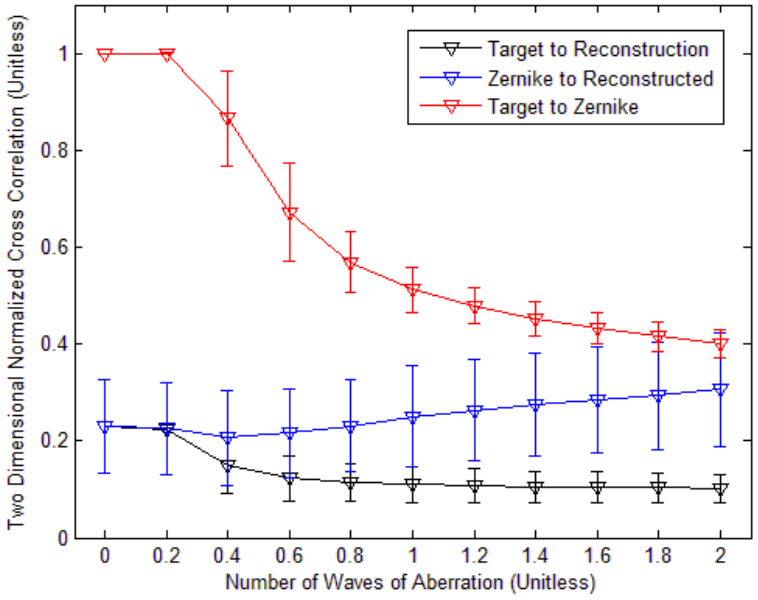

Figure 76. Optical aberration evaluation using image type front lit AF bar chart with random intensity, Zernike polynomial number 5.

4.4.3 Optical Aberration using Zernike Polynomial 7: "Coma"

The analysis in this section will utilize Zernike polynomial number seven which closely resembles the coma optical aberration and will be performed as described in Section 4.4. Six hypercubes will be used in the evaluation. The basic image types used are the letter, backlit AF bar chart, and front lit AF bar chart and the constant intensity and random intensities are used.

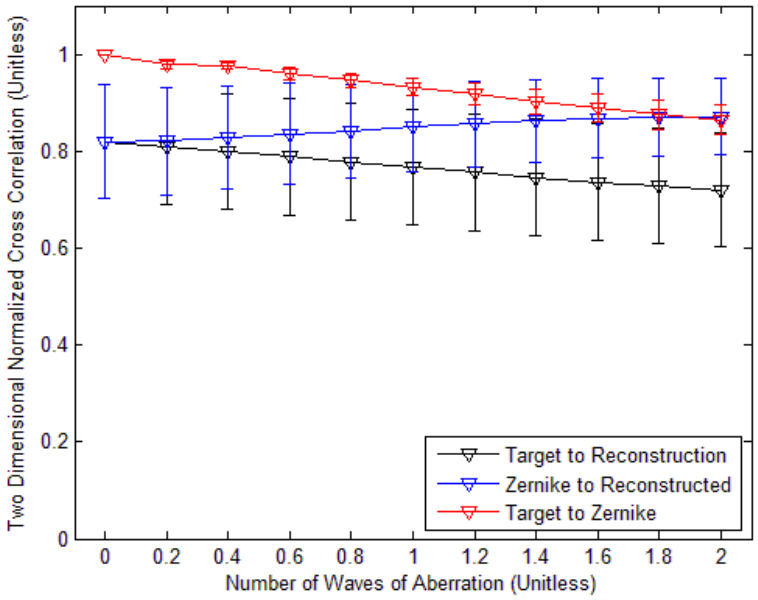

Figure 77. Optical aberration evaluation using image type letter with constant intensity, Zernike polynomial number 7.

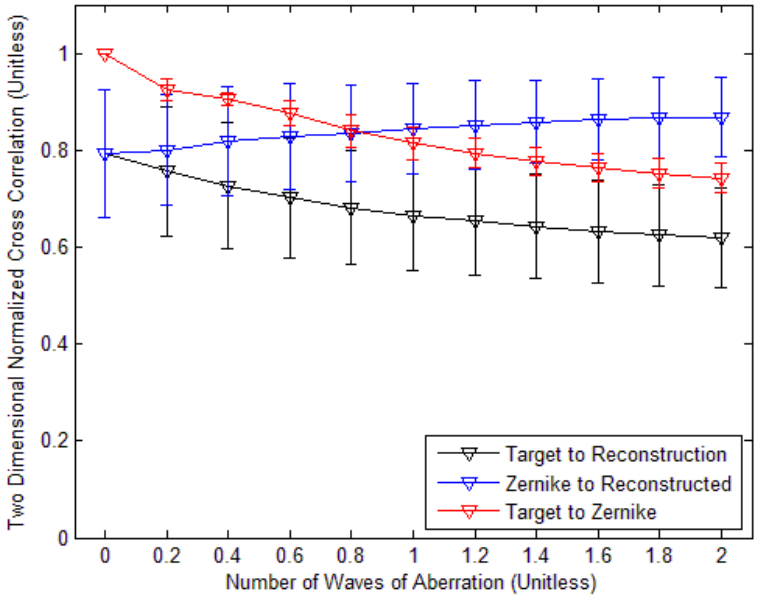

Figure 78. Optical aberration evaluation using image type letter with random intensity, Zernike polynomial number 7.

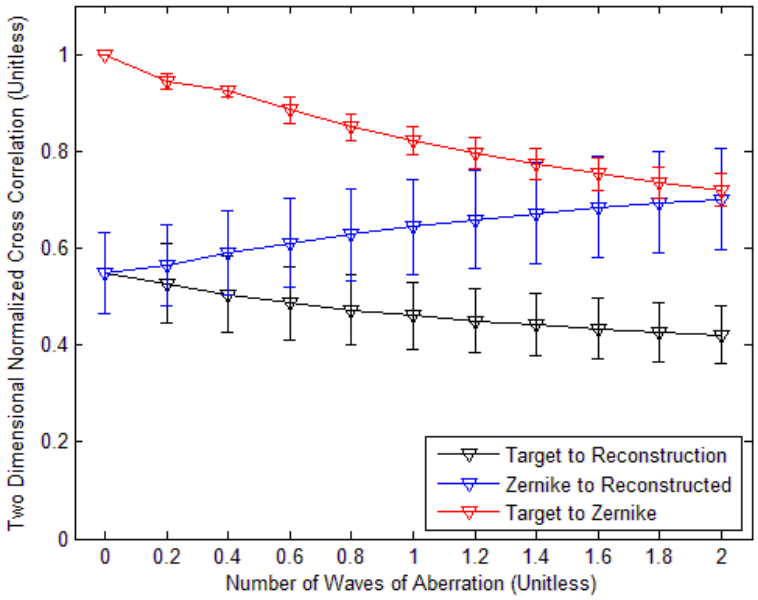

Figure 79. Optical aberration evaluation using image type backlit AF bar chart with constant intensity, Zernike polynomial number 7.

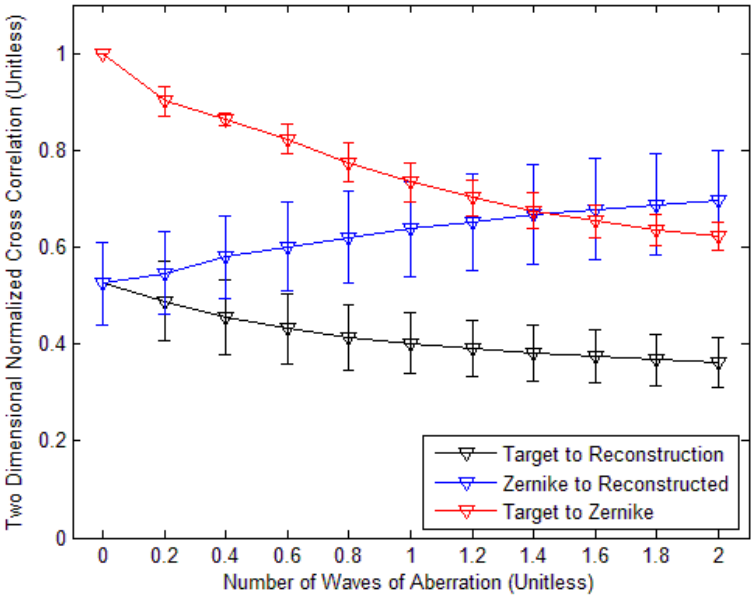

Figure 80. Optical aberration evaluation using image type backlit AF bar chart with random intensity, Zernike polynomial number 7.

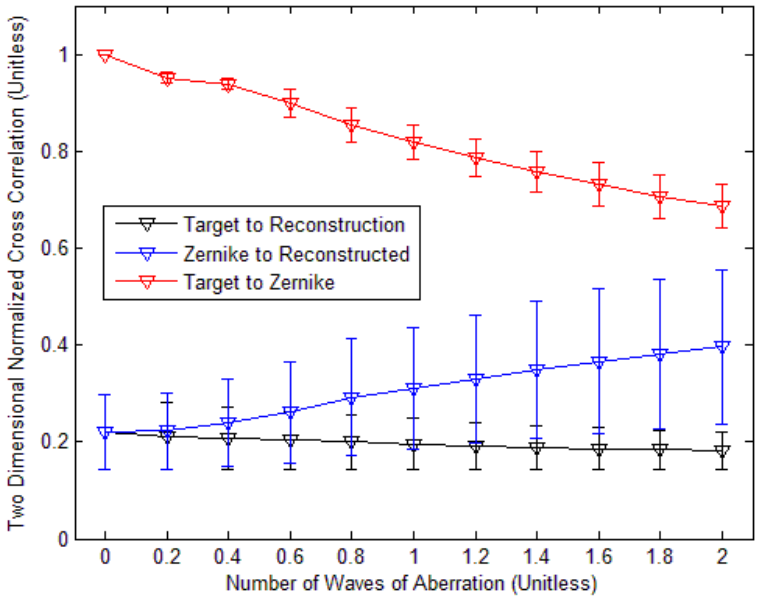

Figure 81. Optical aberration evaluation using image type front lit AF bar chart with constant intensity, Zernike polynomial number 7.

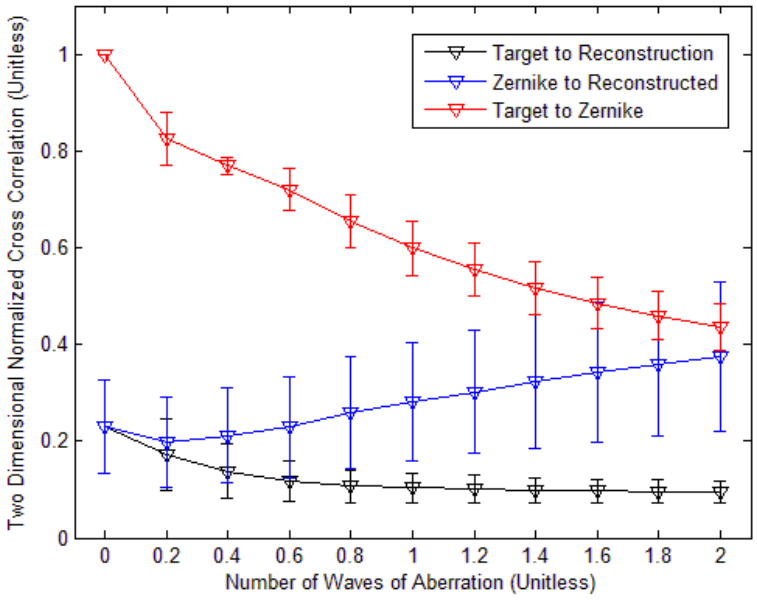

Figure 82. Optical aberration evaluation using image type front lit AF bar chart with random intensity, Zernike polynomial number 7.

4.4.4 Optical Aberration using Zernike Polynomial 9: "Spherical"

The analysis in this section will utilize Zernike polynomial number nine which closely resembles a spherical optical aberration and will be performed as described in Section 4.4. Six hypercubes will be used in the evaluation. The basic image types used are the letter, backlit AF bar chart, and front lit AF bar chart and the constant intensity and random intensities are used.

.

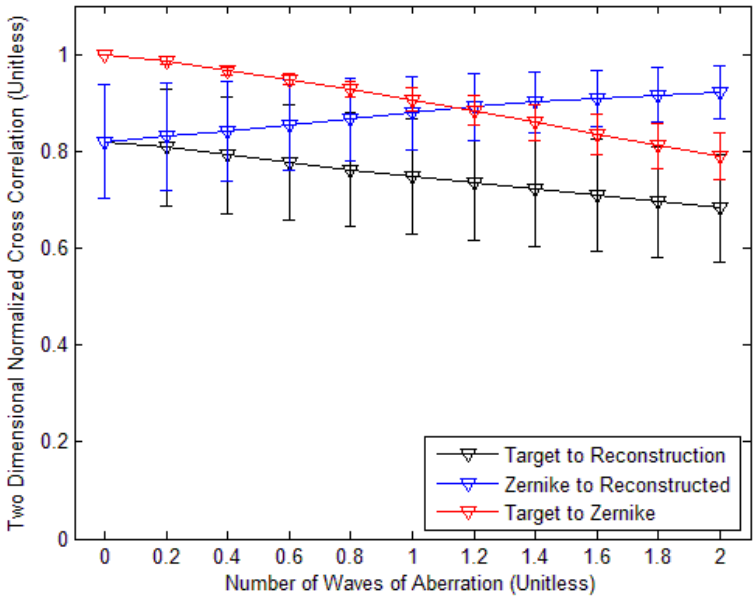

Figure 83. Optical aberration evaluation using image type letter with constant intensity, Zernike polynomial number 9.

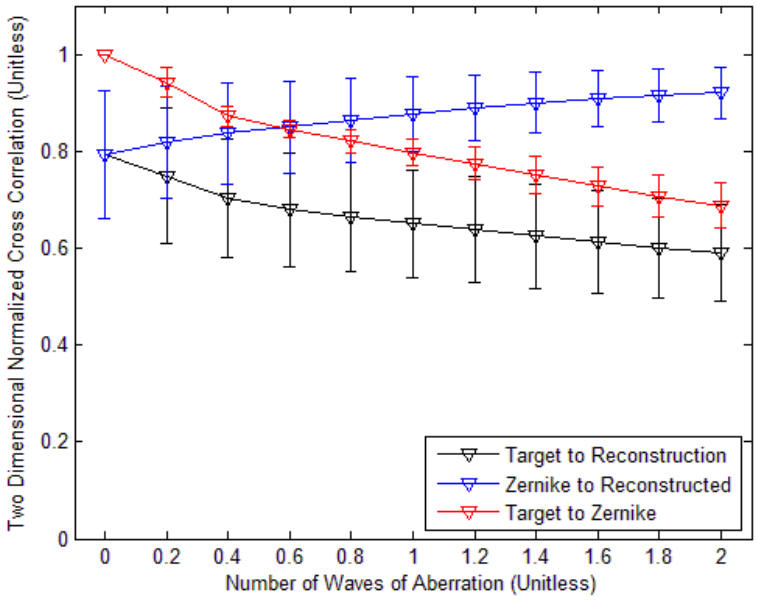

Figure 84. Optical aberration evaluation using image type letter with random intensity, Zernike polynomial number 9.

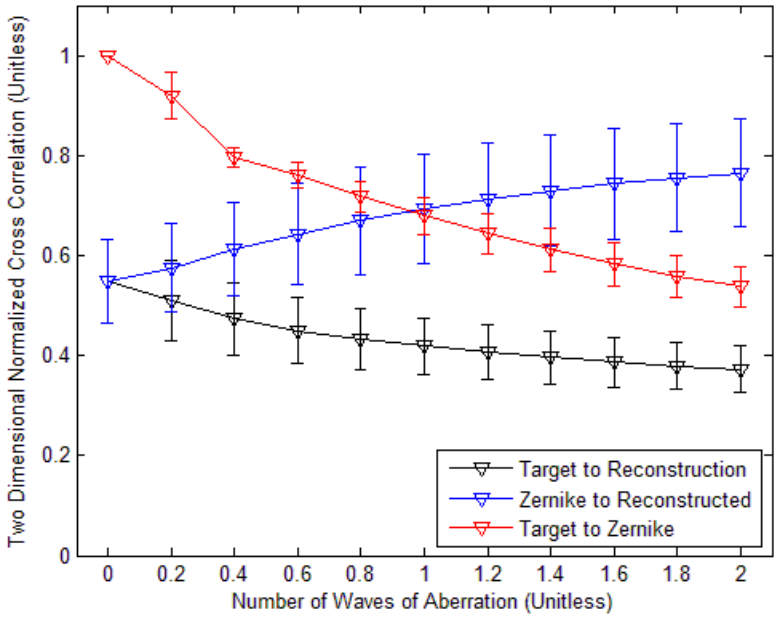

Figure 85. Optical aberration evaluation using image type backlit AF bar chart with constant intensity, Zernike polynomial number 9.

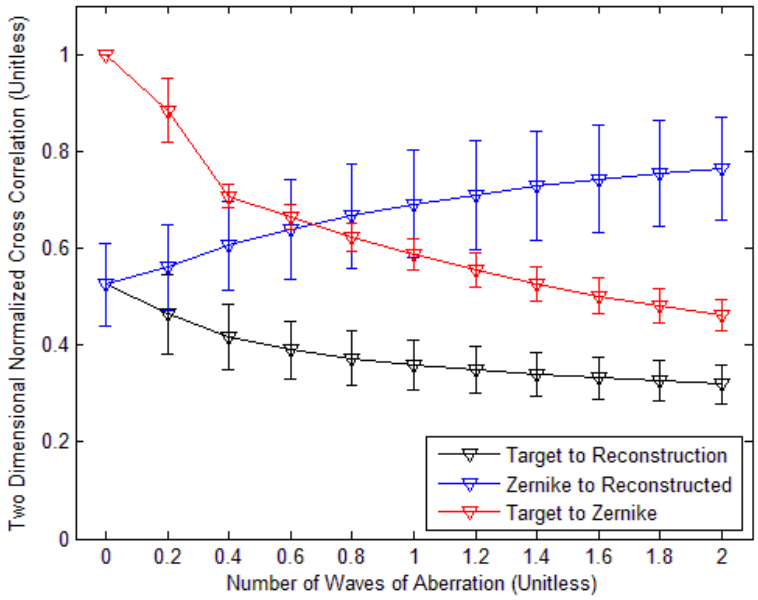

Figure 86. Optical aberration evaluation using image type backlit AF bar chart with random intensity, Zernike polynomial number 9.

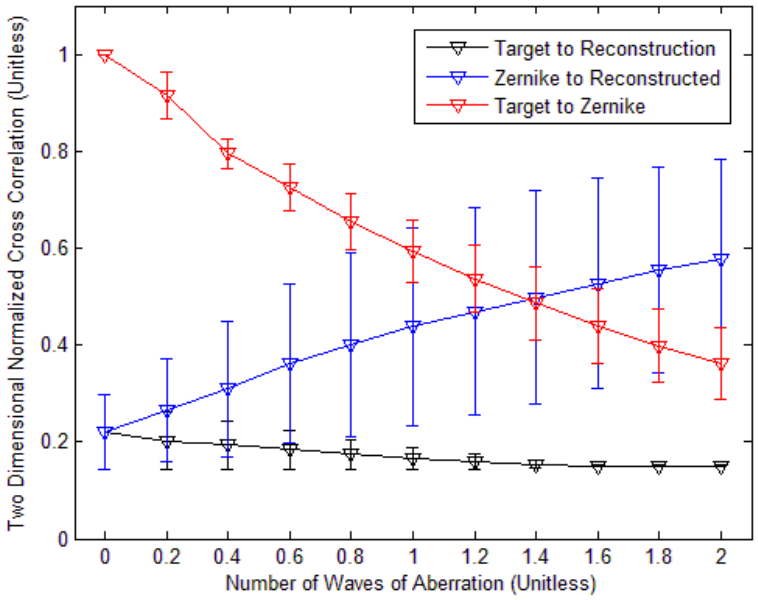

Figure 87. Optical aberration evaluation using image type front lit AF bar chart with constant intensity, Zernike polynomial number 9.

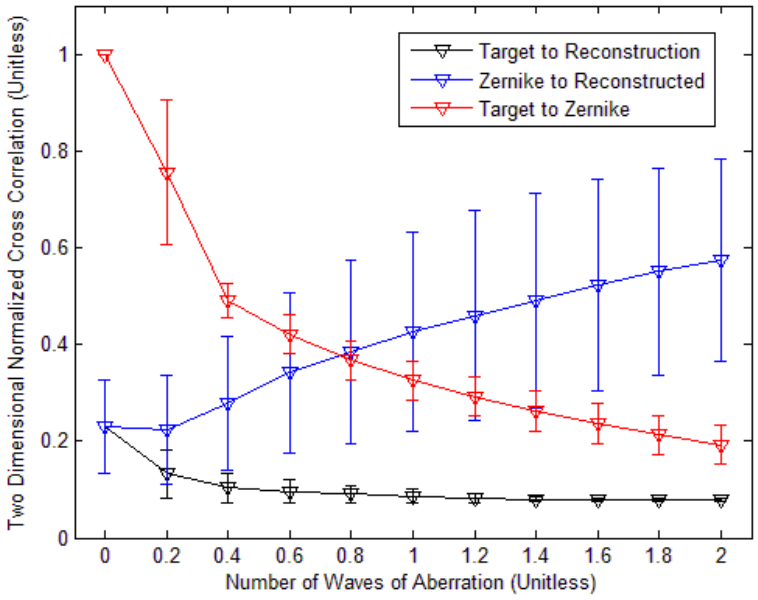

Figure 88. Optical aberration evaluation using image type front lit AF bar chart with random intensity, Zernike polynomial number 9.

4.5 Summary of Results

The range of angles used in the reconstruction is critical in the overall reconstructed image quality. In all cases the reconstruction worked best when it had captured angles over a 360 degree range. It was observed that the virtually all of the reconstructed image quality was gained in the first 20 projection which are equally spaced. It was observed that Back Projection reconstruction image quality decreased as the spatial complexity increased. Due to Back Projection's limited performance capability for the majority of the hypercubes analyzed, the new Shift and Place algorithm was developed and tested.

Shift and Place was compared against Back Projection. In 15 of the 18 hypercubes tested (83%) Shift and Place outperformed the Back Projection method provided at least 20 projections were used in the reconstruction algorithm. It was observed in some cases the reconstructed image quality actually started to decrease as additional projections were used in the reconstruction. It appears that the placement technique is extremely sensitive to any variation between shifted images. As additional projections are used the potential to incorrectly identify information also increases.

Optical aberrations in the recorded projections impact the reconstructed image quality. The trend line in the decreased image quality of the Zernike images resembled the decrease in image quality in the reconstructed image but was not identical. This means that the image quality lost in the reconstruction and the image quality lost due to optical aberrations are cumulative. The fact the slopes of the trend lines are not exact matches indicates that the impact is not additive.

V. Conclusions and Recommendations

This chapter summarizes the research conducted in this thesis. All conclusions were made based on simulated images using the proposed new prism design. Reconstructed image quality using traditional Back Projection and the new Shift and Place algorithm were compared for a variety of scenes. Reconstructed image quality is highly dependent on the initial target hypercube so a total of 54 initial target hypercubes were constructed with varying degrees of spatial and spectral complexity.

5.1 Optical Model, Simulation, Reconstruction, and Analysis Tools

MATLAB and Zemax work very well together. The MATLAB tools played a crucial role in allowing all of the data to be processed, stored, and analyzed effectively. The storage principles have successful allowed over 200 GB of information to be processed and stored, ready for additional testing or evaluations. The MATLAB tools were built to be highly modular to allow their function to be increased or changed by future researchers.

5.2 Angle Selection and Range

The angle range plays a major role in the ability to reconstruct images using projections. In all cases using a full range of prism angles between 360 degrees provided the best reconstructed image quality. The vast majority of the image quality gains were made in the first 20 projections.

5.3 Back Projection and Shift and Place Reconstruction

Back Projection's method of improving the reconstructed image quality by utilizing additional projections is insufficient in most applications. Since the major gains in the image reconstruction occur in the first 20 projections, a new method will be required to enable CTEx improve the image quality. The Shift and Place reconstruction algorithm demonstrated its potential in increasing the reconstructed image quality. Other more complex algorithms exist like Projection onto Convex Sets [1] that may prove to have more capability.

5.4 Optical Aberrations and Reconstructed Image Quality

Optical aberrations impact the reconstructed image quality. The decreases in image quality from the reconstruction process and from the optical aberrations are cumulative and appear to be nearly additive. A combination of optical aberrations should be investigated to see if similar trends are observed.

5.5 Recommendations

A wealth of simulation, reconstruction, and analysis data is ready for further investigation. The tools worked extremely well and with the right hardware can effectively process a great deal of information in a short period of time. During the course of this work a two member team was established in which one member worked on CTEx experimentally and the other worked on the simulation. This was highly effective partnership which should replicated in future research as it appeared to be a force multiplier.

Between the reconstruction process and optical aberrations, the greatest limiting factor in chromotomography appears to be in the reconstruction process. Back Projection only works well with relatively simple targets. More advanced algorithms should be explored with an emphasis of systematically removing artifacts from off wavelength images and filling in the cone of missing information. It appears an iterative, potentially recursive, algorithm is the likely solution. Shift and Place in principle has the right idea, but there are likely better ways in determining where to place the information.

The new prism design should be further explored and a detailed analysis of the current and proposed prism design performance should be completed. It is believed the new design will outperform the current design but it is unclear by how much. Those results could be the basis of the of cost benefit analysis to determine if the current CTEx prism should be replaced.

An extremely powerful computer should be purchased for the simulation and reconstruction process. The computer ideally will have solid state drives, a minimum of 128 GB of RAM memory, and mu1ti-core Xeon processor. Only a fraction of the simulations could have been completed using a standard AFIT machine as the calculations required are significant.

Appendix A

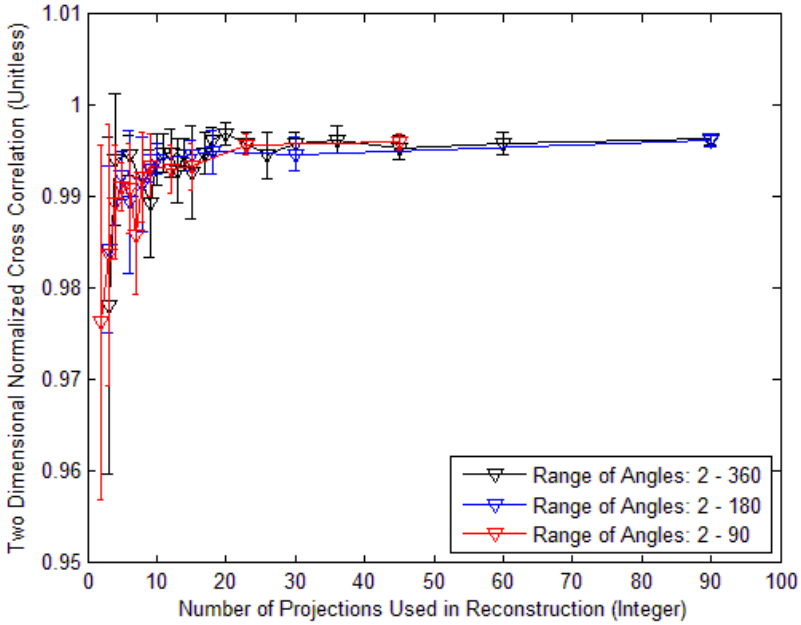

Figure 89. Reconstructed image quality of monochromatic point-like source with constant intensity.

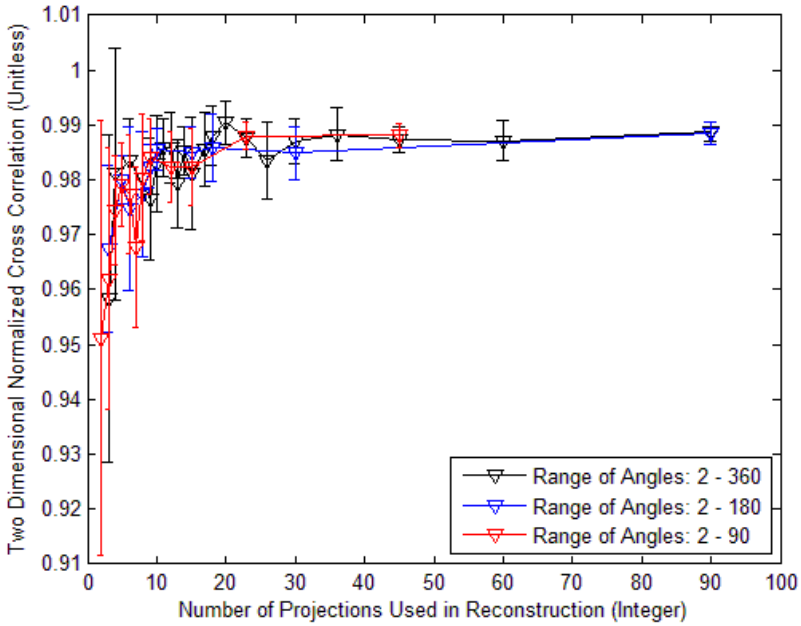

Figure 90. Reconstructed image quality of monochromatic point-like source with random intensity.

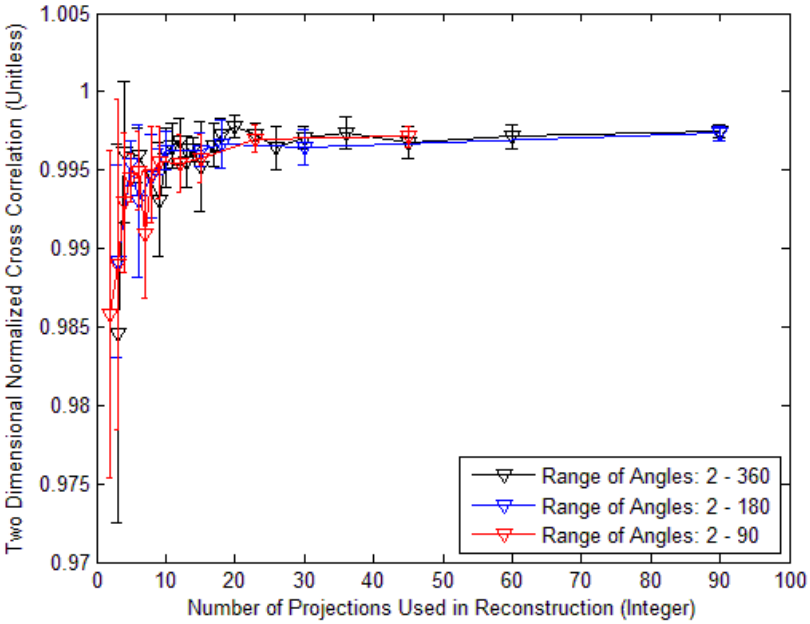

Figure 91: Reconstructed image quality of monochromatic letter with constant intensity.

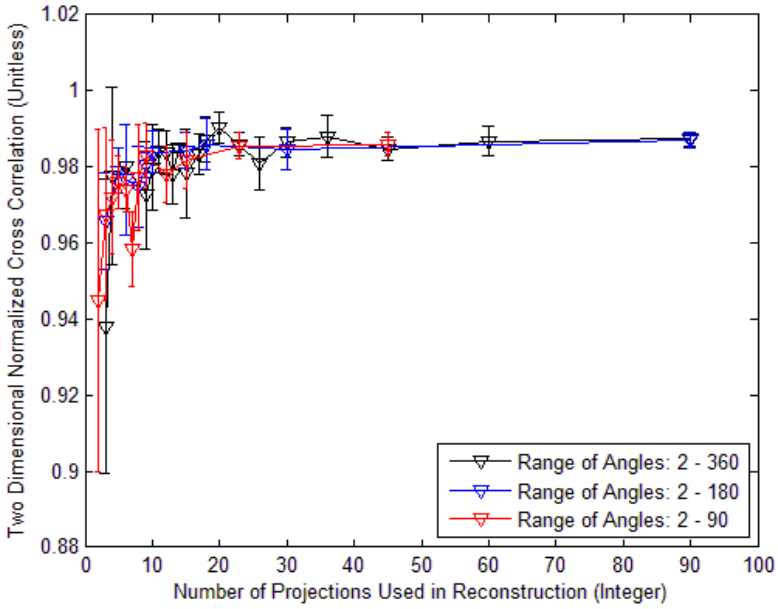

Figure 92. Reconstructed image quality of monochromatic letter with random intensity.

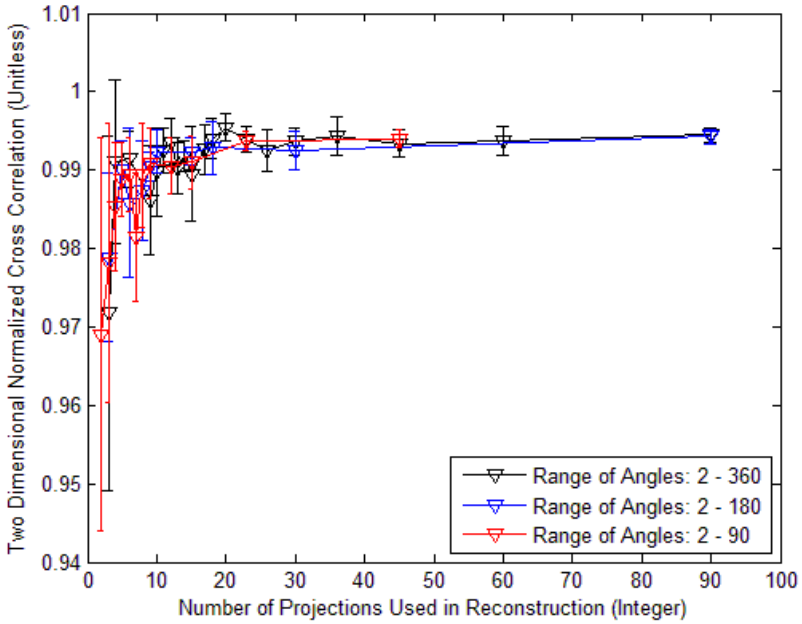

Figure 93. Reconstructed image quality of monochromatic backlit bar chart with constant intensity.

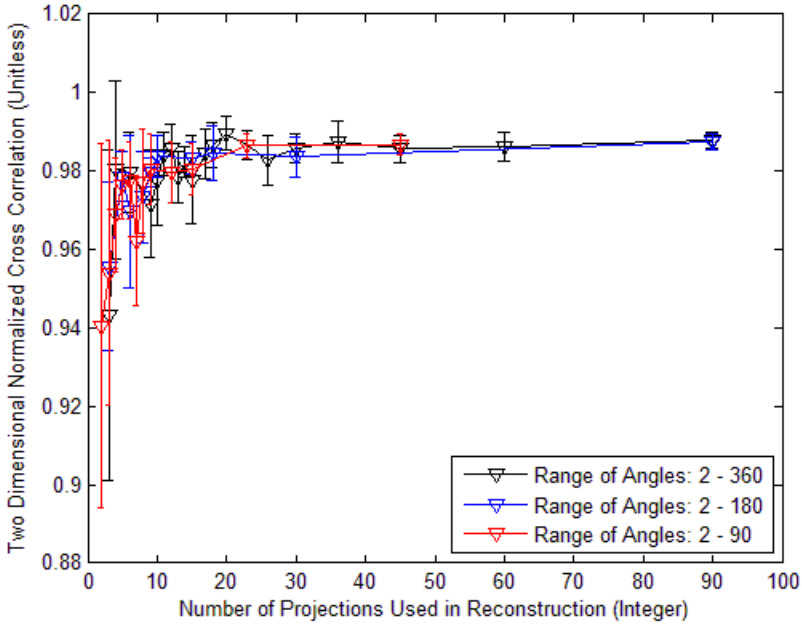

Figure 94. Reconstructed image quality of monochromatic backlit bar chart with random intensity.

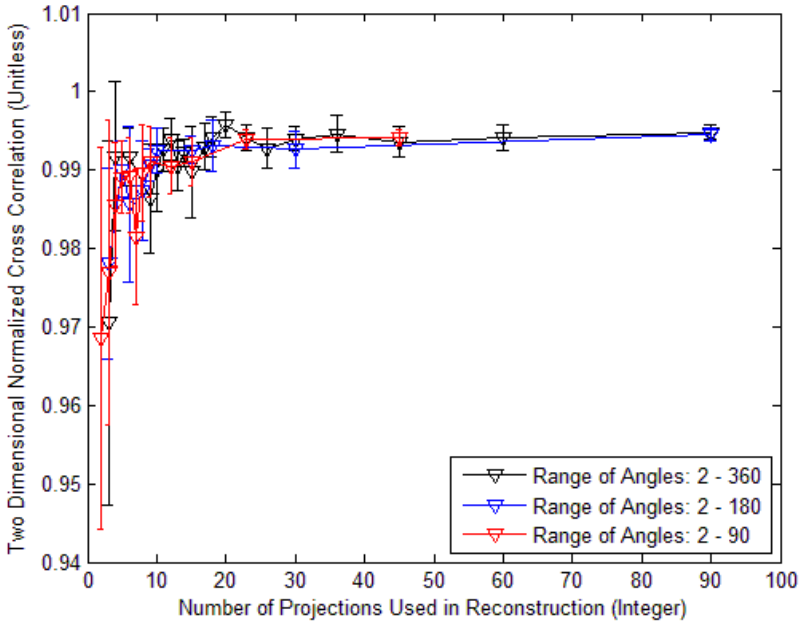

Figure 95. Reconstructed image quality of monochromatic front lit bar chart with constant intensity.

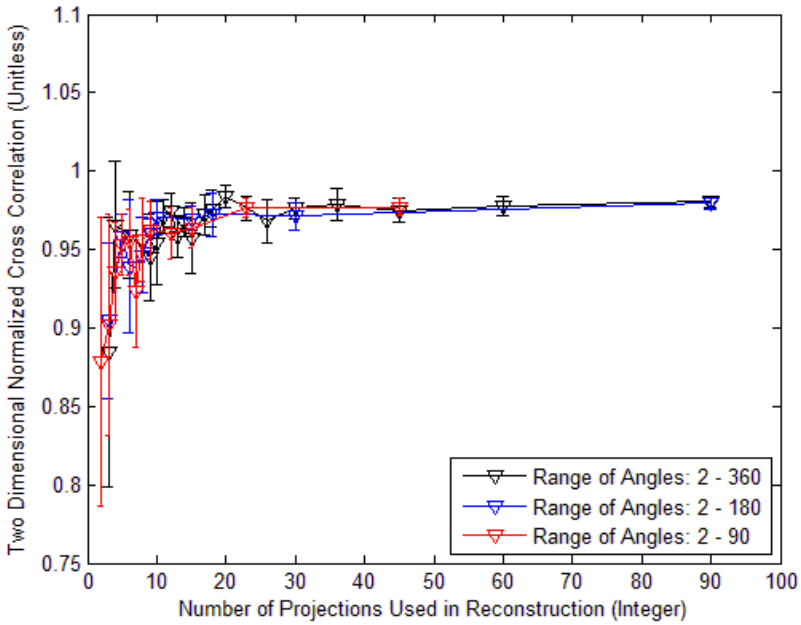

Figure 96: Reconstructed image quality of monochromatic front lit bar chart with random intensity

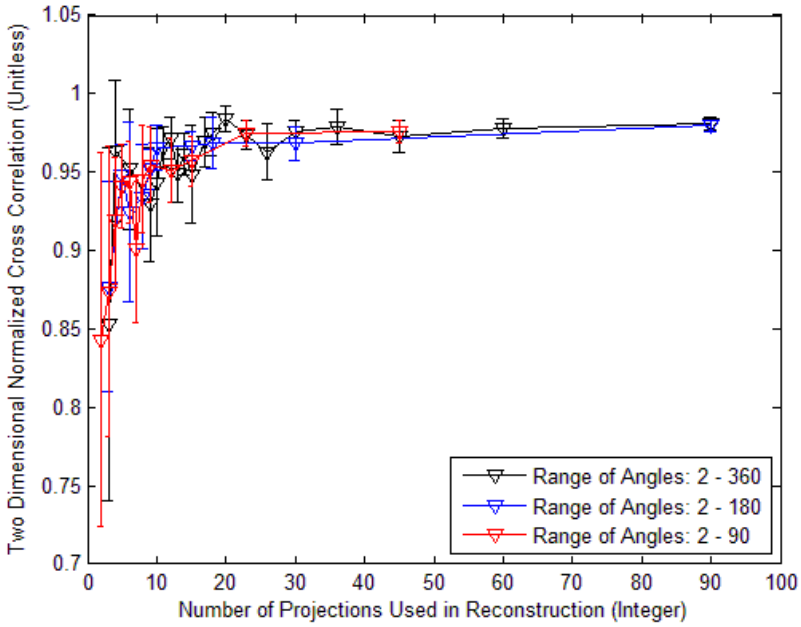

Figure 97. Reconstructed image quality of monochromatic random intensity 400x400 pixel image.

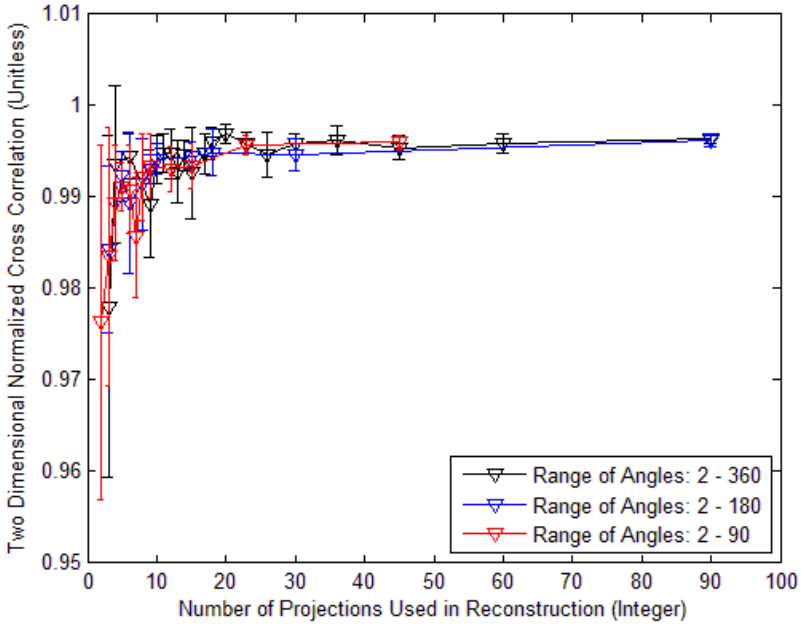

Figure 98. Reconstructed image quality of point like source with constant intensity, 100 nm separation.

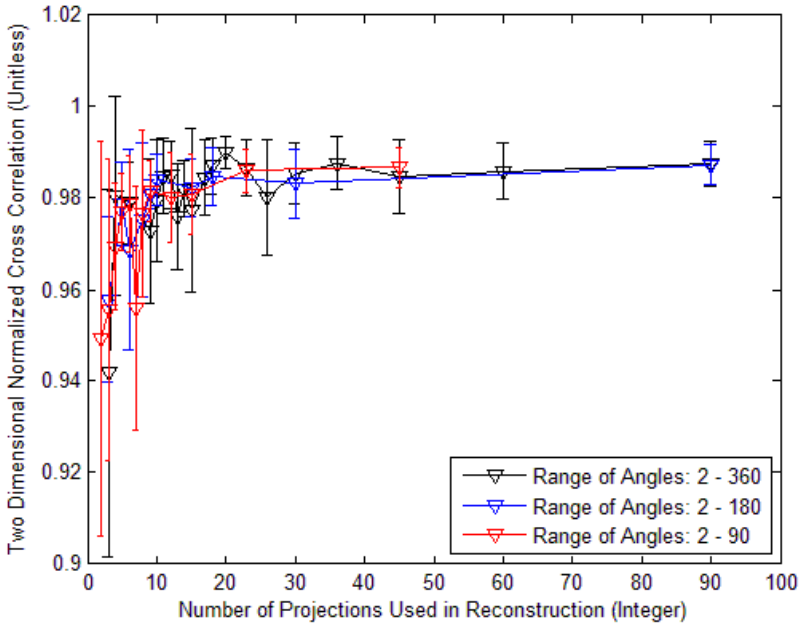

Figure 99: Reconstructed image quality of point like source with random intensity, 100 nm separation.

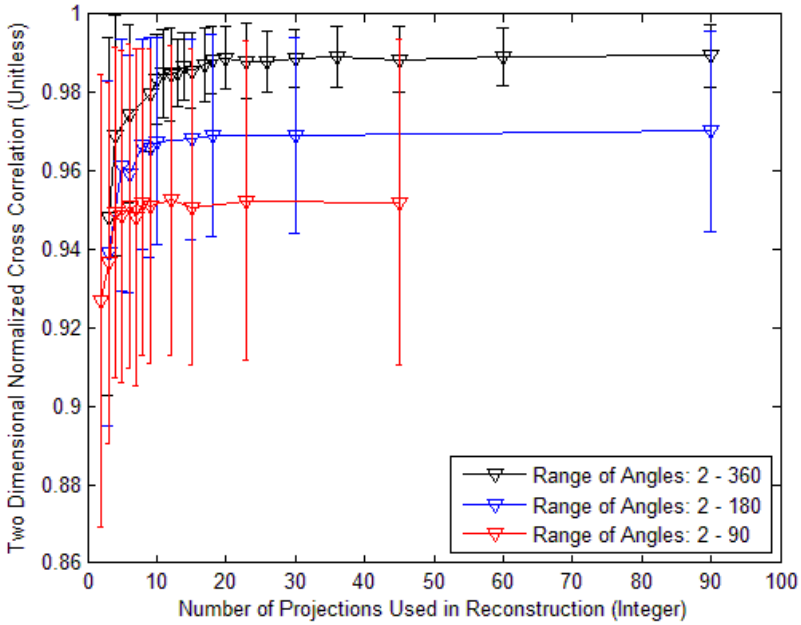

Figure 100. Reconstructed image quality of letter with constant intensity, 100nm separation.

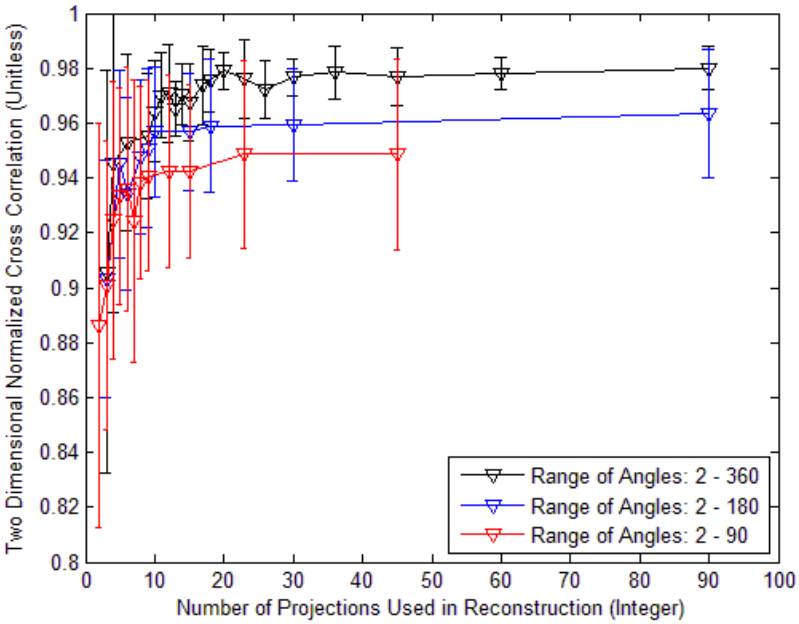

Figure 101. Reconstructed image quality of letter with random intensity, 100 nm separation.

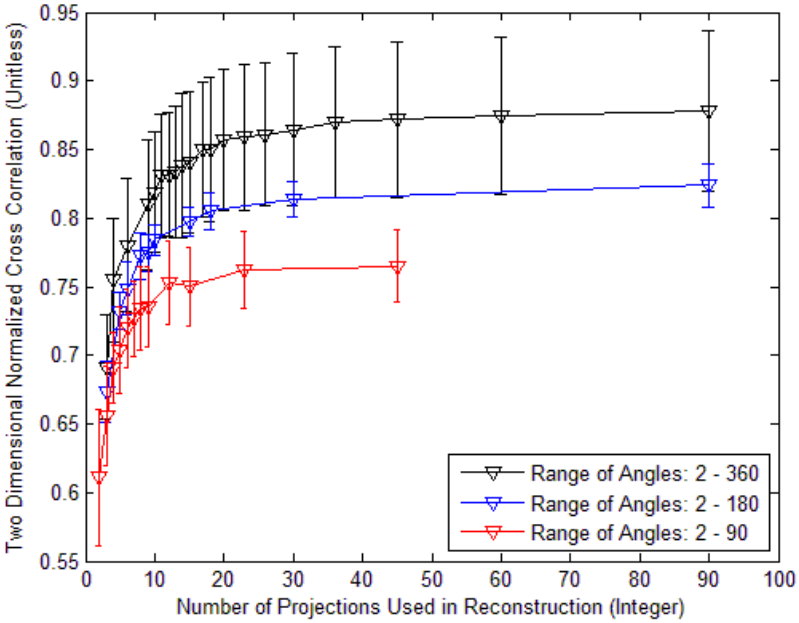

Figure 102. Reconstructed image quality of backlit bar chart with constant intensity, 100 nm separation.

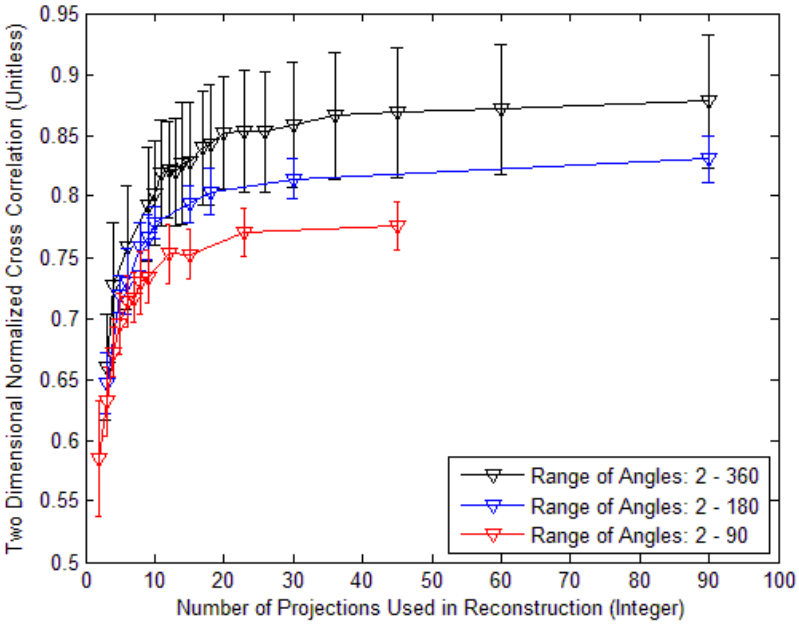

Figure 103. Reconstructed image quality of backlit bar chart with random intensity, 100 nm separation.

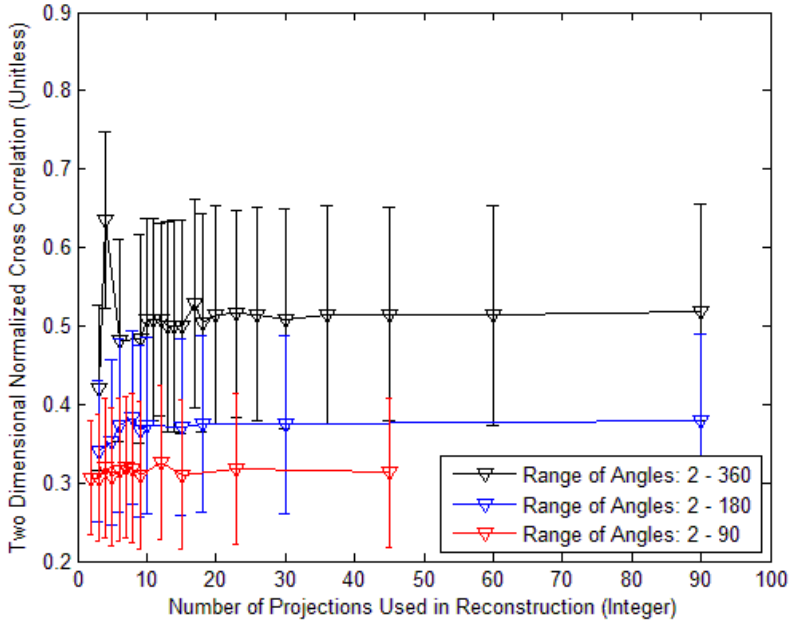

Figure 104. Reconstructed image quality of front lit bar chart with constant intensity, 100 nm separation.

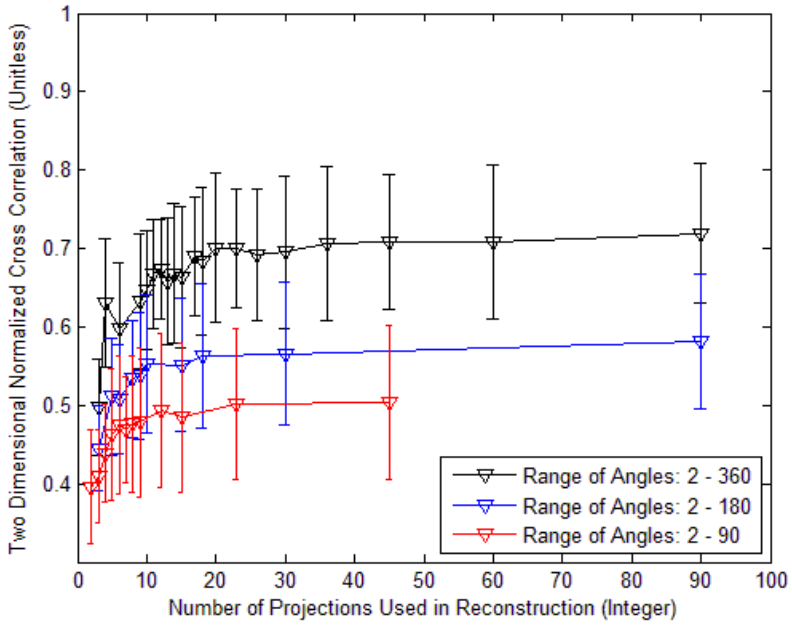

Figure 105. Reconstructed image quality of front lit bar chart with random intensity, 100 nm separation.

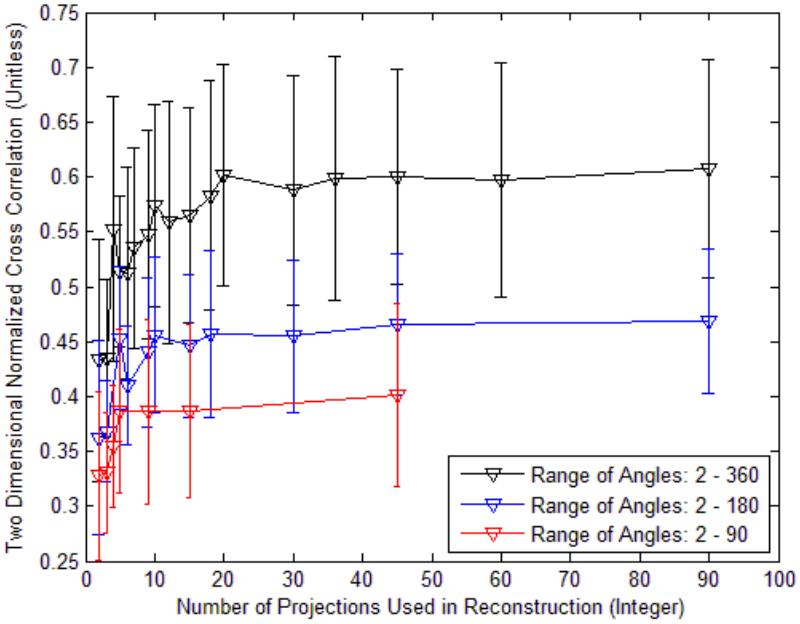

Figure 106 Reconstructed image quality of random 400x400 pixel, 100 nm separation.

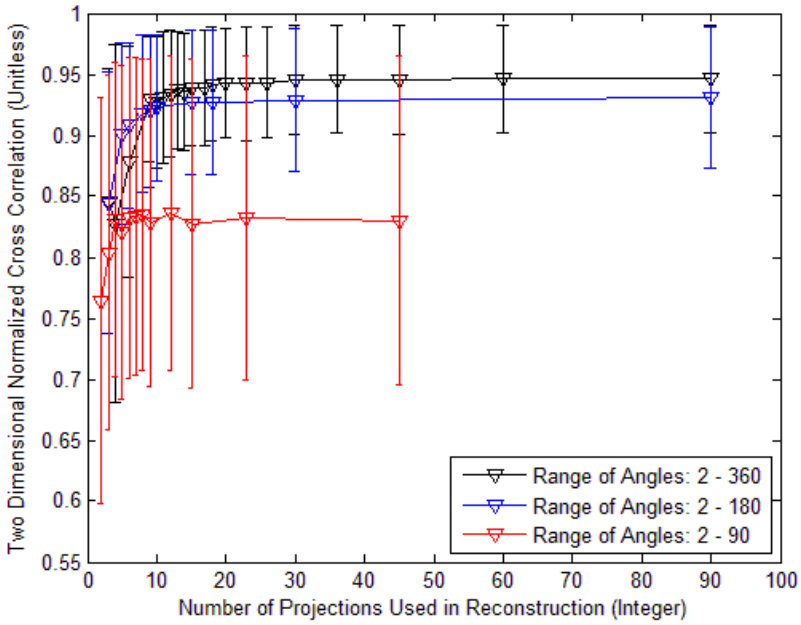

Figure 107. Reconstructed image quality of point-like source with constant intensity, 20 nm separation.

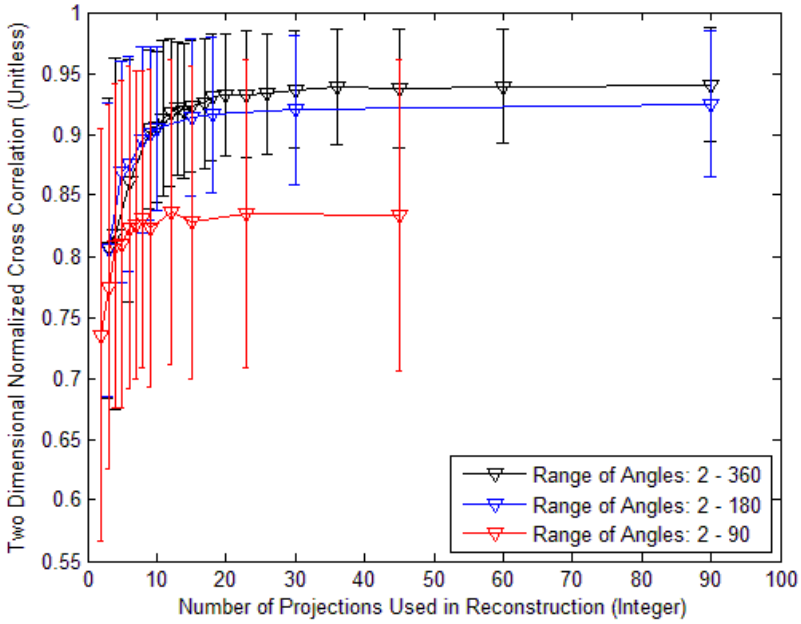

Figure 108. Reconstructed image quality of point-like source with random intensity, 20 nm separation.

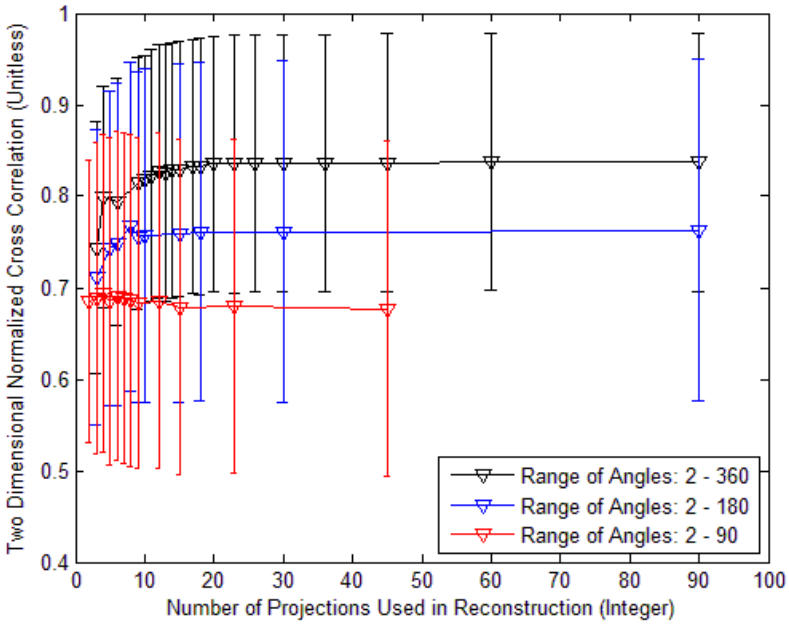

Figure 109. Reconstructed image quality of letter with constant intensity, 20 nm separation.

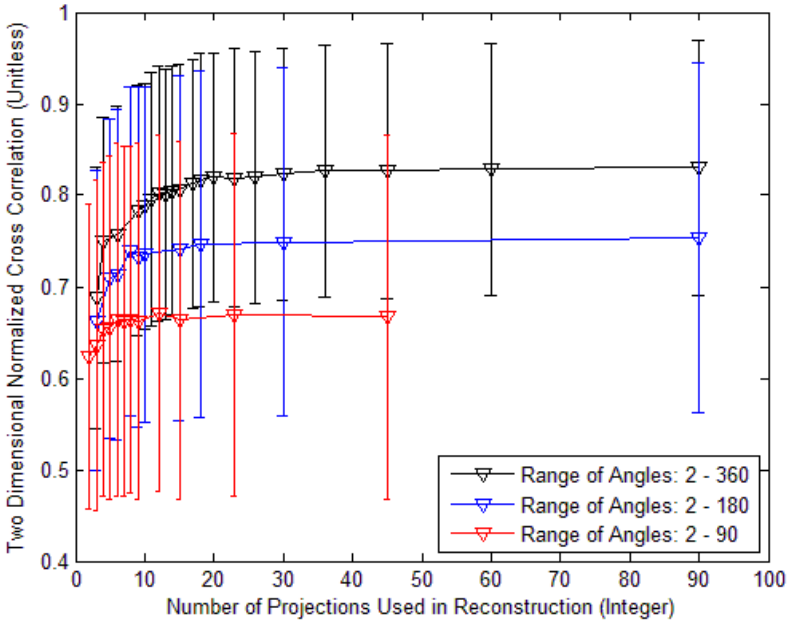

Figure 110. Reconstructed image quality of letter with random intensity, 20 nm separation.

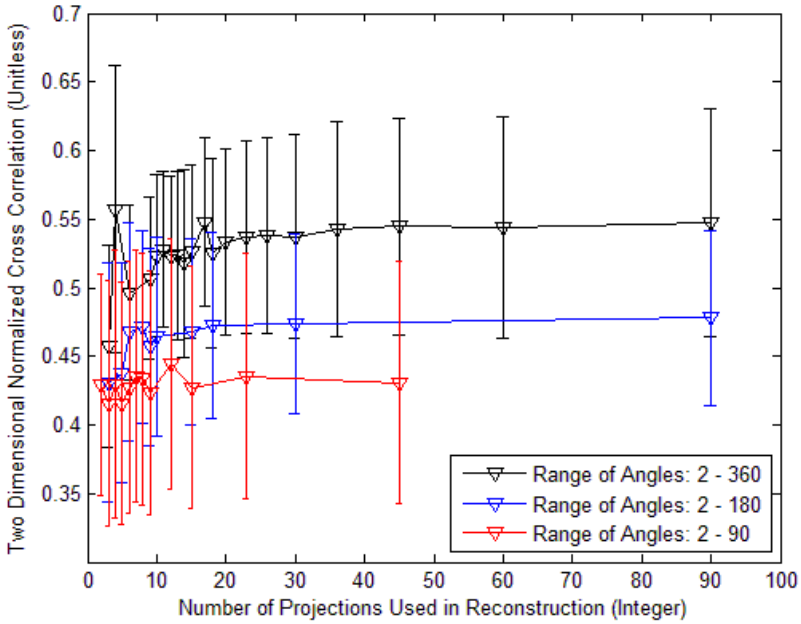

Figure 111. Reconstructed image quality of backlit AF bar chart with constant intensity, 20 nm separation.

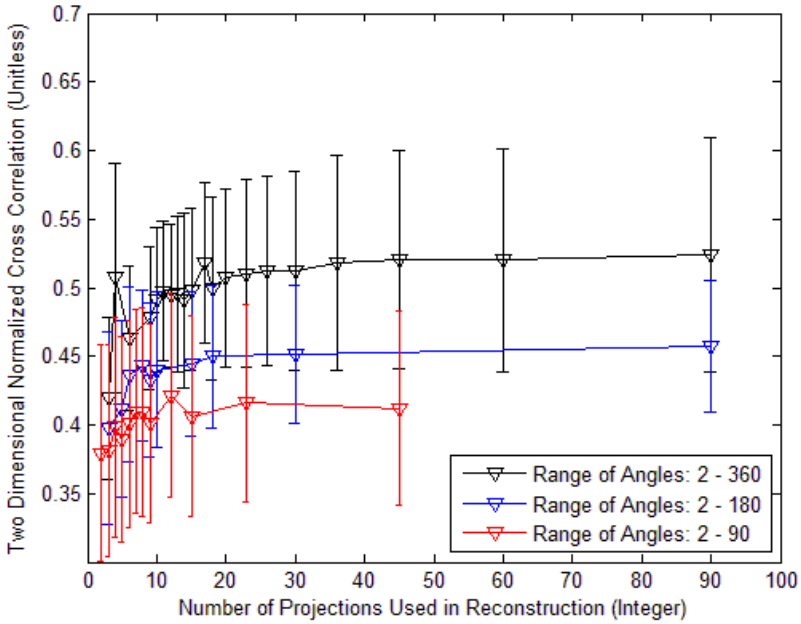

Figure 112. Reconstructed image quality of backlit AF bar chart with random intensity, 20 nm separation

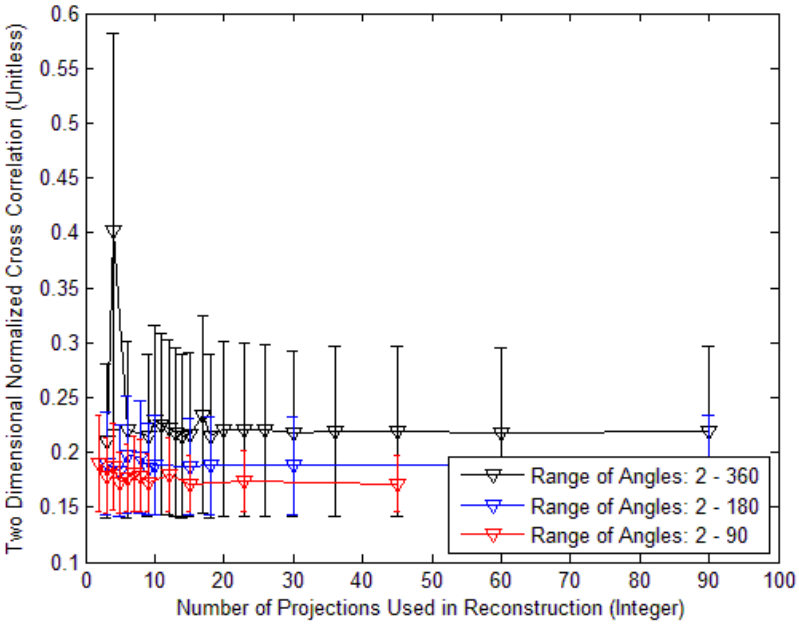

Figure 21. Reconstructed image quality of front lit AF bar chart with constant intensity, 20 nm separation.

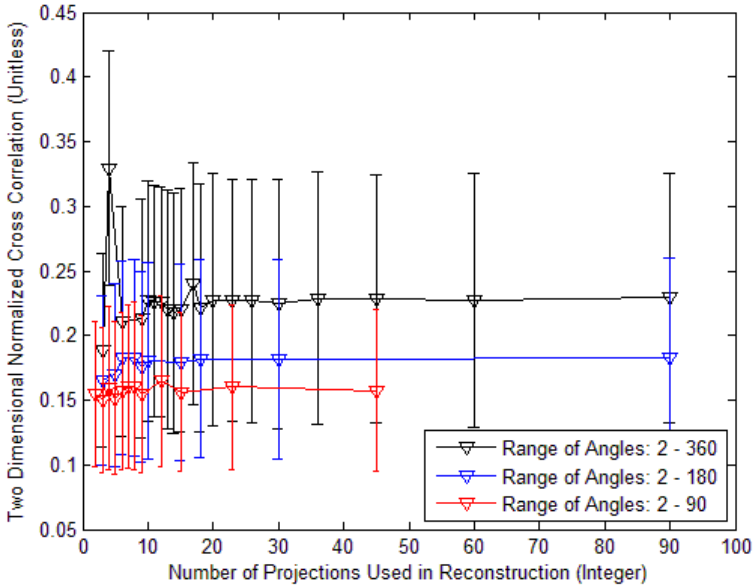

Figure 113. Reconstructed image quality of front lit AF bar chart with random intensity, 20 nm separation.

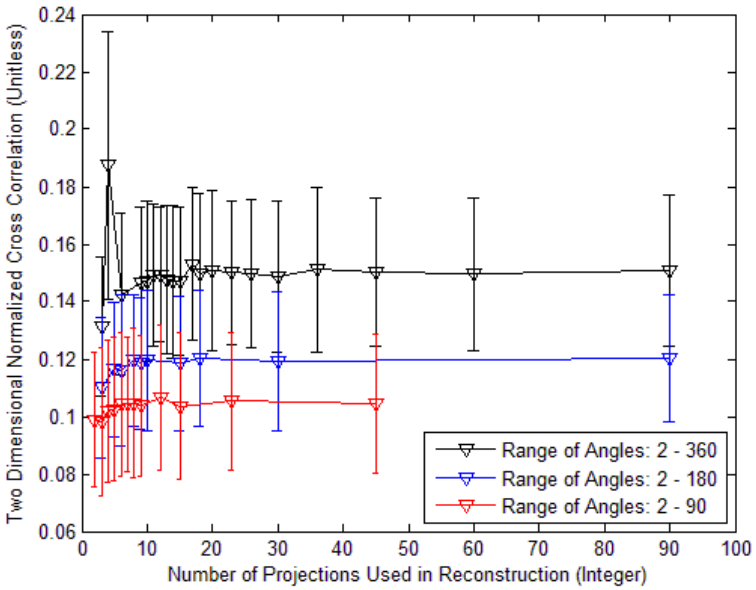

Figure 114. Reconstructed image quality of random intensity 400x400 pixels with 20 nm separation.

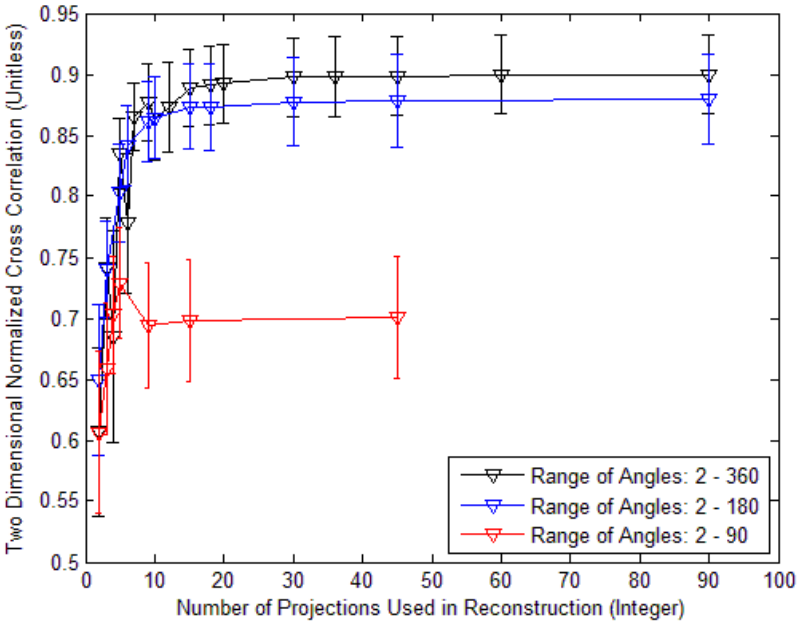

Figure 115. Reconstructed image quality of point like source with constant intensity, 10 nm separation

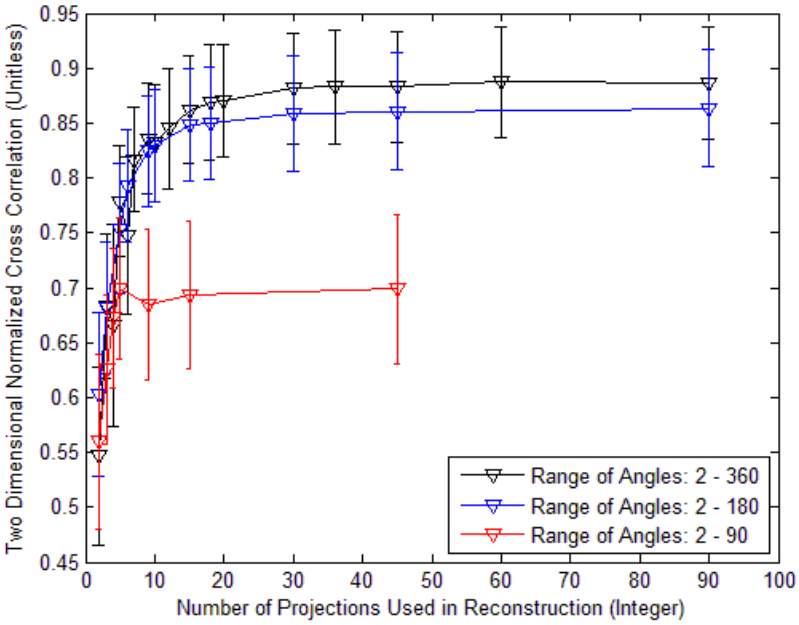

Figure 116. Reconstructed image quality of point like source with random intensity, 10 nm separation

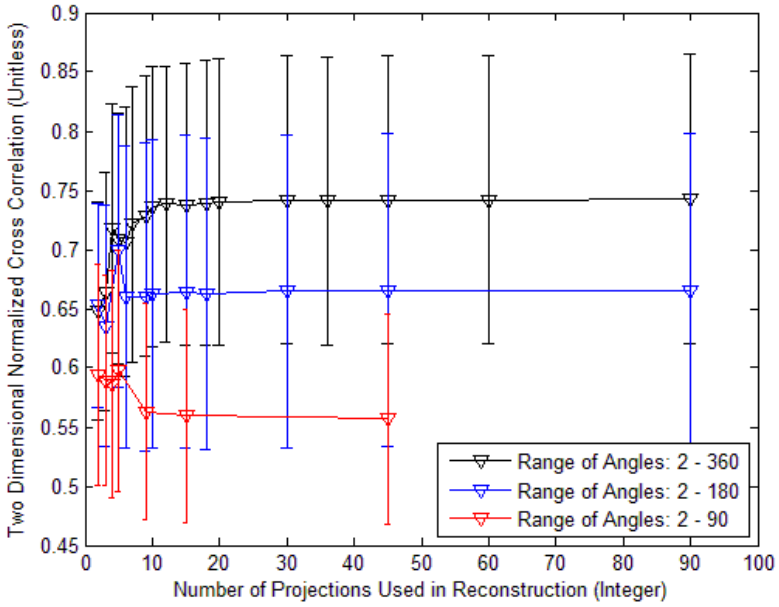

Figure 117. Reconstructed image quality of letter with constant intensity, 10 nm separation

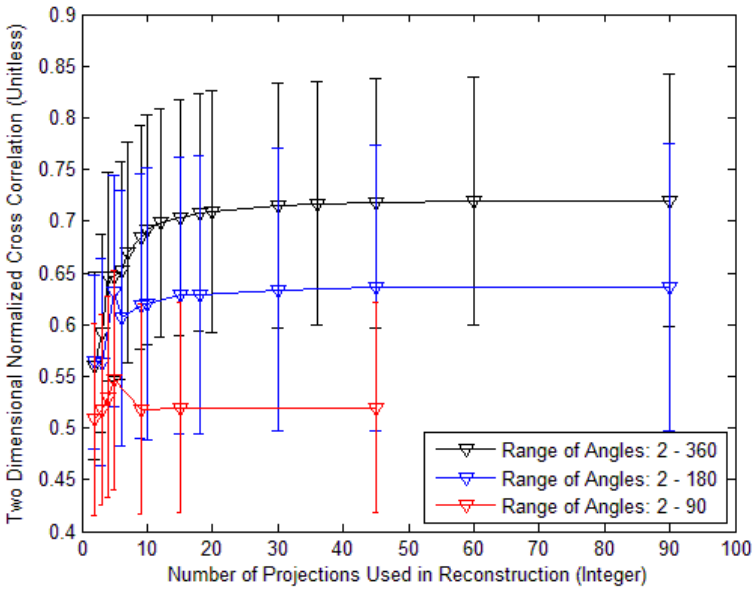

Figure 118. Reconstructed image quality of letter with random intensity, 10 nm separation

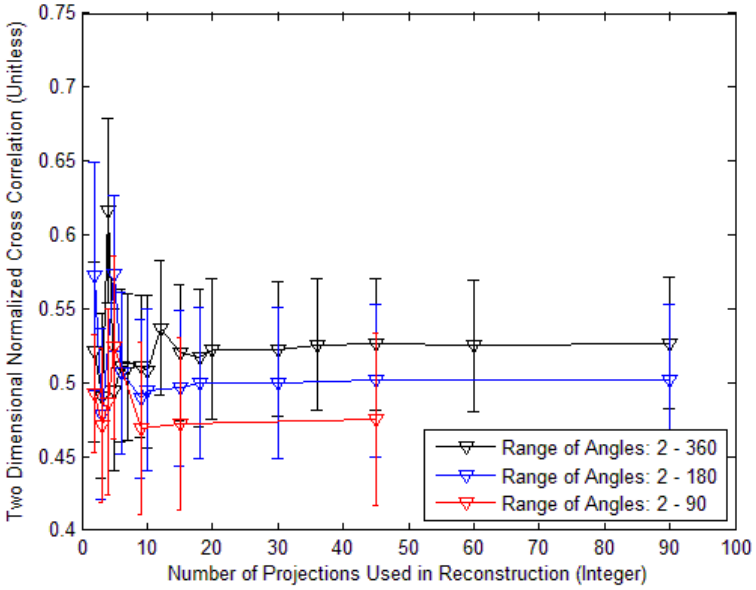

Figure 119. Reconstructed image quality of backlit AF bar chart with constant intensity, 10 nm separation

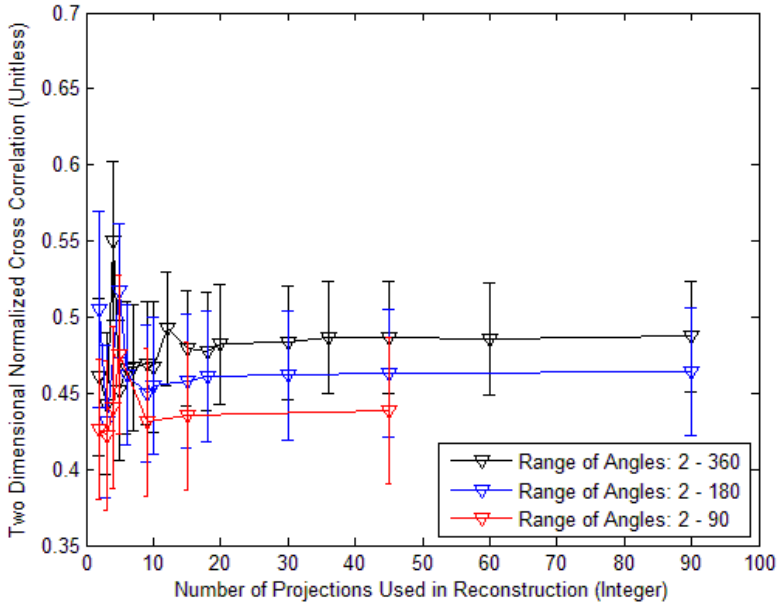

Figure 120. Reconstructed image quality of backlit AF Bar chart with random intensity, 10 nm separation

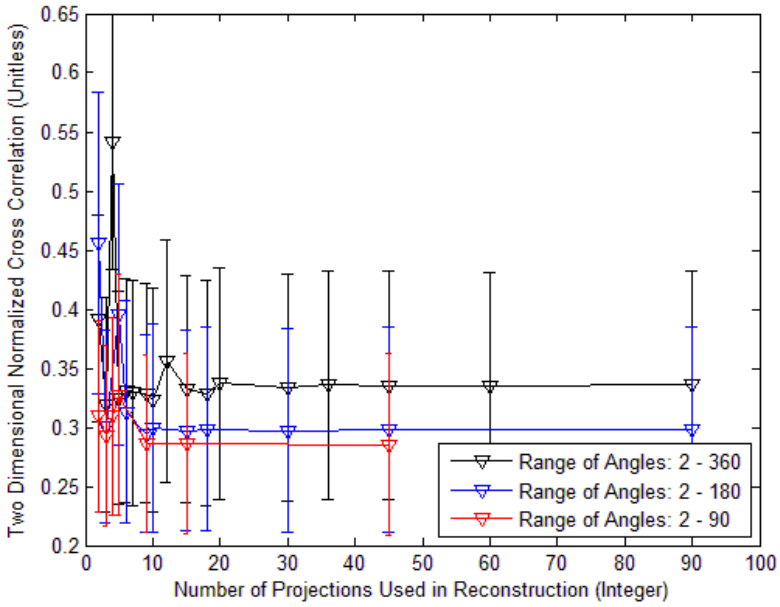

Figure 121. Reconstructed image quality of front lit AF bar chart with constant intensity, 10 nm separation

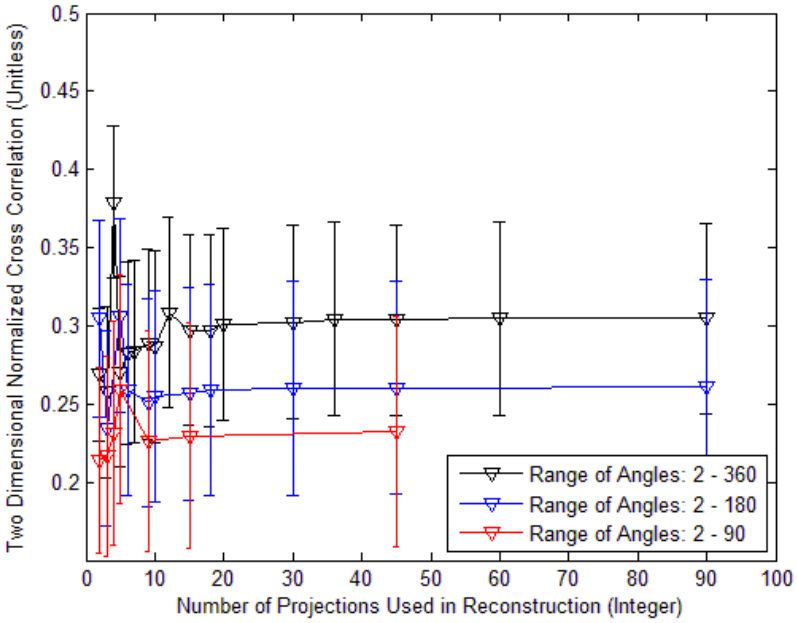

Figure 122. Reconstructed image quality of front lit AF bar chart with random intensity, 10 nm separation

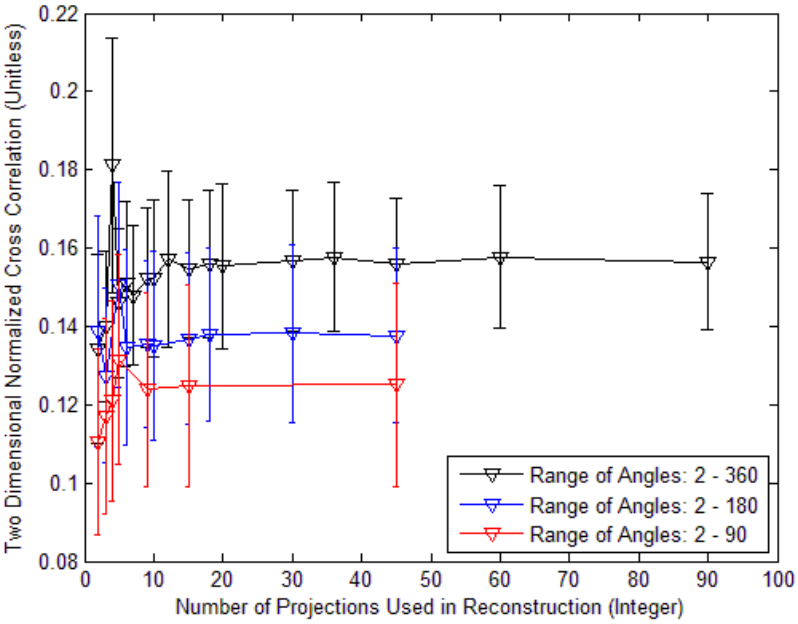

Figure 123. Reconstructed image quality of random intensity 400x400 pixel, 10 nm separation

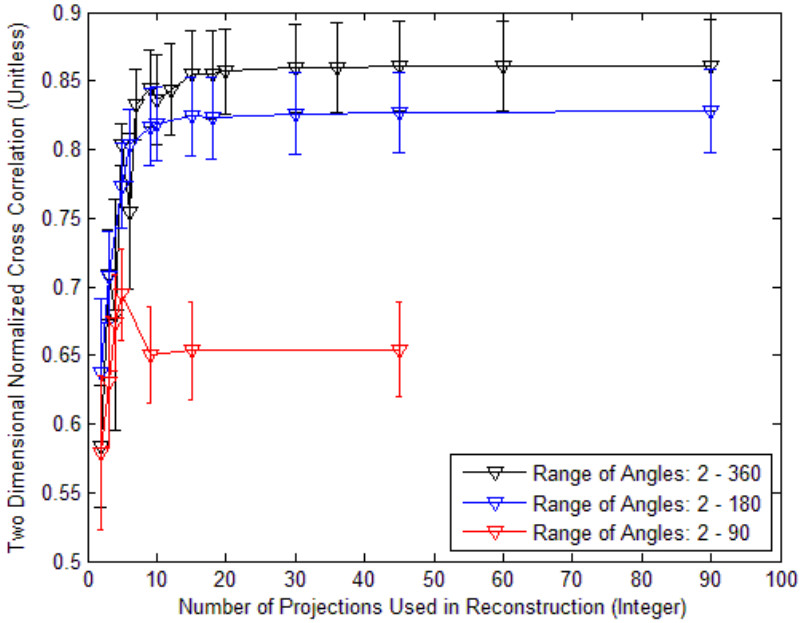

Figure 124. Reconstructed image quality of point like source with constant intensity, 5 nm separation

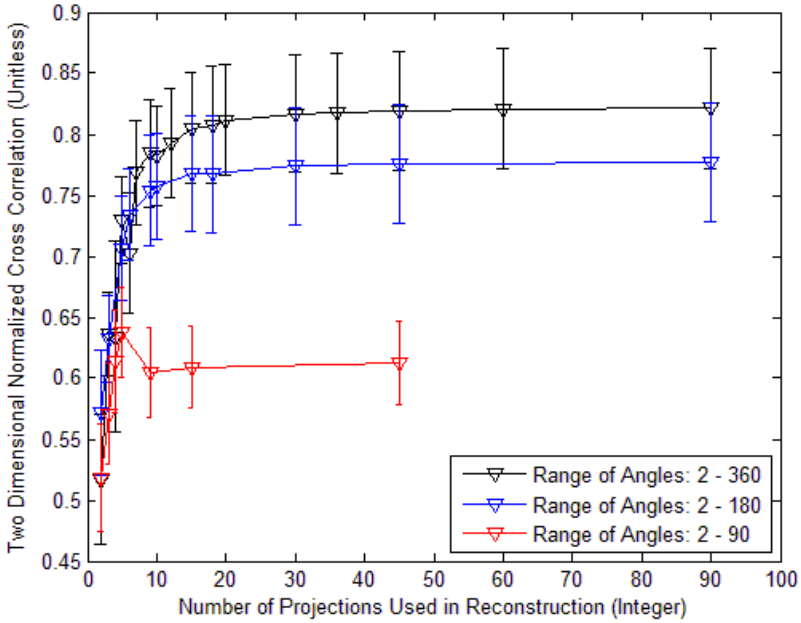

Figure 125. Reconstructed image quality of point like source with random intensity, 5 nm separation

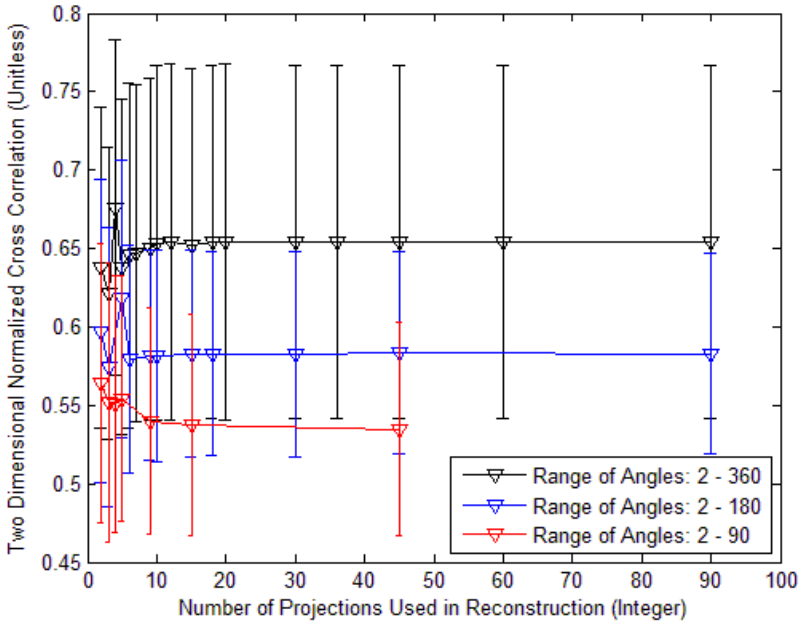

Figure 126. Reconstructed image quality of letter with constant intensity, 5 nm separation

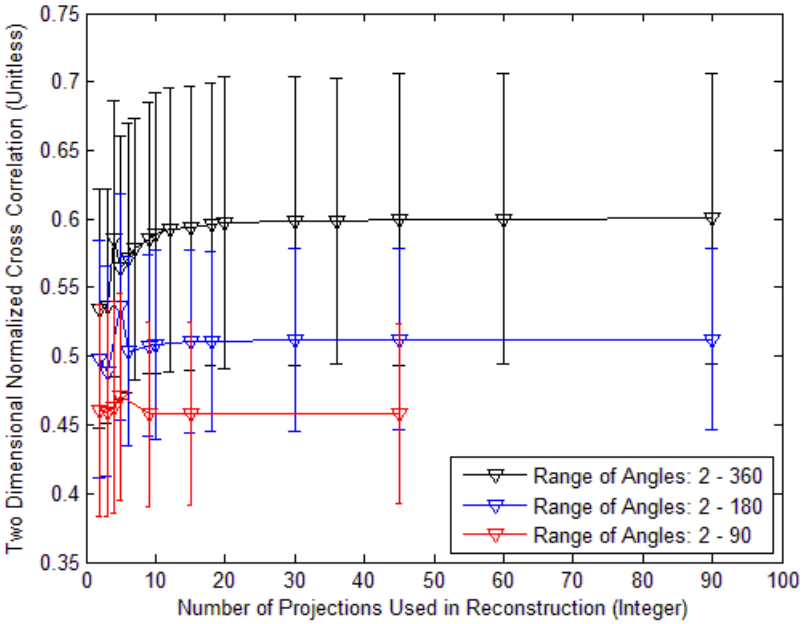

Figure 127. Reconstructed image quality of letter with random intensity, 5 nm separation

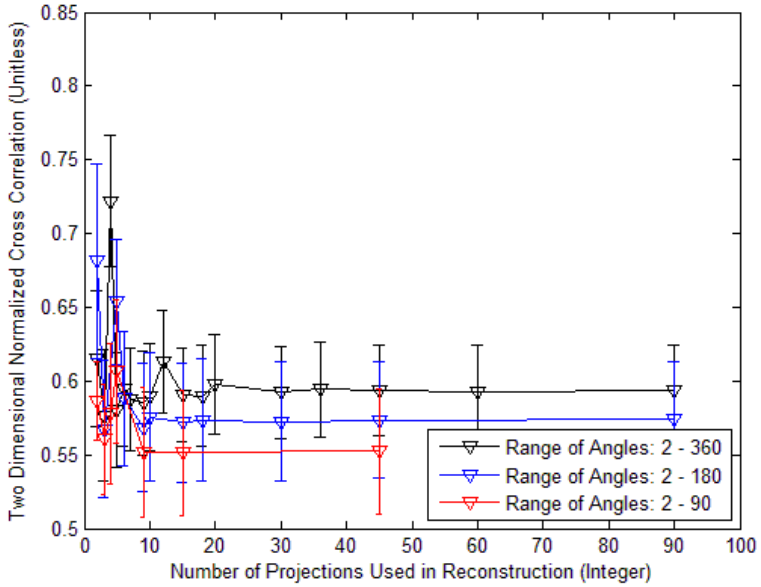

Figure 128. Reconstructed image quality of backlit AF bar chart with constant intensity, 5 nm separation

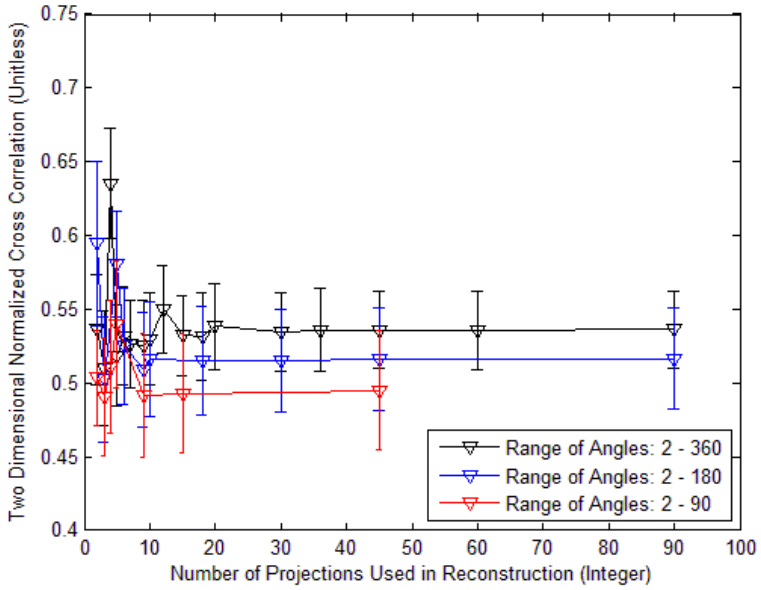

Figure 129. Reconstructed image quality of backlit AF bar chart with random intensity, 5 nm separation

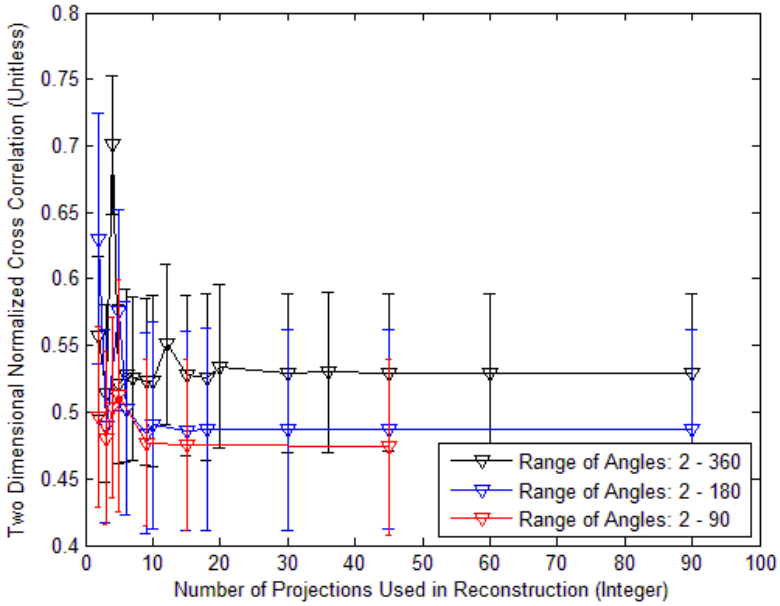

Figure 130. Reconstructed image quality of front lit AF bar chart with constant intensity, 5 nm separation

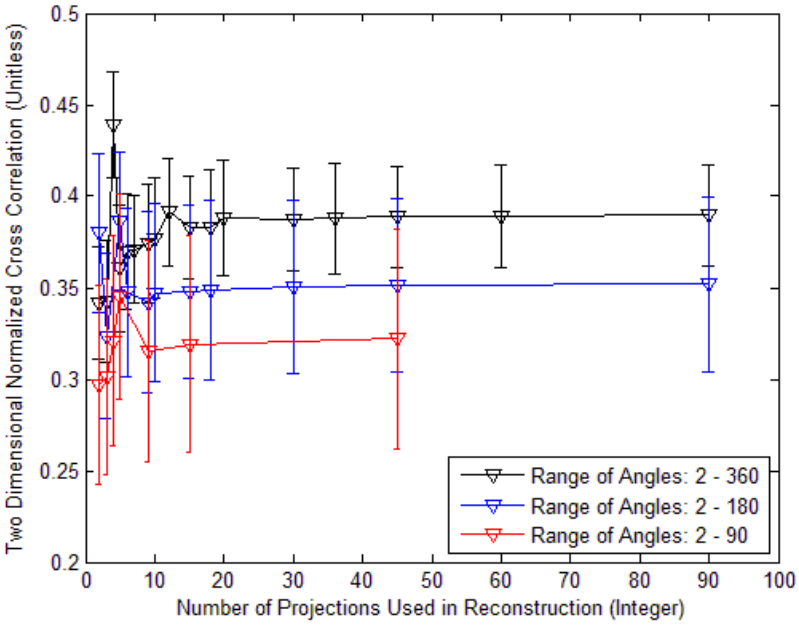

Figure 131. Reconstructed image quality of front lit AF bar chart with random intensity, 5 nm separation

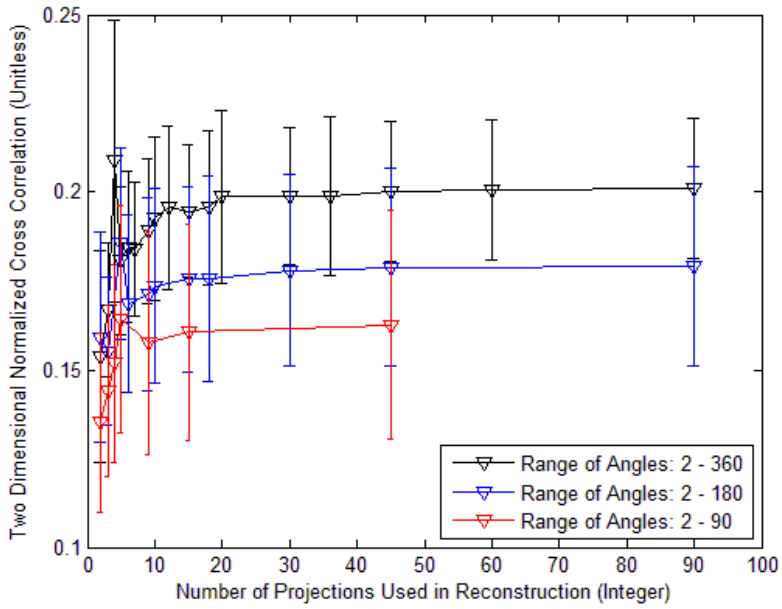

Figure 132. Reconstructed image quality of random intensity image, 5 nm separation

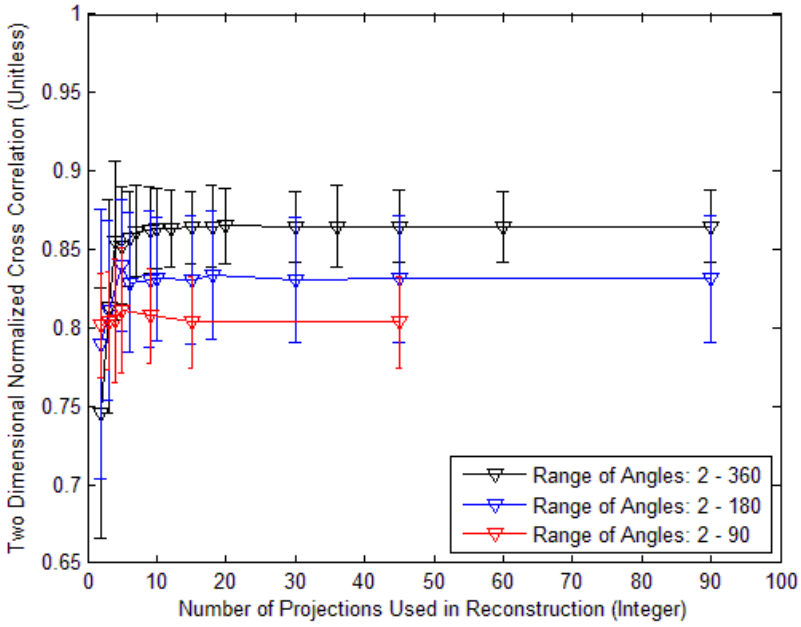

Figure 133. Reconstructed image quality of point source with constant intensity, 1 nm separation

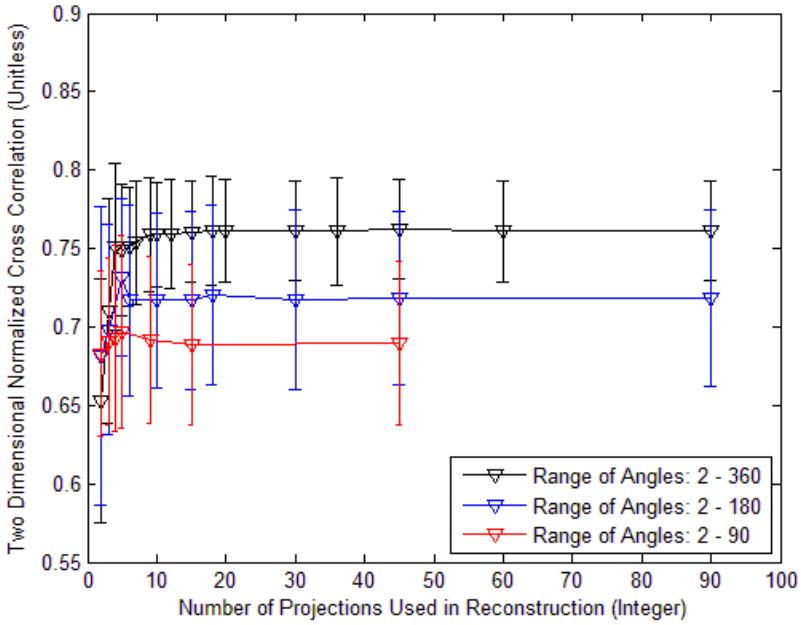

Figure 134. Reconstructed image quality of point source with random intensity, 1 nm separation

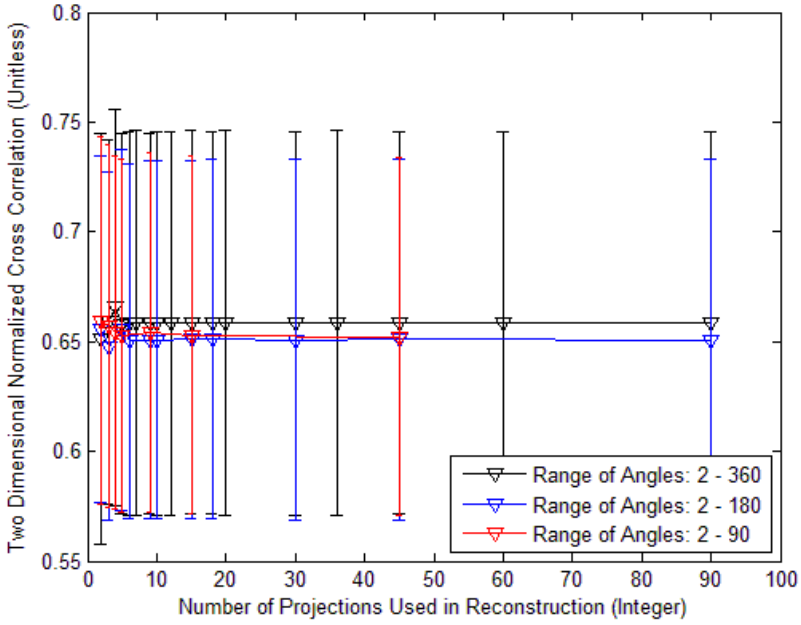

Figure 135. Reconstructed image quality of letter with constant intensity, 1 nm separation

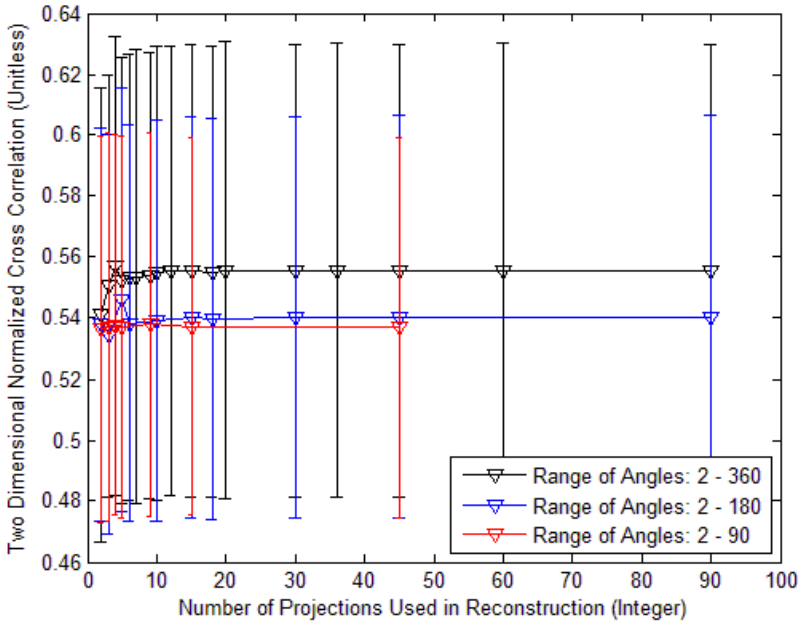

Figure 136. Reconstructed image quality of letter with random intensity, 1 nm separation

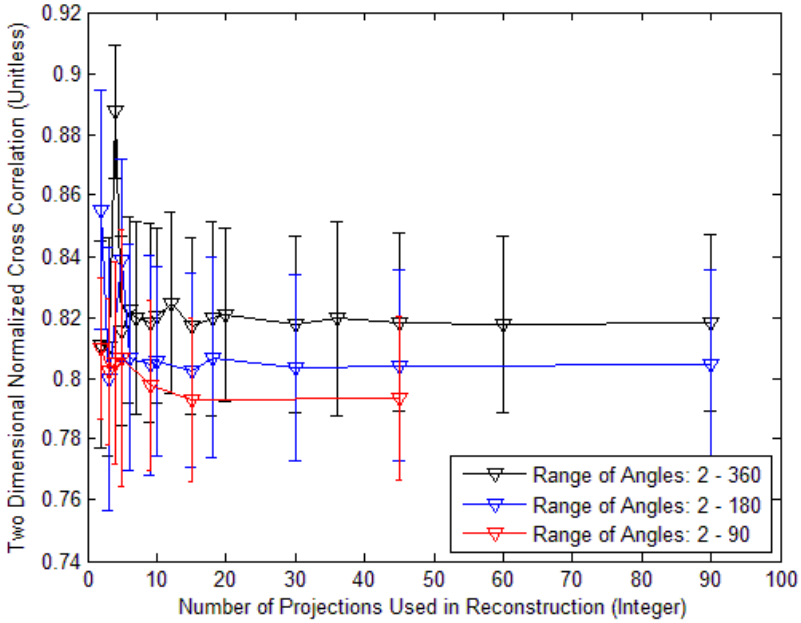

Figure 137. Reconstructed image quality of backlit AF bar chart with constant intensity, 1 nm separation

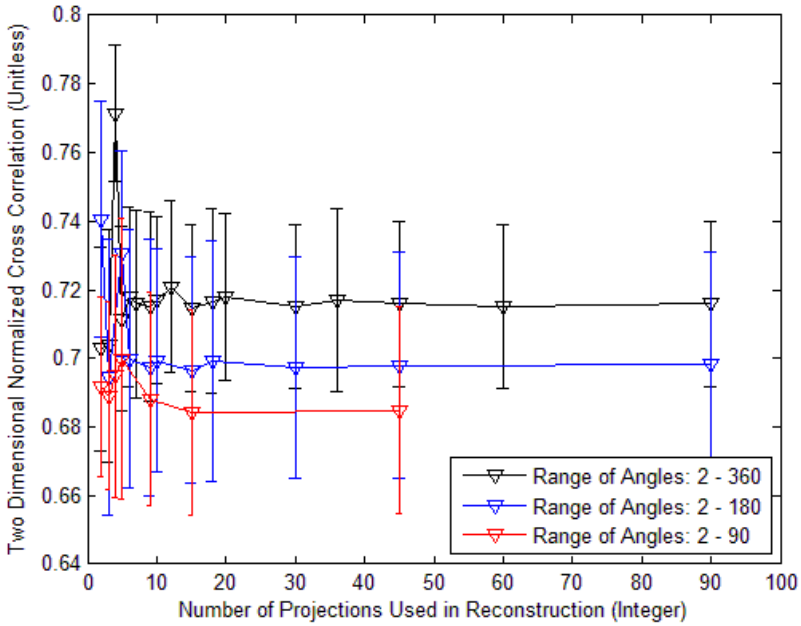

Figure 138. Reconstructed image quality of backlit AF bar chart with random intensity, 1 nm separation

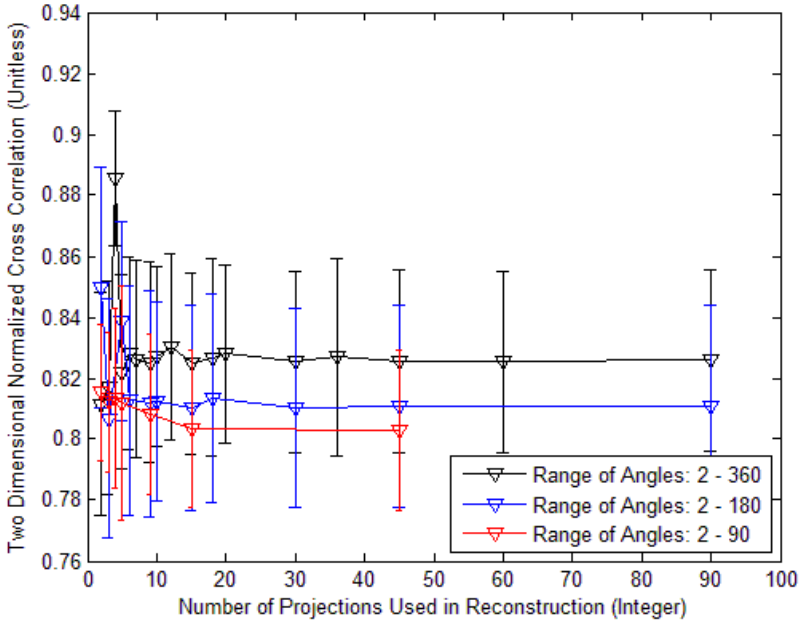

Figure 139. Reconstructed image quality of front lit AF bar chart with constant intensity, 1 nm separation

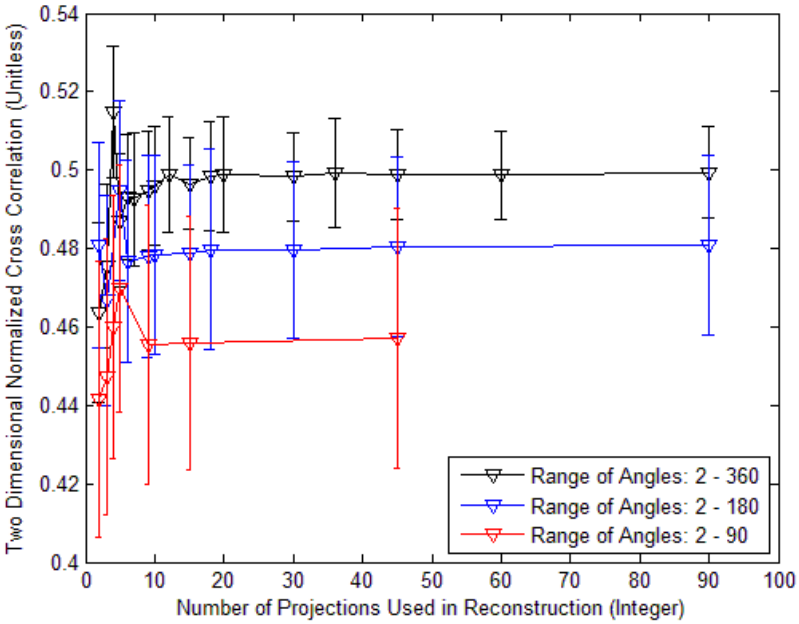

Figure 140. Reconstructed image quality of front lit AF bar chart with random intensity, 1 nm separation

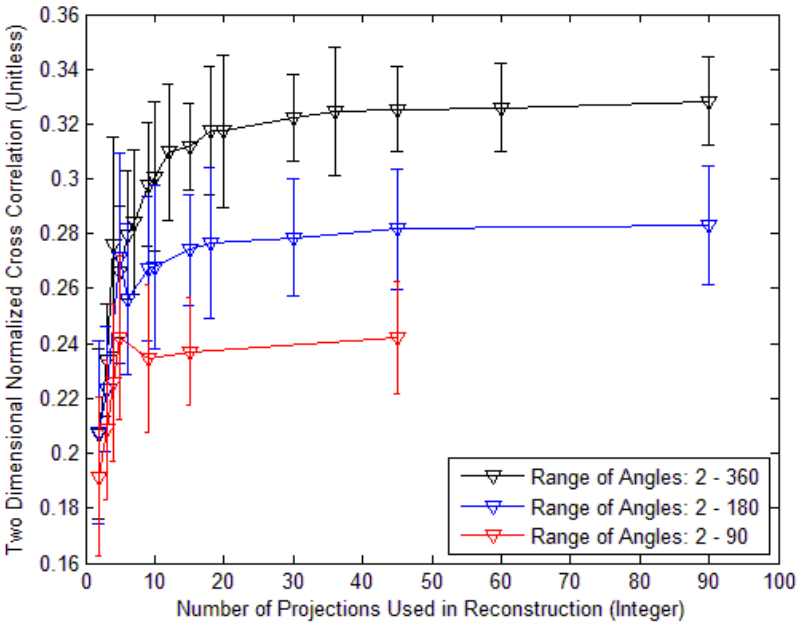

Figure 141. Reconstructed image quality of random 400x400 intensity image, 1 nm separation

References

[1] Brodzik, Andrzej and Jonathan Mooney. "*Convex projections algorithm for restoration of limited-angle chromotomographic image*s". J. Opt. Soc. Am. A, 16(2):246–257, February, 1999.

[2] Deming, Ross W. "*Chromotomography for a rotating-prism instrument using backprojection, then filtering*". Opt. Lett., 31(15):2281–2283, Aug 2006.

[3] Ford, Bridget K., Jose S. Salazar, and Mark P. Wilson. Reconstruction Algorithm Development and Assessment for a Computed Tomography Based Spectral Imager. Technical report, Albuquerque, NM, 2005.

[4] Fischer, Robert. *Optical System Design*, Mc Graw Hill, second edition, 2008

[5] Gaskill, Jack. *Linear Systems, Fourier Transforms, and Optics*, John Wiley and Sons Inc, 1978

[6] Hawks, Michael R. Prism Designer and Professor.

[7] Jet Propulsion Laboratory. "*Airborn Visible/Infrared Imaging Spectrometer*". Online, August 2012. URL http://aviris.jpl.nasa.gov/aviris/.

[8] Jiang, Hsieh. *Computed Tomography*, SPIE PRESS, second edition, 2009

[9] Mooney, Andrzej Brodzik, Jonathan M. and Myoung An. "*Principle component analysis in limited-angle chromotomography*". SPIE, 3118:170–178, 1999.

[10] Mooney, Jonathan T. "*Angularly Multiplexed Spectral Imager*". SPIE, 2480:65–77, 1995.

[11] Murguia, James E., Toby D. Reeves, Jonathan M. Mooney, William S. Ewing, Freeman D. Shepherd, and Andrzej K. Brodzik. "*Compacted visible /near-infrared hyperspectral imager*". volume 4028, 457-468. SPIE, 2000. URL http://link.aip.org/link/?PSI/4028/457/1

[12] O'Dell, Daniel C. *Development and Demonstration of a Field-Deployable Fast Chromotomographic Imager*. Master's thesis, Air Force Institute of Technology, Wright-Patterson Air Force Base, Ohio, 2010.

[13] Zemax Development Corporation. *Zemax User's Manual*, Feb 2011.

[14] Zygo Corporation. *MetroPro Reference Guide* OMP-0347, 2004l

REPORT DOCUMENTATION PAGE

Form Approved
OMB No. 074-0188

The public reporting burden for this collection of information is estimated to average 1 hour per response, including the time for reviewing instructions, searching existing data sources, gathering and maintaining the data needed, and completing and reviewing the collection of information. Send comments regarding this burden estimate or any other aspect of the collection of information, including suggestions for reducing this burden to Department of Defense, Washington Headquarters Services, Directorate for Information Operations and Reports (0704-0188), 1215 Jefferson Davis Highway, Suite 1204, Arlington, VA 22202-4302. Respondents should be aware that notwithstanding any other provision of law, no person shall be subject to any penalty for failing to comply with a collection of information if it does not display a currently valid OMB control number.

PLEASE DO NOT RETURN YOUR FORM TO THE ABOVE ADDRESS.

1. REPORT DATE *(DD-MM-YYYY)*	2. REPORT TYPE	3. DATES COVERED *(From – To)*
27-03-2014	Master's Thesis	Oct 2012 - Mar 2014

4. TITLE AND SUBTITLE
COMPARATIVE ANALYSIS OF RECONSTRUCTED IMAGE QUALITY IN A SIMULATED CHROMOTOMOGRAPHIC IMAGER

5a. CONTRACT NUMBER

5b. GRANT NUMBER

5c. PROGRAM ELEMENT NUMBER

6. AUTHOR(S)
Tervo, Ryan L, Captain, USAF

5d. PROJECT NUMBER

5e. TASK NUMBER

5f. WORK UNIT NUMBER

7. PERFORMING ORGANIZATION NAMES(S) AND ADDRESS(S)
Air Force Institute of Technology
Graduate School of Engineering and Management (AFIT/EN)
2950 Hobson Way, Building 640
WPAFB OH 45433

8. PERFORMING ORGANIZATION REPORT NUMBER
AFIT-ENP-14-M-35

9. SPONSORING/MONITORING AGENCY NAME(S) AND ADDRESS(ES)

10. SPONSOR/MONITOR'S ACRONYM(S)
n/a

11. SPONSOR/MONITOR'S REPORT NUMBER(S)

12. DISTRIBUTION/AVAILABILITY STATEMENT
DISTRIBUTION STATEMENT A APPROVED FOR PUBLIC RELEASE; DISTRIBUTION UNLIMITED

13. SUPPLEMENTARY NOTES
This material is declared a work of the U.S. Government and is not subject to copyright protection in the United States.

14. ABSTRACT
A hyperspectral chromotomographic instrument has been developed to determine the spatial and spectral distribution of a target. It does this by recording the dispersed images produced by a rotating direct vision prism with a high speed camera. The recorded images are processed through a tomographic reconstruction algorithm to produce a reconstructed hypercube. A physics-based system model was developed to investigate three areas. The first was how the prism angle selection and range of angles used impacted the reconstructed image quality. The second was an assessment of a new iterative reconstruction algorithm developed to remove artifacts produced in the Back Projection algorithm. The third area was how optical aberrations in the recorded images impacted the reconstructed image. The areas of investigation were completed using a new prism design because a distortion-like effect found in the current prism design. The majority of the image quality gains were accomplished in the first 30 projections used in the reconstruction. Provided at least 30 projections were used in the reconstruction the new algorithm, developed for this investigation, outperformed Back Projection in 15 of the 18 targets evaluated.

15. SUBJECT TERMS
Hyperspectral Imager, Chromotomography, Compare Reconstruction Algorithms, Impact of Aberrations, Image Quality, Simulation

16. SECURITY CLASSIFICATION OF:			17. LIMITATION OF ABSTRACT	18. NUMBER OF PAGES	19a. NAME OF RESPONSIBLE PERSON
a. REPORT	b. ABSTRACT	c. THIS PAGE			Dr.Michael Hawks (AFIT/ENP)
U	U	U	UU or SAR	147	19b. TELEPHONE NUMBER *(Include area code)* (937) 255-6565, x 4828 (Michael.Hawks@afit.edu)